Fall 2007

Electron beam characterization of carbon nanostructures

Eric Samuel Mandell

Department: Physics

ELECTRON BEAM CHARACTERIZATION OF CARBON NANOSTRUCTURES

by

ERIC MANDELL

A DISSERTATION

Presented to the Faculty of the Graduate School of the

UNIVERSITY OF MISSOURI – ROLLA

AND

UNIVERSITY OF MISSOURI – ST. LOUIS

In Partial Fulfillment of the Requirements for the Degree

DOCTOR OF PHILOSOPHY

in

PHYSICS

2007

Phil Fraundorf, Chair	**Dan Waddill, Co-Chair**
Erika Gibb	**Massimo Bertino**
Scott Miller	

ABSTRACT

Atom-thick carbon nanostructures represent a class of novel materials that are of interest to those studying carbon's role in fossil fuel, hydrogen storage, scaled-down electronics, and other nanotechnology. Electron microscope images of "edge-on" graphene sheets show linear image features due to the projected potential of the sheets. Here, intensity profiles along these linear features can measure the curvature of the sheet, as well as the shape of the sheet (i.e. hexagonal, triangular). Also, electron diffraction powder profiles calculated for triangular graphene sheet shapes show a broadening of the low-frequency edge of diffraction rings, in comparison to those calculated for hexagonal sheets with a similar number of atoms. Calculated powder profiles further indicate that curvature of a sheet will broaden the tailing edge of the diffraction peaks.

These simulation results are applied to the characterization of nanocrystalline carbon cores found in a subset of graphitic presolar stardust. Electron diffraction data from these cores indicates they are comprised primarily of unlayered graphene sheets. Comparison to simulations indicates that these sheets are more triangular than equant, and thus likely the result of some anisotropic growth process. This assertion is separately supported by intensity profiles of linear features in HRTEM images. The density of the cores is further shown to be less than 90% of the density of graphitic rims surrounding these cores. This structural data constrains proposed grain formation mechanisms in AGB atmospheres, and opens up the unexpected possibility that these presolar cores may have been formed by the dendritic crystallization of liquid carbon droplets.

ACKNOWLEDGMENTS

I wish to thank all of my friends and loved ones who have supported me over the many years spanning this project. I would also like to sincerely thank his advisor, Dr. Phil Fraundorf for his encouragement and consultation throughout this work and beyond. Lastly, my sincere gratitude is extended to the NASA - Missouri Space Grant Consortium, and the Department of Physics and Astronomy at both the University of Missouri – St. Louis and at the University of Missouri – Rolla for their financial support and otherwise in helping this work come to fruition.

TABLE OF CONTENTS

LIST OF FIGURES

1. INTRODUCTION

In its many forms, both nano and macro, carbon has intrigued mankind for centuries. One need only look at the phase diagram for carbon to see why this might be so (Bundy, 1980). While having one of the highest melting points of any known element, the melting temperature varies by more than 500[K] over a pressure range of ~ 0 – 15[GPa], with a peak around 9[GPa]. For most materials, the melting line slopes forward on the phase diagram, which is not the case here. In addition to this odd phase behavior, graphite is a member of a small group of materials that exhibit van der Waals bonding between its sp^2 bonded layers. The drastic difference between this bonding and the sp^3 bonding of diamond also make carbon and its structures interesting subjects of study.

Though nanoforms of both diamond and graphite certainly exist and are of interest, a third form of carbon structures, fullerenes, manifest on the nanoscale (Dresselhaus, et. al. 1996; Iijima 1991; Kroto, et. al. 1985; Oberlin, et. al. 1976). Fullerenes represent a set of many different nanostructures, which retain the six-member hexagonal bonding, similar to that in a graphene sheet, but are warped by the inclusions of five-member (pentagonal) or seven-member (heptagonal) rings. These defects induce curvature into the graphene sheet structure and give rise to the formation of buckyballs, caps on nanotubes, nanocones, and a variety of other spherical, ellipsoidal, and tubular structures. It is not surprising that these materials have very different electronic properties than bulk graphite or diamond, and are of great interest to the engineering community (Iijima 1991; Menon, et. al. 1996; Saito, et. al. 1992; Yu, et. al. 2000). However, due to their small size, and in some cases being only

one atom thick, fullerenes must be studied with electron beam techniques. Developing a better understanding of the appearance and behavior of nanocarbon forms in the electron microscope, for example, is critical in researching these structures (Hashimoto, et. al. 2005; Qin and Peng 2002; Wang and Hui 2003; Zuo, et. al. 2003).

While the engineering of nanomaterials here on Earth has only begun, it turns out that nanocarbon had been formed in red giant stellar outflows and supernovae long before our sun had begun burning (Amari, et. al. 1990, 1993; Bernatowicz, et. al. 1987, 1991; Hoppe, et. al. 1995; Lugaro 2005). This material traversed the interstellar medium (ISM), finally being incorporated in our solar system during its early formation, and likely provided much of the carbon we see today. Just as is the case for engineered nanomaterials, this presolar dust often requires electron beam analyses to characterize and identify structures. This data may often times prove useful in delineating between proposed formation mechanisms for the grains, as the evidence for certain structural features might indicate allowable temperature ranges during crystal growth, or some other criteria to explain their structure; just as is done with experimental materials from the laboratory.

The intention of this thesis is to bring forward some of the issues involving electron-beam analyses as they pertain to carbon nanostructures. Particular emphasis is given here to the imaging and characterization of "edge-on" graphene, which can be related to the imaging of nanocones, nanotubes, and many disordered carbon materials as well. Meanwhile, additional work related to the modeling of electron diffraction from collections of graphene sheets is also examined. Simulations of these analyses provide a background

for comparison to experimental data, when investigating a material of either known or unknown origin. The results of these simulations are then applied to the characterization and analysis of a subset of graphitic stardust containing a strange nanocrystalline carbon core (Bernatowicz, et. al. 1996; Croat, et. al. 2005, Fraundorf et al. 2000).

With this in mind, a review of carbon nanostructures and their study is first conducted, providing a background on graphene and its variations of form. This is followed by a brief synopsis of electron beam techniques and their simulation, as they will be utilized heavily in this work. An introduction to the history and knowledge surrounding the nanocrystalline stardust is also provided, which will be the primary subject for applying the electron-beam simulation results in this thesis. This chapter then concludes with an outline of the organization and what is to follow in subsequent chapters.

1.1 ATOM-THICK CARBON NANOSTRUCTURES

In recent years, much of society has become aware of the growing research into the properties, formation, and structure of carbon nanotubes (Dresselhaus, et. al. 1996; Iijima 1991; Oberlin, et. al. 1976). Single-walled nanotubes (SWNT) represent a version of carbon nanostructures that are only one atom thick (Figure 1.1). The atomic structure of single-walled nanotubes can be thought of as being derived from the wrapping of a single sheet of graphite, or graphene. The same can be said for other similar atom-thick carbon nanostructures such as nanocones or nanohorns.

The average nearest-neighbor C-C bond in graphite (1.42[Å]) is the nearly the same as the average bond length in most carbon nanostructures. This short bond distance speaks to the strength and durability of carbon structures. These structures also retain primarily the sp^2 bonding similar to that of graphite. While graphene is a flat, hexagonal network of carbon atoms, the other atom-thick structures are three-dimensional. Curvature can be introduced into the hexagonal graphene network by the insertion of a pentagonal bonding arrangement, where a single pentagonal defect can bend the sheet by 30° (Dresselhaus, et. al. 1996). In order to preserve inter-atomic distances, nearby atoms bend out of the plane of the pentagonal bond network, resulting in a corannulene molecular arrangement (Dresselhaus, et. al. 1996). Heptagonal bond networks can also be inserted, resulting in curvature of the hexagonal graphene. Combinations of these defects in the graphene lattice can result in closed structures and varying degrees of curvature, making possible the wide variety of structures observed.

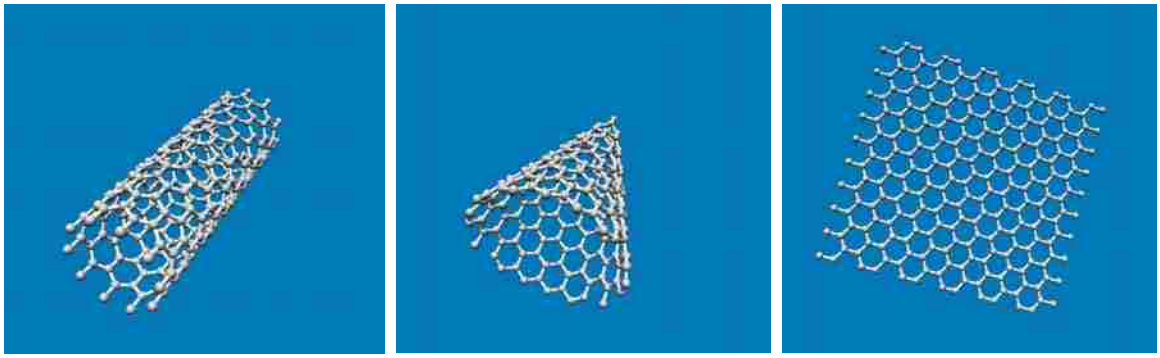

(a) **(b)** **(c)**

Figure 1.1: Atomic models for a carbon nanotube (a), a carbon nanocone (b), and a graphene sheet (c).

High-resolution TEM imaging and electron diffraction have proven useful in characterizing the size and helicity of carbon nanotubes (Wang and Hui 2003). These have been the most studied examples of atom-thick carbon, due to their desirable electrical properties and many proposed applications. The walls of the tubes are the dominant contrast feature when the tube lies along a direction perpendicular to the beam direction, since the projected mass-thickness is greatest there. Simulated TEM images of carbon nanotubes over many orientations, both with and without amorphous substrates, have helped explain contrast effects arising from the walls of the tubes (Wang and Hui 2003). With the recent research and interest in graphene as a viable material for scaled down electronics, understanding contrast effects in the TEM involving this material will aid in its identification and characterization.

1.2 ELECTRON BEAM TECHNIQUES AND SIMULATION

Electron beam characterization techniques, such as High-Resolution Transmission Electron Microscopy (HRTEM), Energy-Filtered TEM (EFTEM), Scanning Electron Microscopy (SEM), and Electron Energy Loss Spectroscopy (EELS), have been utilized to a great extent in examining carbon nanostructures (Iijima 1991; Menon, et. al. 1996; Saito, et. al. 1992; Yu, et. al. 2000). While studies have been focused typically on manufactured, laboratory materials, these techniques have also been used to study carbonaceous materials provided by nature (Bernatowicz, et. al. 1996; Fraundorf and Wackenhut 2002; Fraundorf, et. al. 2000; Jaszczak, et. al. 2003; Mandell 2006). It is critical, when employing these techniques, that the researcher understand the contrast and image artifacts that may be present in the data due to changes in crystal structure and instrument parameters. A better

comprehension of results and expectations are commonly arrived at through models, simulations, and an understanding of the image formation process.

1.2.1. Phase Contrast TEM Imaging. The short wavelengths of electrons accelerated to energies of 300[keV] (~0.00197[nm]) present the researcher with a great tool for the examination of crystals on the nanoscale (Williams & Carter 1996). In a sense, these relativistic electrons can be used to image the arrangement of atoms in a crystal in a manner somewhat analogous to using light imaging. However, the scattering of the incident radiation is but one of the many physical differences between these two regimes.

Electrons are strongly scattered by atoms in the crystal. In the simplest approximation, each electron would undergo a single scattering event, though this is rarely the case. For a thorough simulation of electron scattering, a dynamical multiple-scattering model should be considered in most cases (Hren, et. al. 1986; Spence 1988). The single-scattering approximation is valid for very thin specimens with light atoms, and atom-thick carbon structures represent a class of materials that fall under this category. Given the wave-behavior of relativistic electrons, TEM images can be simulated for atom lists corresponding to carbon nanostructures by calculating phase changes in the wave front of the electron, when transmitted through the potential field of the specimen. The contrast arises from these phase changes. Recording the phase changes allows for the formation of transmitted image of the specimen (Figure 1.2(a)).

Model phase-contrast TEM images may be calculated using a variety of different software packages that are commercially available. Here we take advantage of procedures developed by E. J. Kirkland in Chapter 2 (Kirkland, 1988). One can also use mathematics software to set up a weak-phase object image simulation that computes the exit electron wave function after passing through a specimen where the atomic potential has been projected into a single plane (Hren, et. al. 1986). While this sort of simulation will breakdown for thicker specimens (> 20[nm]), it will be sufficient here since the specimens examined in this thesis (Chapters 2 and 4) are no thicker than 4[nm] (Ho, et. al. 1988).

Electrons are first approximated as a plane wave passing through the specimen. Given the projected potential of the specimen along the beam direction, a distribution of phases and amplitudes are calculated depending on the variations of the projected potential. The Fourier transform of the exit complex wave will give the Fraunhofer diffraction pattern, formed in the back focal plane of the magnetic lenses used to focus the electrons. This is really the angular distribution of the intensity if no lenses were present. Performing a second Fourier transform with the Fraunhofer diffraction pattern, multiplied by the complex contrast transfer function (CTF) of the lens, will form the simulated image as a recombination of the diffracted beams from each part of the specimen (Hren, et. al. 1986; Spence 1988). The CTF is a function that defines the modulation of amplitudes and phases in the Fraunhofer diffraction pattern by considering the effects of lens aberrations, beam convergence, and chromatic aberrations resulting from a range of electron energies in the beam (Hren, et. al. 1986; Reimer 1997). These factors cause contrast reversals and prevent the transfer of certain spatial frequencies in the diffraction data. The CTF also defines the

point-to-point resolution of the TEM by constraining the range of spatial frequencies over which contrast is directly interpretable (Hren, et. al. 1986; Williams & Carter 1996).

1.2.2. Electron Diffraction. For simulation of 2D diffraction patterns of single nanocrystals, or ensembles of nanocrystals, it is possible to simply use the Fraunhofer diffraction pattern in the back focal plane, as described above. Here, the correlation between atom positions is reflected in the differences in scattered intensity. In the case of random arrays of atoms, the diffraction intensities will decrease going from lower to higher

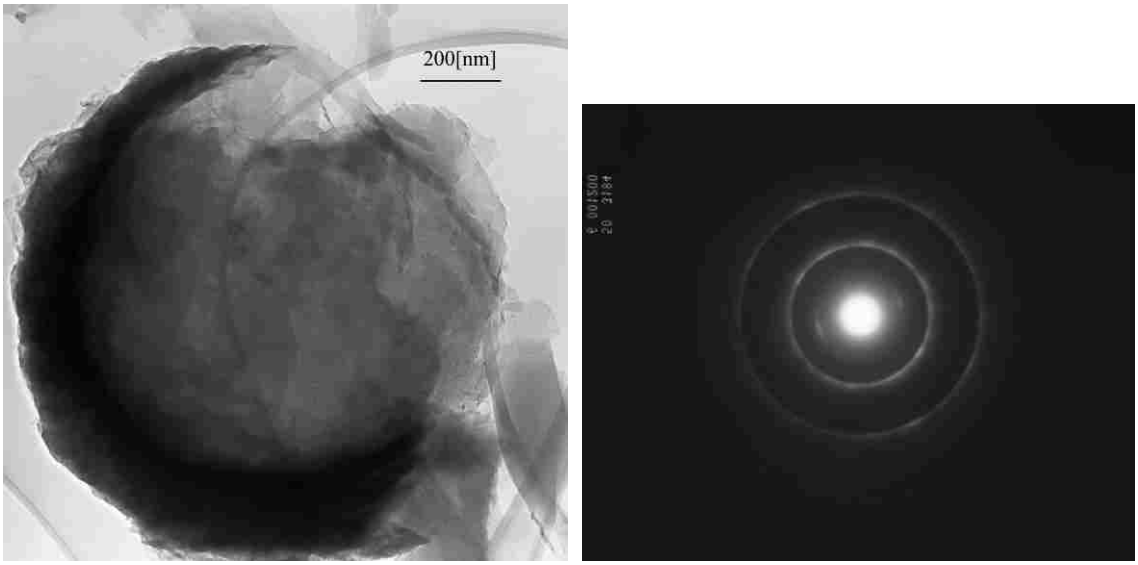

(a) **(b)**

Figure 1.2: (a) A conventional, phase-contrast, TEM image. Contrast arises from phase changes in the electron wave front after being transmitted through the specimen. Darker regions represent more optically dense regions. (b) An electron diffraction pattern from a collection of nanocrystals. The radii of the rings surrounding the central bright spot correspond to specific crystal lattice periodicities.

scattering angles. These intensities are also proportional to the square of the atomic scattering factor. If the array of atoms is periodic, regularly spaced spots with separations proportional to the reciprocal of the period of the crystal lattice will form in the back focal plane. Crystal shape can affect the shape of these spots, as they appear smeared out when the crystal is very small. Earlier studies have provided some expectations for the shape of diffraction peaks from atom-thick crystals, such as the graphene being examined in this thesis (Warren 1941). In addition, spots will either be spread out or have intensities changed when the crystal is bent or distorted, due to the changes in the relative directions of the lattice periodicity in different parts of the crystal (Hren, et. al. 1986; Williams & Carter 1996).

Modeling of scattering, or electron diffraction, data for molecules averaged over all orientations is performed rather readily by using the Debye scattering model,

$$I_{eu} = \sum_{m} \sum_{n} f_m f_n \frac{\sin(g r_{mn})}{g r_{mn}} \tag{1}$$

which computes scattering intensities at each reciprocal distance, g, where f is an atomic scattering factor and r_{mn} is the real space vector between atom m and atom n (Warren 1969/1990). This type of simulation is useful for comparison to experimental powder patterns (Figure 1.2(b)) obtained from Selected-Area Electron Diffraction (SAED) data from collections of nanocrystals (Chapter 3), and will be the primary means for simulation of diffraction data in Chapter 2 of this thesis.

1.2.3. Scanning Transmission Electron Microscopy. In conventional TEM, the electron wave interacts with the specimen and the Fraunhofer diffraction pattern is formed in the back focal plane. Each point in the image is formed by collecting the electrons from each part of the specimen contributing to phase changes at that point. In scanning transmission electron microscopy (STEM), the electron source is focused into a narrow beam that is scanned across the specimen. Some portion of the incident intensity is scattered, or transmitted, and detected to form the image signal at each point (Hren, et. al. 1986).

Rather than using apertures that collect electrons scattered into certain angles, as in conventional TEM, the detector size in STEM will define the angular acceptance. Collecting electrons scattered within ~0-10[mrad] of the beam direction results in a bright-field image that is similar to that formed in conventional TEM. When collecting electrons

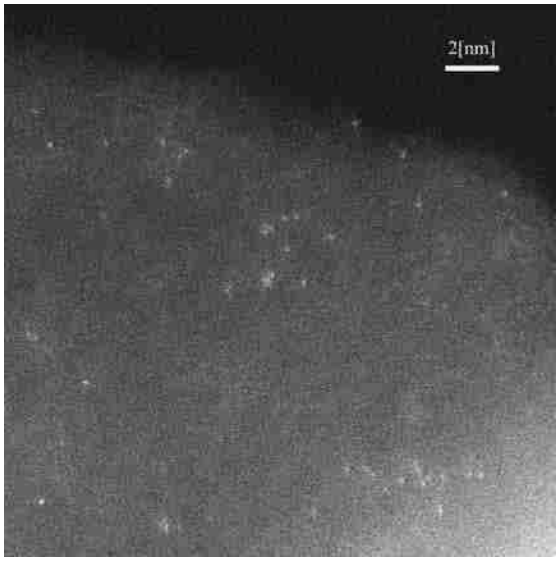

Figure 1.3: An HAADF-STEM image. The small bright spots correspond to single atoms and clusters of atoms with atomic numbers much greater than the surrounding medium.

that have been scattered to high angles (>50[mrad), an image can be formed where the contrast depends on the atomic number, Z, of the scattering atoms. Single atoms scatter the incident beam incoherently, and heavier atoms will scatter incident electrons to higher angles (Hren, et. al. 1986; Williams & Carter 1996). By using a High-Angle Annular Dark Field (HAADF) detector (Figure 1.3), the strength of the this scattering can be recorded at each point in the specimen, and form an image where heavy atoms will stand out well against a background of lighter atoms (Chapter 4) (Howie 1979).

1.2.4. Electron Energy Loss Spectroscopy. As electrons pass through the specimen and are scattered, they lose energy. By placing a spectrometer in the TEM column and collecting the electrons post-specimen, the energy losses of the electrons may be measured (Electron Energy Loss Spectroscopy or EELS). Alternatively, electrons that have lost energy within a specified range can be filtered and used to form an image (Energy-Filtered TEM or EFTEM) (Williams & Carter 1996).

The EELS spectrum (Figure 1.4) is dominated by the zero-loss peak (~0-2[eV]), which represents those electrons that have been scattered elastically and were within the angular acceptance of the collector aperture. The remaining spectrum is usually divided into a low loss region (~5-25[eV]) and a high loss region (~10-1000) based on the processes that give rise to the features observed. Features in the low loss region are typically due to plasmon losses, or interactions with the electrons in the specimen. The intensity in the high loss region is significantly weaker than the zero-loss peak. The features seen there are due to the ionization of atoms, where inner shell electrons have been

given sufficient energy to move them away from the nucleus (Williams & Carter, 1996). In order to gauge the mean-free-path thickness, or density of the material in cases where the physical thickness is known, the integrated intensity under the zero-loss peak can be compared to the integrated intensity for the entire spectrum (Chapter 5) (Egerton, 1996).

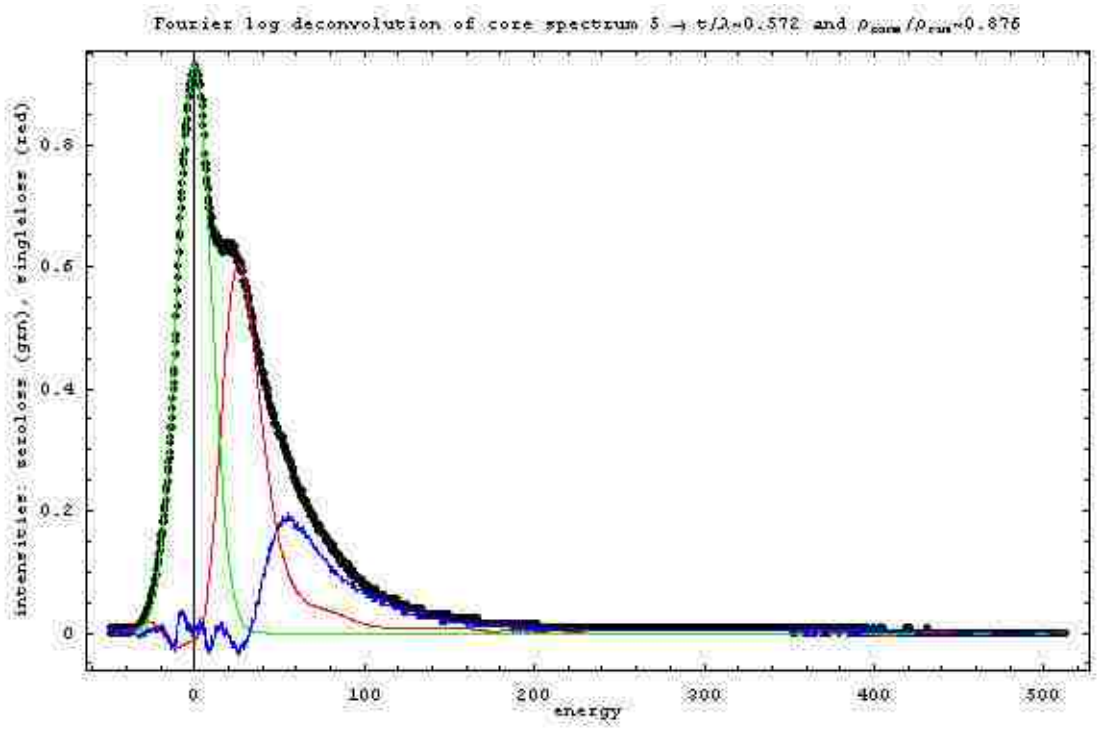

Figure 1.4: An example of electron energy-loss data (black line). The green line is a Gaussian curve fit to the zero-loss peak. The red line represents the energy-loss profile corresponding to single-scattering of the incident electrons, and the blue line represents the energy-loss profile due to plural scattering.

Because the scattering of electrons through the specimen is dependent on the mean-free-path of the electrons through that material, it is possible to use elastic images in the EFTEM (images formed using only zero-loss electrons), along with a conventional bright-

field image, to calculate a relative mean-free-path thickness image (Egerton 1996). In this result, contrast differences in the image are due to differences in mean-free-path within the field of view. In cases where the physical thickness of the specimen or approximate values of density are known for portions of the specimen, inferences may be made about the density of other regions of the specimen (Chapter 5) (Egerton 1996; Williams & Carter 1996).

1.3 GRAPHENE CORES IN GRAPHITIC STARDUST

The term 'stardust' (also referred to as stellar or presolar grains) is used to refer to those materials, often found in meteorites, exhibiting isotopic compositions that require they were produced in other stars (Lugaro 2005). Stardust provides us with a group of materials from nature that offer an interesting challenge for electron beam characterization (Amari, et. al. 1990, 1992; Bernatowicz, et. al. 1996). Grains produced in supernovae and stellar ejecta populate the interstellar medium and were incorporated into our solar system during the formation of the sun. While many grains were melted or otherwise altered during our sun's formation, some survived intact within meteorites and other solid masses. The discovery of stardust in meteorites that crashed here on Earth opened new access to interstellar material and new avenues of research in materials astronomy (Bernatowicz & Walker 1997; Lugaro 2005).

Representing a small percentage of the material in some carbonaceous chondrite meteorites, stardust is identified by measuring the isotopic ratios present in different types of grains and comparing to the expected solar values. Grains that form around our sun will

have isotopic ratios governed by the nuclear reactions occurring within the solar core. These ratios can be measured using Secondary Ion Mass Spectrometry (SIMS), or NanoSIMS in the case of measuring individual grains, where the sample is slowly sputtered away using a primary ion beam (Benninghoven, et. al. 1987; Lugaro 2005). The charged atoms and small molecules that are ejected from the specimen are extracted into a mass spectrometer. Stardust will carry different nucleosynthesis fingerprints that depend on the stellar source present during their formation. In the case of grains composed primarily of carbon, these are commonly identified as presolar when the C^{12}/C^{13} ratio is deviated far from the solar value (~89) (Lugaro 2005).

Interesting examples of presolar grains are micron-sized graphite spherules, a subset of graphitic stardust, formed in red giant atmospheres (Figure 1.5) (Amari, et. al. 1990, 1995; Bernatowicz, et. al. 1996, 2005; Bernatowicz & Walker 1997; Croat, et. al. 2005; Fraundorf & Wackenhut 2002; Fraundorf, et. al. 2000; Mandell, et. al. 2006; Stadermann, et. al. 2004, 2005). These grains are characterized by their core-rim structure and spherical shape. While the rims are made up of concentric graphitic layers, similar to those found in carbon onions, the cores are composed of carbon in an unknown nanocrystalline phase (Ugarte 1992). Electron diffraction data suggests that the cores are comprised primarily of unlayered graphene. This is evidenced by the high frequency tails seen on the graphene peaks in azimuthally- averaged diffraction data, and the mysterious absence of any (002) graphitic layering rings (Bernatowicz, et. al. 1996; Croat, et. al. 2005). Even amorphous carbon has a broad feature in diffraction due to (002) layering. The size of these cores and the complete suppression of graphitic layering make their formation a true mystery and

challenge for materials engineering. Any proposed formation mechanism for these grains must be able to account for these observations.

In addition to the diffraction data, graphene sheets have been found in HRTEM images (Fraundorf & Wackenhut 2002). Here, the sheets are likely only visible when viewed "edge-on", relative to the direction of the electron beam, so as to provide the necessary mass-thickness to stand out within the surrounding core material. By searching for thin, torn regions of the nanocrystalline cores that are not obstructed by the amorphous carbon support film (used for TEM specimen mounting) it is possible to see "edge-on" graphene within the cores. This image data can be analyzed to reveal statistics on the size and orientation of nearby or adjacent sheets, and the number of sheets visible per unit area. It is here that simulations can be used to compare proposed growth models to experiment, and intensity variations in different sheet shapes when viewed "edge-on" to those seen in the core data. Once again, electron imaging results must be reconciled with the diffraction data and any other measurements in order to finally evaluate proposed formation models.

1.4 DISSERTATION OUTLINE

The content of this work is focused on simulations of electron imaging and scattering for various carbon nanostructures, used to characterize unlayered graphene cores found in a subset of graphitic stardust. This is of interest to the materials research community in that it describes electron characterization signatures for a variety of carbon nanostructures. These are useful in aiding the researcher manufacturing these structures, or in identifying key differences between similar molecules. Of course, this work is of interest to the

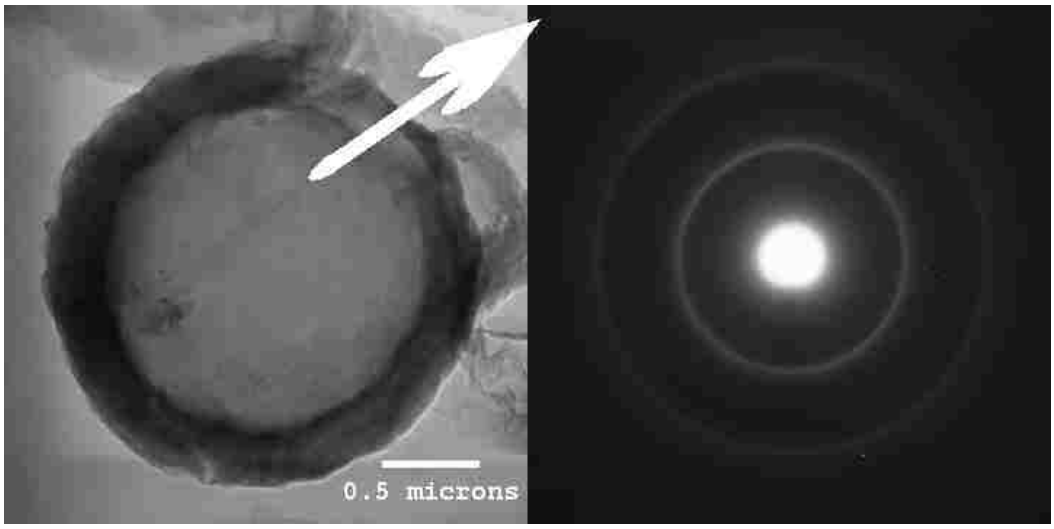

(a) **(b)**

Figure 1.5: (a) A phase contrast TEM image of core-rim graphitic stardust. The rim is made up of concentric graphitic layers, while the core is primarily unlayered graphene. (b) An SAED pattern from the core structure.

astrophysics community, as the stardust represents material populating the interstellar medium and carries the signatures of the stellar sources where they were formed. These grains also provide a window on material that was present during the early formation of our solar system.

Chapter 2 of this dissertation will discuss electron imaging and diffraction simulations for a variety of carbon nanostructures, including graphene and nanocones. This chapter will also investigate some of the interesting effects that arise due to graphene sheet shape, orientation, and relationships between nearby molecules. In Chapter 3, electron diffraction data from the presolar graphene cores is examined in detail, and compared to scattering models for various molecules. Electron imaging of the

nanocrystalline stardust cores is discussed in Chapter 4, along with inferences derived from comparisons to simulations. Density comparisons between the core and rim are detailed in Chapter 5, using both EELS and mean-free-path images calculated from EFTEM image data. Finally, Chapter 6 discusses how all of these electron beam characterization results bear on three different proposed grain growth models, and ends with a discussion as to what work lays ahead for further studies of these strange carbon cores.

2. GRAPHENE STRUCTURAL COMPARISONS IN ELECTRON IMAGING AND SCATTERING SIMULATIONS

Many avenues of research involved with carbon nanostructures of one form or another must wrestle with interpreting electron imaging and diffraction data. Atom-thick carbon structures have been proposed recently as a novel material for scaled down electronics, and appear in a variety of forms, including graphene and single-walled carbon fullerenes (i.e. nanotubes, nanocones) (Dresselhaus, et. al. 1996; Ewels 2002; Hansson 2000; Hashimoto et. al. 2005; Iijima 1980, 1987; Kasuya, et. al. 2002). These materials are also relevant to researchers investigating a variety of energy related issues from hydrogen storage to carbons in soot, coal, or petroleum (Gilliland & Harriott 1954; Iijima, et. al. 1996; Murr and Soto 2005; Veranth, et. al. 2000). Improving the ability to characterize the structure of graphene and other molecular carbon forms will aid these material studies and perhaps provide a better understanding of formation mechanisms, or the role of growth conditions present during fabrication.

In order to characterize the shape and structure of atom-thick carbonaceous materials, it is helpful to construct appropriate molecular models and simulate electron image and diffraction data from these structures. Observed differences between simulated data from different structures provide a framework for comparison and identification in experimental materials. In this work, the shape of graphene sheets is differentiated by examining greyvalue intensity profiles along “edge-on” structures in simulated phase-contrast TEM images. Profiles for hexagonal sheets differ significantly from those of triangular sheets.

Because of this, triangular sheets may be identified when faceting occurs around pentagonal defects within graphene's hexagonal lattice structure (Chapter 4).

Additionally, simulated TEM images can be utilized in considering patterns that emerge in homogenous collections of molecules. By examining simulated image results from collections of randomly-oriented, identical molecules, statistics on quantities such as "observed angles between linear features" become tools by which nanostructure species might be distinguished from another (Chapter 4). In this case, simulated images of randomly-oriented, faceted nanocones and relaxed nanocones are compared, revealing certain preferential angles between linear features in the images.

Electron scattering models for various carbon nanostructures can be compared in order to gauge how shape effects, similar to those mentioned above, manifest in diffraction. Model diffraction profiles for specific molecules were calculated using the formula described by Debye, which averages the molecule over all orientations relative to the electron beam (Warren 1969/1990). This creates an azimuthally-averaged powder profile as if from an infinite collection of identical crystals. Due to the atom-thick nature of graphene, interesting changes in diffraction peak shape arise quickly from changes in crystal shape (Chapter 3). Also, it is shown here that graphene peak shapes are altered due to curvature or faceting around pentagonal defects (i.e. nanocones), including the development of satellite peaks near the graphene periodicities. These satellite peaks manifest due to the coherence between lattice fringes resulting from in-plane defects that warp the 2D graphene crystal into a 3D structure.

Cataloging the observed differences between graphene-like structures in electron beam simulations should provide a back-drop for analyses of experimental materials. Structural knowledge arrived at through these comparisons will likely shed light on growth and formation mechanisms, as well as open avenues for identification of other sheet characteristics in electron image and diffraction data.

2.1 TEM IMAGE SIMULATION AND THE DEBYE MODEL

For simulation of phase contrast TEM images, C++ routines written by E.J. Kirkland were employed (Kirkland 1998). These allowed for the simulation of the projected atomic potential for several atom lists, each representing a carbon nanostructure of interest under a certain orientation, and embedded in a 40Å thick amorphous carbon layer. The atom positions of the amorphous layer were identical in each simulation and serve to dampen Fourier ringing in the image from the finite graphene molecules. The amorphous layer also provides a gauge as to how well the edge-on features are able to stand out against a thicker background material.

The atomic potentials for each atom list were projected into a single layer for image simulation, where the weak-phase object approximation should be applicable in dealing with such thin simulated materials. That is to say that contrast in simulated images may be interpreted intuitively up to the resolution limit of the model electron microscope, defined by the energy of the electrons, the amount of spherical aberration allowed for in the model, and the defocus at which the electron wavefront exiting the specimen is sampled (Hren, et. al. 1986). Optimal resolution in phase contrast TEM imaging occurs at Scherzer defocus,

where the first zero in the contrast transfer function is extended outward as far as possible in reciprocal space, allowing a wider range of spatial frequencies to be directly interpretable (Williams and Carter 1996, Reimer 1986).

In this work, two different model scopes are considered, using 300[kV] electrons and objective apertures with 0 – 12[mrad] acceptance; one with a resolution of about 2[Å] (C_S = 1.2[mm] and Δf = 541[Å]), and another with 1[Å] resolution (C_S = 0.069[mm] and Δf = 135[Å]). Because the average C-C bond length (1.42[Å]) is between these two resolution limits, it is expected that the atomic columns may be more discernible in the 1[Å] simulation, when the graphene is viewed edge-on, than in the other model.

Upon simulation of 32-bit floating point image data, the images were imported into ImageJ for analysis. Greyvalue intensity profiles were calculated in ImageJ by selecting a window over the edge-on, atom-thick feature in the image. The intensity is averaged across the window selection iteratively, along the edge-on feature. Because the measured greyvalue intensity is affected by the amorphous layer, we get some indication as to how distinguishable the sheet is under less than ideal conditions.

For simulation of electron diffraction data from carbon nanostructures, Debye scattering profiles may be calculated using the Debye formula (Equation 1 in Chapter 1),

$$I_{eu} = \sum_m \sum_n f_m f_n \frac{\sin(gr_{mn})}{gr_{mn}} \qquad (1)$$

where f is an atomic scattering factor for electrons, g is a reciprocal space distance and r_{mn} is the real space vector between atom m and atom n in the list of atoms comprising the molecule of interest (Warren 1969/1990). The scattered intensity, I, is computed for each reciprocal space distance, considering all possible orientations of the molecule. This results in the azimuthally-averaged powder profile for an infinite collection of identical molecules under all possible orientations. While this does not provide the diffraction pattern for a single molecule under a specific orientation, it allows for the comparison of molecule shape effects in diffraction for collections of similar crystals.

2.2 INTENSITY PROFILES IN SIMULATED PHASE-CONTRAST TEM IMAGES

While there are certainly obvious physical differences when comparing atomistic models of graphene with different shapes, sizes, and curvature, it is not immediately apparent how these features might manifest, or be measurable, in TEM data. One can imagine that an atom-thick structure, such as graphene, is likely most visible when viewed edge-on, so that the atomic columns are parallel to the direction of the electron beam. This provides the necessary mass-thickness contrast to stand out against a background of other randomly-oriented molecules, or amorphous material. In comparing the two different graphene molecules pictured in Figure 2.1, one can also imagine that differences in the lengths of the atomic columns due to sheet shape differences might be measurable in TEM images. Perhaps even the orientation of the sheet may be discernible, given a strong understanding of the model and expectations derived from its employ. In either case, the effects should manifest as differences in greyvalue intensity in the image, where profiling may be used to distinguish between them.

In order to investigate this scenario, atomic models of edge-on graphene, embedded in a 40[Å] thick amorphous layer, were constructed. Phase contrast TEM images of these models were simulated, using parameters discussed in Section 2.1, and intensity profiles were measured along the linear features corresponding to the edge-on sheets. In all cases, a hole was included in the image by "slicing" away some of the amorphous layer prior to image calculation. This hole provides a reference measurement where the total electron beam current in the model image is being recorded.

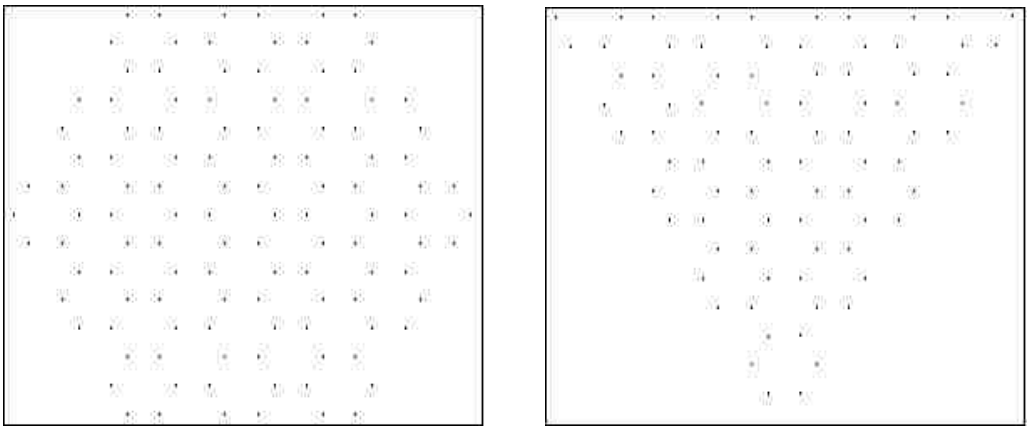

(a) **(b)**

Figure 2.1: Atomic models for a hexagonal graphene sheet (a) and a triangular graphene sheet (b). It is expected that these shape differences will give rise to observable differences when viewed edge-on in simulated TEM image data.

2.2.1. Graphene Sheet Shapes in Intensity Profiles. Beginning with the sheet orientations shown in Figure 2.1, where the electron beam is directed along the vertical in those models, phase contrast images of the hexagonal sheet viewed edge-on were simulated. Figure 2.2 consists of two simulated images with approximately the same field

of view (128[Å] x 128[Å]); one for the 2[Å] resolution scope and the other for the 1[Å] resolution scope. The windowed region in each image contains the location of the edge-on hexagonal sheet and is the region over which the greyvalue intensity is profiled. The corresponding profiles in Figure 2.3 allow for a comparison of the differences between the two model scopes. The hexagonal sheet used in these simulations is approximately 20[Å] in breadth, and the atom positions in the amorphous background are identical in each simulation. The sheet's location is made apparent by the relatively constant oscillations seen in both profiles, where the greyvalue dips to near 0.80 repeatedly. The value of the

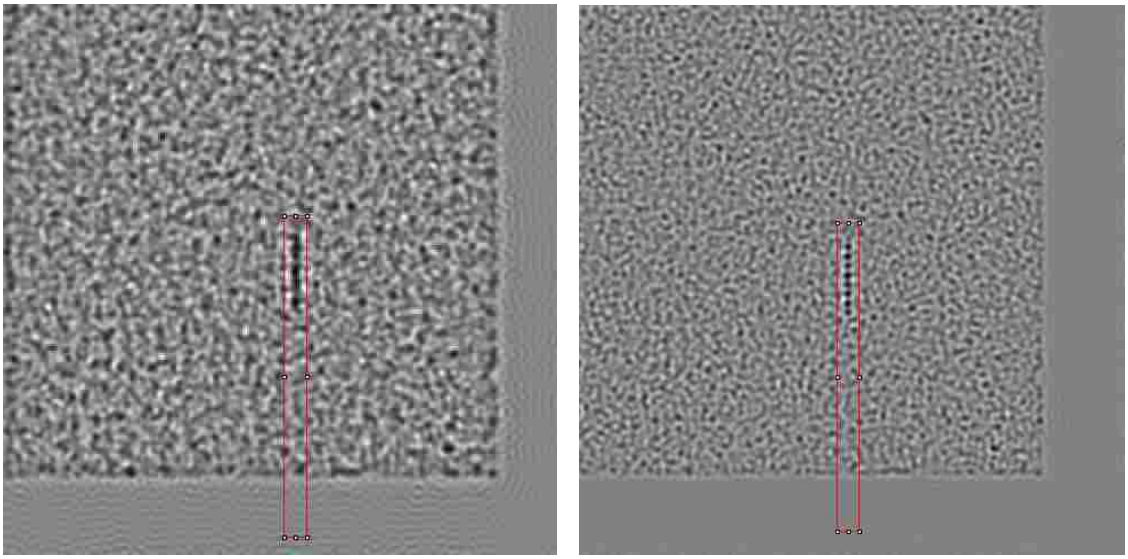

(a) **(b)**

Figure 2.2: (a) A simulated phase contrast image for an edge-on hexagonal sheet within amorphous material. The model scope has a resolution of about 2[Å]. The windowed region outlines the region over which the profile is to be taken, along the direction of the sheet. (b) The same as (a) except the model scope has a resolution of 1[Å] (field of view for both images is 128[Å]).

(a)

(b)

Figure 2.3: (a) The average greyvalue intensity profile along the direction of the sheet corresponding to Figure 2.2(a). The average intensity in the hole fluctuates around 1, as expected, and the relatively constant projected mass of the hexagonal sheet is seen in the oscillations around 0.80. (b) The same as (a) except corresponding to Figure 2.2(b).

darkest pixels along the sheet are actually approximately 0.40, as seen in line profiles shown in Figure 2.4. Here, this data represents the actual greyvalues along the linear feature in the image. The averaging process in the profiles from the windowed regions acts to blur this data, but provides a smoother curve.

The average intensity in the hole of each image is approximately 1, as expected. Thus, this profile measurement and others to follow are all interpretable in the sense that the difference in the greyvalue measured, relative to 1, is an indicator of strength of the scattering due to the projected atomic potential in that region.

Based on the shape and orientation of the sheet (Figure 2.1), we expected to see six strong troughs in the profiles, followed by less intense troughs on either end that tail off as the projected mass is less on the outer edge of the sheets. In fact, what we see is that for the case of the 1[Å] resolution model (Figures 2.2(b) and 2.3(b)), the sheet appears very clearly in the image and in profile. Compared to the 2[Å] resolution model (Figures 2.2(a) and 2.3(a)), there is more detail seen in the former, but the relative intensity compared to that in the hole is less. This is due to the fact that the 1[Å] resolution profile is averaged over twice as many pixels, and the improvement in resolution causes better localization of the sheet in projection.

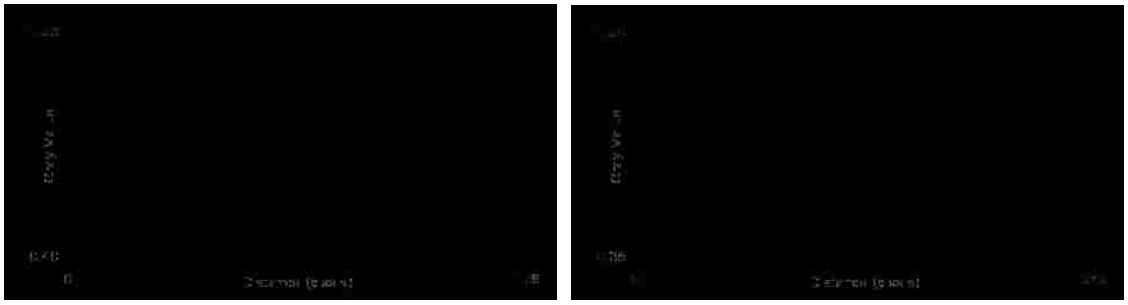

(a) **(b)**

Figure 2.4: (a) The greyvalue intensity profile along a line through the hexagonal sheet in Figure 2.2(a). (b) The same as (a) except corresponding to Figure 2.2(b).

While hexagonal sheets represent an isotropic shape of graphene, triangular sheets present a different shape that might arise under crystal growth conditions that lead to faceting. Figure 2.5 is a set of simulated images, one for each model scope, of an edge-on triangular sheet with the beam oriented along the vertical direction of the sheet in Figure 2.1. The corresponding average greyvalue intensity profiles, seen in Figure 2.6, again illustrate the improved resolution in the 1[Å] scope. Also, the sheet shape is somewhat visible in these profiles, where the relative intensity deviates from that in the hole less and less, as the projected potential becomes weaker along the sheet. Figure 2.7 represents line profiles through the edge-on sheets in Figure 2.5, and provides the actual greyvalues across the sheet relative to the hole.

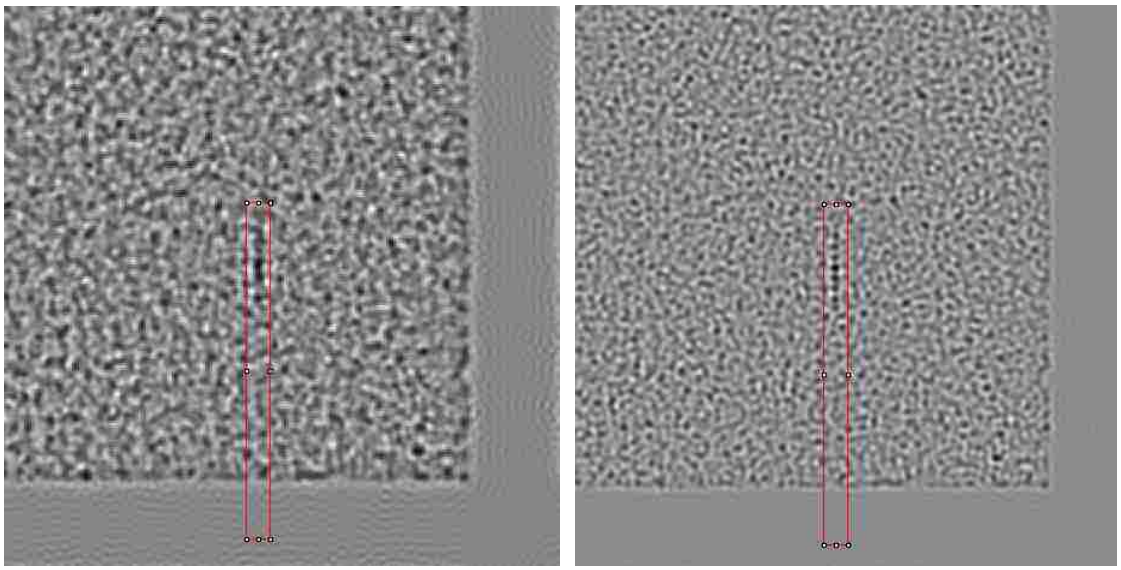

(a) **(b)**

Figure 2.5: (a) A simulated phase contrast image for an edge-on triangular sheet within amorphous material with a 2[Å] resolution model scope. (b) The same as (a) except the model scope has a resolution of 1[Å] (field of view for both images is 128[Å]).

In both cases in Figures 2.6 and 2.7, the triangular shape of the sheet is visible. Rather than observing troughs that maintain a roughly constant value over a defined region for the sheet, we see a slope of trough intensities corresponding to the decrease in projected

(a)

(b)

Figure 2.6: (a) The average greyvalue intensity profile along the direction of the sheet corresponding to Figure 2.5(a). The average intensity in the hole fluctuates around 1, as expected, and the decreased intensity of the troughs bracketing the central trough of the triangular sheet is indicative of the sheet shape. (b) The same as (a) except corresponding to Figure 2.5(b).

(a) **(b)**

Figure 2.7: (a) The greyvalue intensity profile along a line through the triangular sheet in Figure 2.5(a). (b) The same as (a) except corresponding to Figure 2.5(b).

potential along the triangular sheet. This is not resolved as well in the 2[Å] resolution image, but a net effect is observable in both the line profile and the window profile. Interestingly, the minimum intensity is approximately the same as that for the hexagonal sheet, where the triangular sheet had a height of approximately 20[Å]; this is similar to the 20[Å] breadth of the hexagonal sheet used in the previous simulations. The fact that the resulting greyvalues are the same for approximately the same amount of projected potential in both simulations provides some confidence that the differences in the profiles are real, and directly related to the shape of the graphene sheets. Even in the case of the lower resolution model images, shape differences can be seen in both the line and average window profiles that correspond to the graphene sheet shape.

Of course, the analysis thus far has focused on two different sheet shapes under very specific orientations. In an experimental image, it is not likely that edge-on sheets will always be in one of these atomic configurations, or orientations, relative to the electron beam. Figures 2.8, 2.9, and 2.10 are data representative of the triangular sheet from Figure

2.1(b) rotated by 90 degrees. This will still be an edge-on sheet in simulated image data, but should now have a maximum in projected potential on one side (with one of the seams or sides of the triangle being parallel to the beam) and fall off gradually along the sheet. Once again, the atom positions for the amorphous layer are exactly the same for each model data set.

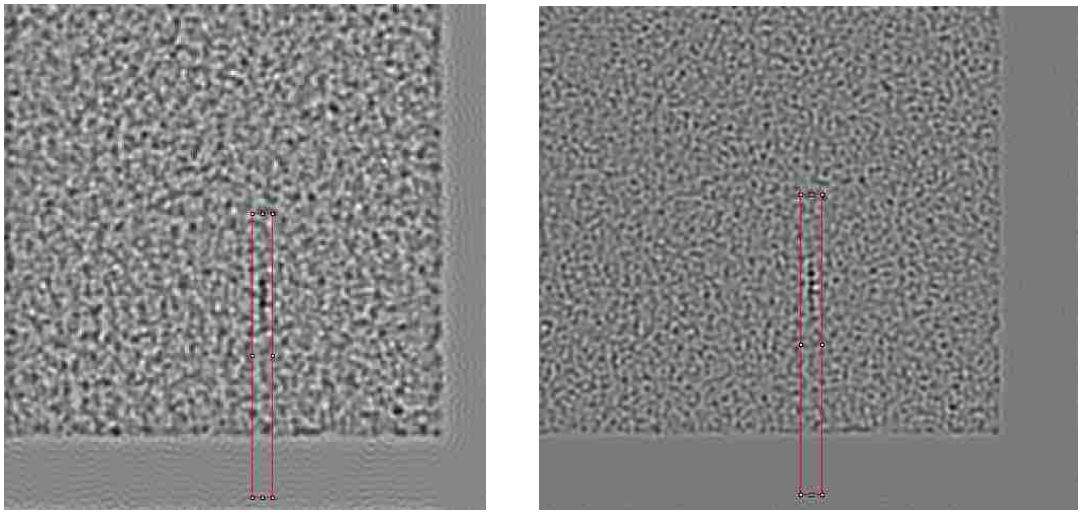

(a) **(b)**

Figure 2.8: (a) A simulated phase contrast image for an edge-on triangular sheet, rotated so that one of the sides is parallel to the electron beam, within amorphous material, with a 2[Å] resolution model scope. (b) The same as (a) except the model scope has a resolution of 1[Å] (field of view for both images is 128[Å]).

Each of the average window profiles (Figure 2.9) are difficult to analyze in determining the graphene sheet shape. Likely, this is due to the fact that the gradual falloff of the projected potential along the sheet becomes averaged out quickly by the amorphous background. In other words, with so few atoms comprising the sheet, and thus the atomic

columns, the surrounding amorphous material can promptly blur out scattering effects due to sheet shape. Thus, experimentally it would be critical to analyze graphene shape in a very thin amorphous layer, or better yet, as an isolated structure.

(a)

(b)

Figure 2.9: (a) The average greyvalue intensity profile along the direction of the triangular sheet imaged in Figure 2.8(a). Here, it is difficult to identify the sheet shape by simply looking at the profile. (b) The same as (a) except corresponding to Figure 2.8(b).

However, when comparing the greyvalue intensities along a line through the sheet (Figure 2.10), the high resolution case is able to discern the expected sheet shape. The

shape is not clear in the lower resolution profile. It is expected that this type of sheet shape would become easier to distinguish if the sheet were made larger. Then, there will be more atomic columns and a more gradual falloff in projected potential over a longer distance. Even in the lower resolution case, this will provide a greater distance over which to profile, and should aid in averaging out some of the contrast and interference effects arising from the regular arrangement of the rows of atoms.

2.2.2. Angle Statistics in Collections of Nanocones. Another way to delineate between two similar types of atom-thick structures, such as faceted and relaxed carbon nanocones, is to consider the statistics of measurements that might reveal characteristic patterns in TEM images. One example of this technique can be illustrated using simulated, phase contrast, TEM images of collections of relaxed and faceted carbon nanocones. By comparing histograms corresponding to the measurements of angles between linear features observed in simulated TEM images, it is possible to differentiate between the two structures. While this particular measurement may be useful only in the case of identifying collections of nanocones, it is an example of applied pattern recognition in images for the purposes of specimen characterization.

Both faceted and relaxed carbon nanocones have certain orientations under which their projected mass-thickness allows for the necessary contrast to stand out against an essentially amorphous carbon background. Some of these orientations give rise to adjoined linear features in phase contrast TEM images that have very specific angles between them, due to the molecular structure (Figure 2.11). The angles between these linear features are

(a) **(b)**

Figure 2.10: (a) The greyvalue intensity profile along a line through the triangular sheet in Figure 2.8(a). The sheet shape is apparent in the higher resolution model scope, but more difficult to observe in the lower resolution case. (b) The same as (a) except corresponding to Figure 2.8(b).

approximately 140˚ and 110˚ for the case of the faceted nanocone, and 113˚ and 150˚ for the case of the relaxed nanocone. Also of import is the fact that while the faceted nanocone has only five orientations under which it can be viewed down the seam, the relaxed nanocone has many more "equivalent" viewpoints that run along the seam direction. Thus, it is expected that high-angle incidences should be more prevalent in a collection of randomly-oriented relaxed cones, than for faceted cones.

Figures 2.12 and 2.13 compare simulated TEM images of collections of randomly-oriented nanocones and histograms of measured angles between linear features in each image. Adjoined linear features were chosen for measurement based on two criteria: (1) that there were two linear features, whose contrast made them stand out strongly against the background of the surrounding material, and (2) the linear features appeared to be part of the same structure or cone in that they appeared to branch away from a common point of

intersection. While this technique could be improved greatly with computer-aided pattern recognition, the shape of the histograms in each case is already fairly evident from this impartial analysis using the human eye.

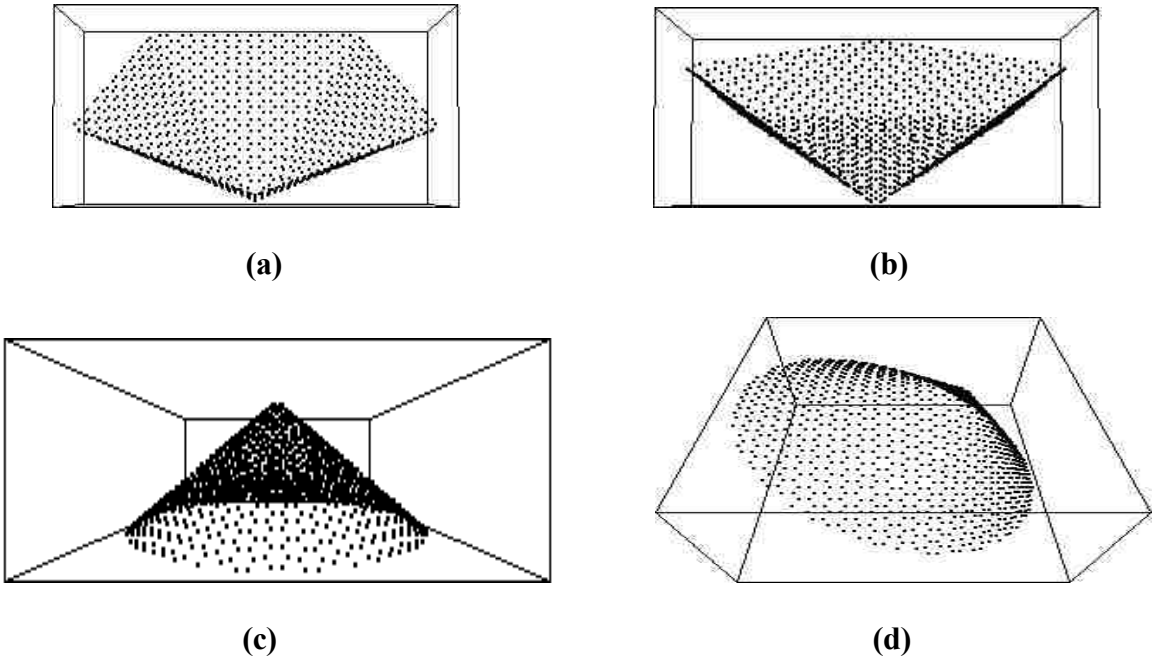

Figure 2.11: (a, b) Two orientations of a faceted nanocone that would give rise to adjoined linear features in phase contrast TEM images. The first is looking down one of the seams of the nanocone, while the other is looking down the back of a facet. (c, d) Two orientations of a relaxed nanocone that might lead to adjoined linear features in phase contrast TEM images. The first is with the cone viewed parallel to the base of the cone, and the second is viewed down the seam, or along the line from the bottom edge of the nanocone towards the apex.

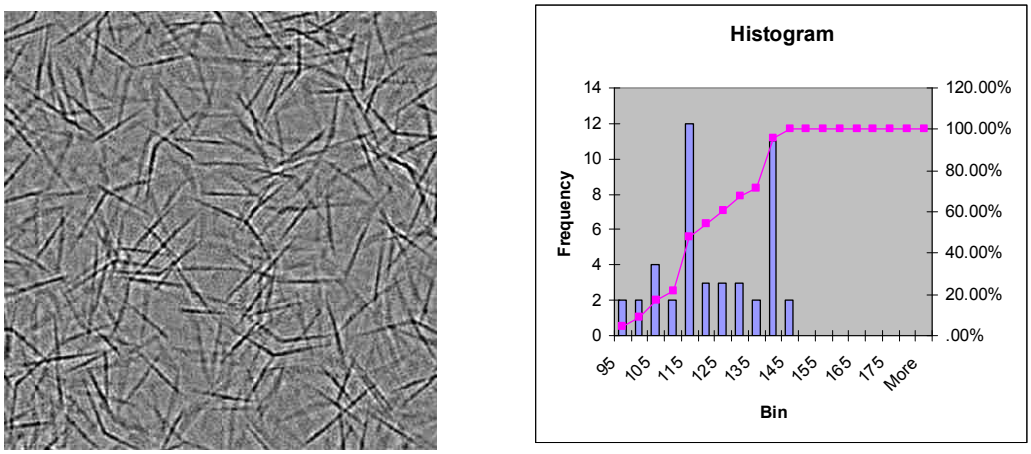

Figure 2.12: A simulated phase contrast TEM image of a collection of randomly-oriented, faceted nanocones and the histogram of observed angles between linear features (field of view is 256[Å]).

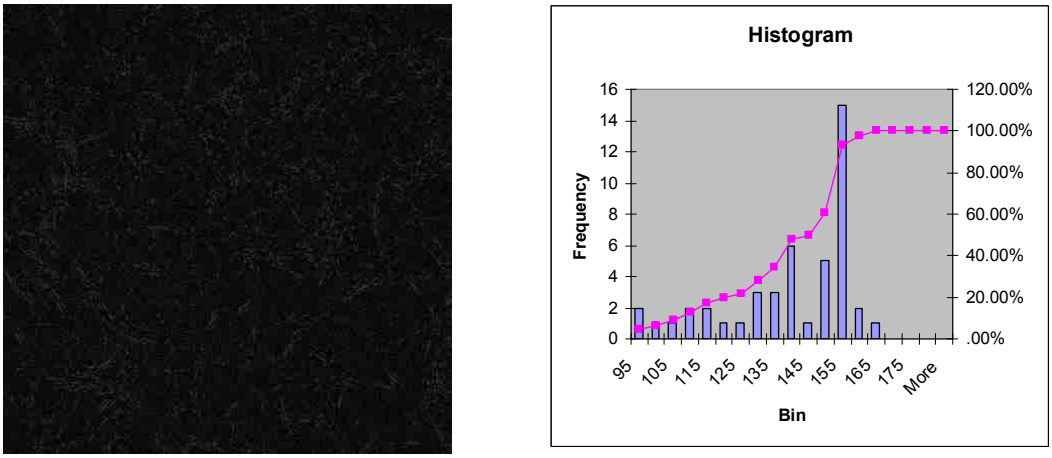

Figure 2.13: A simulated phase contrast TEM image of a collection of randomly-oriented, relaxed nanocones and the histogram of observed angles between linear features (field of view is 256[Å]).

One can see that there are many high-angle incidences and very few low-angle incidences for the case of the relaxed nanocone, while the faceted nanocone histogram indicates a much higher probability for measuring lower angles. Given a sample comprised of nanocones, or when analyzing these structures in the TEM, it may be possible to distinguish faceting from the more common relaxed configuration by analyzing the statistics of observed angles between linear features. Of course, this analysis has only considered single pentagonal defects. The inclusion of a cluster of similar defects within a sheet would change the cone apex angle, and thus the expected angles. However, combined with other image analysis techniques, such as profiling, this technique may still be useful for identifying faceting where very specific recurring angles are measured.

2.2.3. Faceting Evidence in Intensity Profiles. One can also examine both the faceted and relaxed structures discussed in the previous section by using intensity profile measurements, similar to those used in Section 2.2.1. It is likely that linear features appearing to intersect in TEM images of collections of atom-thick structures are coordinated, or are part of a single structure (i.e. nanocone). This is especially true in the case where there are recurring angles or regular relationships between the adjoined linear features. What is not necessarily obvious is whether these structures, being viewed down a preferential direction, might be faceted or relaxed around the defects that cause the deviation from the flat graphene structure. Here, intensity profile measurements from simulated TEM images of these structures provide a method for comparing and differentiating image signatures.

For this analysis, both the faceted and relaxed nanocone were embedded in an identical amorphous layer, and oriented so that the electron beam was directed down the seam of each structure (the orientations in Figure 2.11 (a) and (d)). Images were simulated for these object orientations using both model scopes (2[Å] and 1[Å] resolution), and both structures have the same number of atoms in projection down the seam. In order to examine contrast differences, intensity profiles were plotted using two line scans; one line scan that is tangent to the intersection of the linear features, and another that bisects the features. Figure 2.14 shows the 2[Å] resolution model TEM images and profiles for the faceted nanocone, while Figure 2.15 shows the same for the relaxed nanocone. The profile below each image corresponds to the pixel range indicated by the line in the image, and the line scans are orthogonal, as discussed above.

Comparing the results in Figures 2.14 and 2.15, some points of interest become immediately apparent. Firstly, the greyvalue corresponding to the apex of the faceted cone is darker (~ 0.13) than that of the relaxed cone (~ 0.23). Recall that the same number of atoms is projected along the seam in each case. Because these measurements are relative to the hole in each image, where the average greyvalue is 1.00, the faceted cone seam appears about 13% darker than the relaxed cone seam. Thus, in an experimental situation where the size of the cone is known with some certainty, images taken with the electron beam directed down the seam of the cone can be used potentially to verify whether the cone is faceted or relaxed.

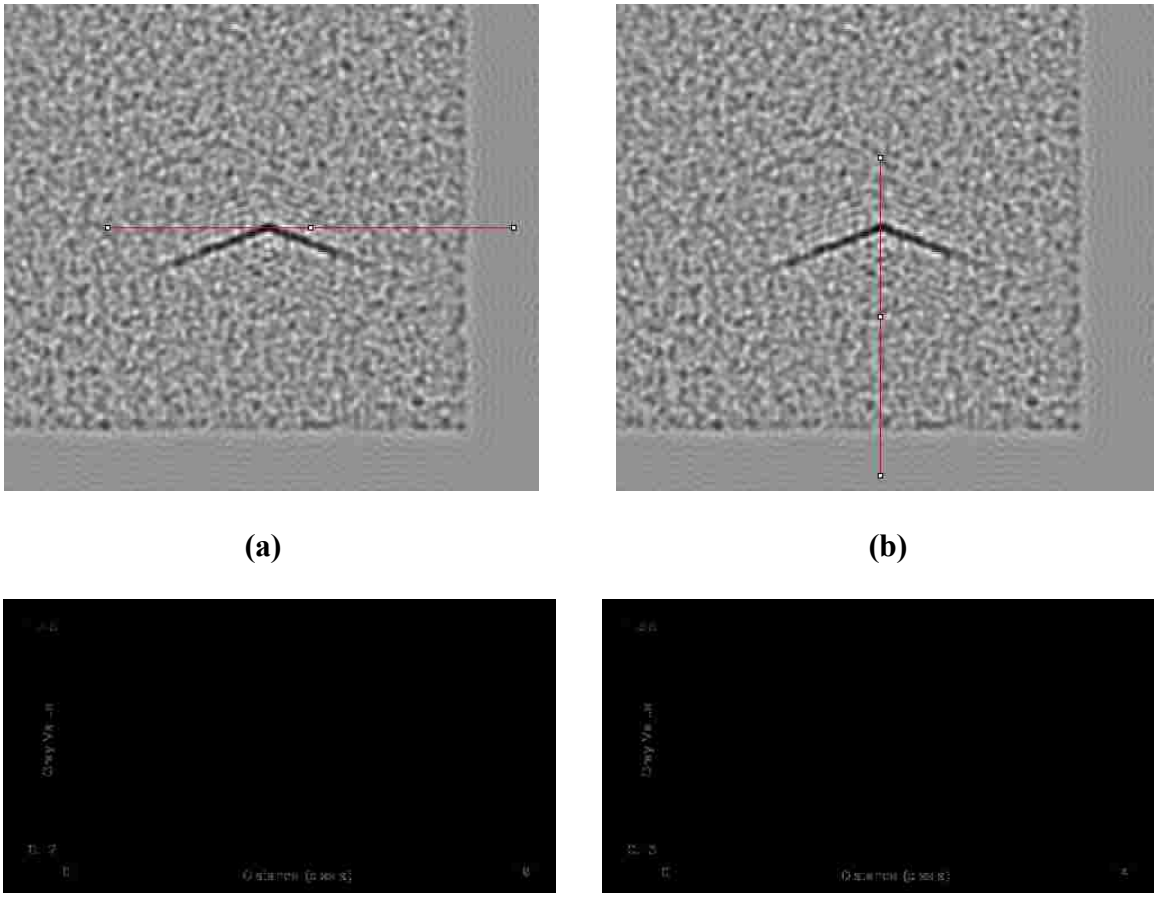

(a) **(b)**

(c) **(d)**

Figure 2.14: (a, b) Simulated TEM images of a faceted nanocone, viewed down the seam, using a model scope with a 2[Å] resolution limit (field of view 128[Å]). The red lines indicate the pixel range over which the orthogonal line scans are measured. The profile (c) corresponds to the horizontal line in (a) and the profile in (d) corresponds to the line in (b).

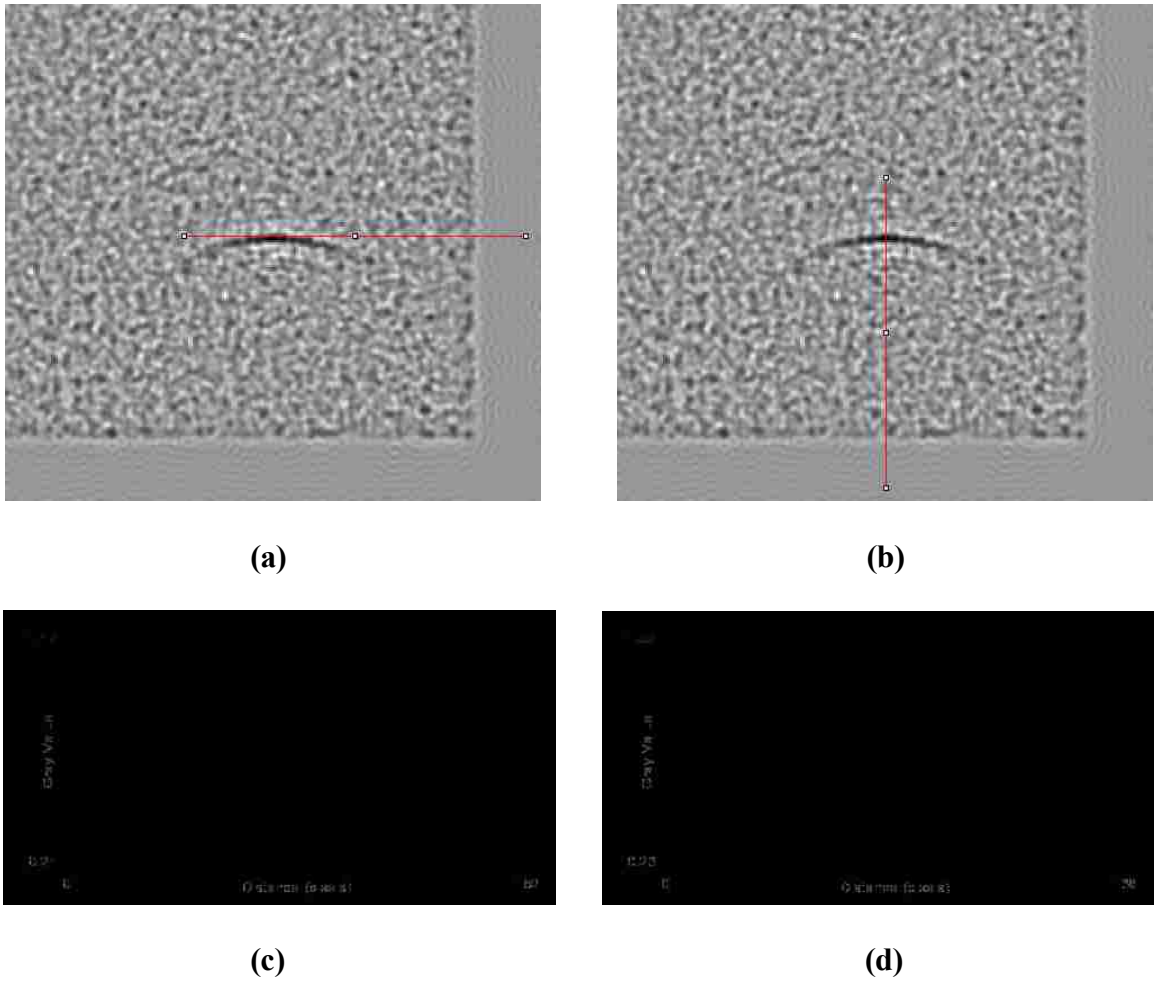

(a) **(b)**

(c) **(d)**

Figure 2.15: (a, b) Simulated TEM images of a relaxed nanocone, viewed down the seam, using a model scope with a 2[Å] resolution limit (field of view 128[Å]). The red lines indicate the pixel range over which the orthogonal line scans are measured. The profile (c) corresponds to the horizontal line in (a) and the profile in (d) corresponds to the line in (b).

Another interesting difference is the shape of the tangential, or horizontal, profile in each case (Figures 2.14(c) and 2.15(c)). Here, the trough centered on the seam of the cone is broadened because the line scan crosses other atomic columns near the seam. Meanwhile this effect is not as pronounced in the case of the faceted cone. This is due primarily to the fact that the faceted cone is made up of flat sheets that lie along a direction

moving away from the seam at a specific angle. When looking down the edge, or seam, of a relaxed nanocone, nearby atoms have only deviated slightly from a plane tangent to the edge of the cone. Gradually, the atoms deviate farther as one travels further away from the seam, resulting in what looks like intersecting lines in projection/TEM imaging. This result is fairly robust in that even if the faceted nanocone is not viewed exactly down the seam (slightly off due to misalignment in tilting), it should still retain the more abrupt drop in the tangential profile due to the nature of the sheets described above.

Figures 2.16 and 2.17 contain simulated TEM images and profiles, using a model scope with a 1[Å] resolution limit, of the same molecules and amorphous material analyzed in Figures 2.14 and 2.15. Observe that the broadening effect is still present around the seam of the relaxed nanocone. Thus, once again, the tangential line scan provides a method of determining whether intersecting line features in images might be part of a molecule that has been allowed to relax, or is faceted. However, the greyvalue intensity of the troughs corresponding to the seams in each case is nearly the same. The faceted seam still appears slightly darker, but is now only about 7% darker than the seam of the relaxed cone. Thus, the improvement in resolution makes it more difficult to simply use the greyvalue of the trough, relative to that in the hole, to identify curvature versus faceting in the nanocone.

In all of the above analyses, it is important to keep in mind that these are merely comparisons between different structures in simulations. Applying any of the results arrived at through these simulations requires the user to know something about the specimen they are analyzing. Linear features can arise in images from a variety of contrast

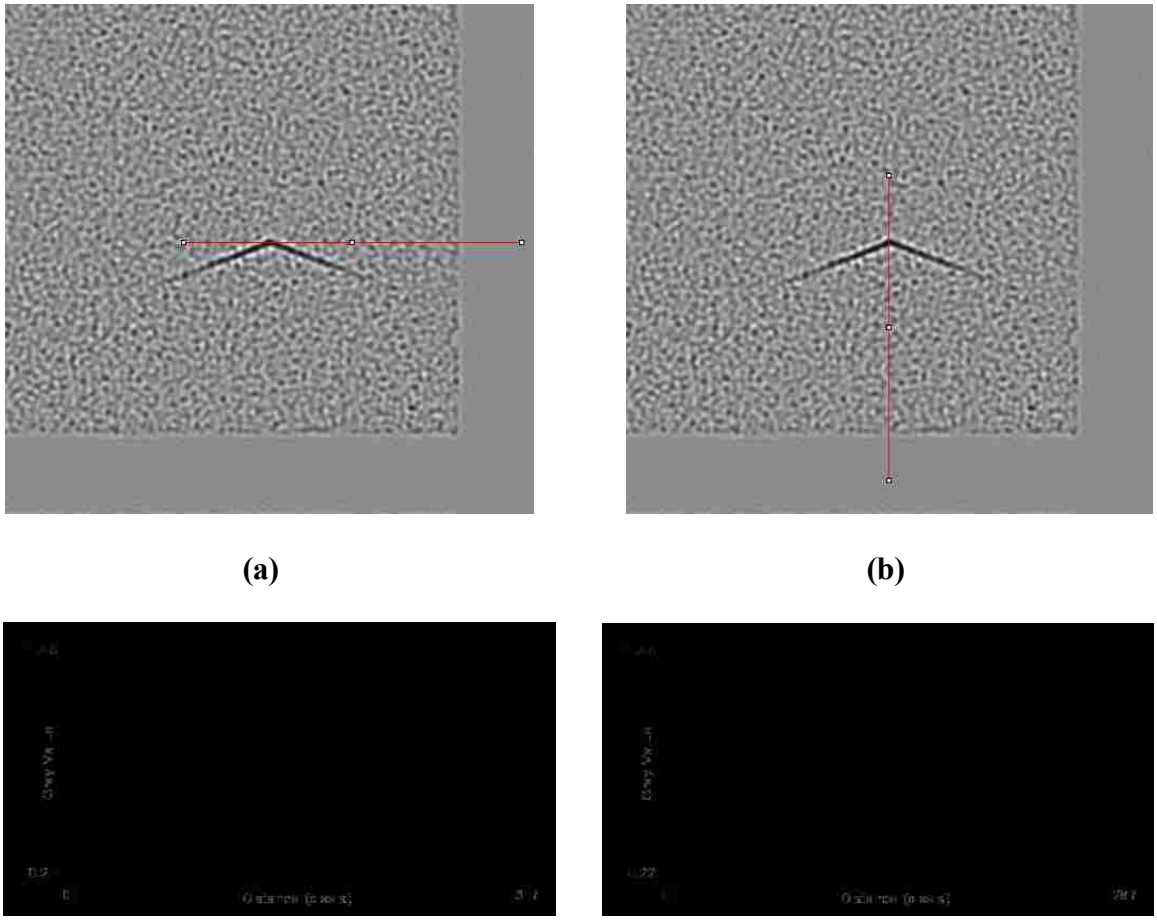

(a) **(b)**

(c) **(d)**

Figure 2.16: (a, b) Simulated TEM images of a faceted nanocone, viewed down the seam, using a model scope with a 1[Å] resolution limit (field of view 128[Å]). The profile (c) corresponds to the horizontal line in (a) and the profile in (d) corresponds to the line in (b).

mechanisms, or strange orientations between molecules. However, for the case of atom-thick carbon, the measurement of specific angles, and the orthogonal greyvalue intensity profiles can provide a wealth of information about structure and characterization. A careful analysis of other explanations for the linear features must always be undertaken experimentally, while other analysis methods (i.e. electron diffraction, EELS) may help confirm conclusions drawn from these types of image measurements in any real specimen.

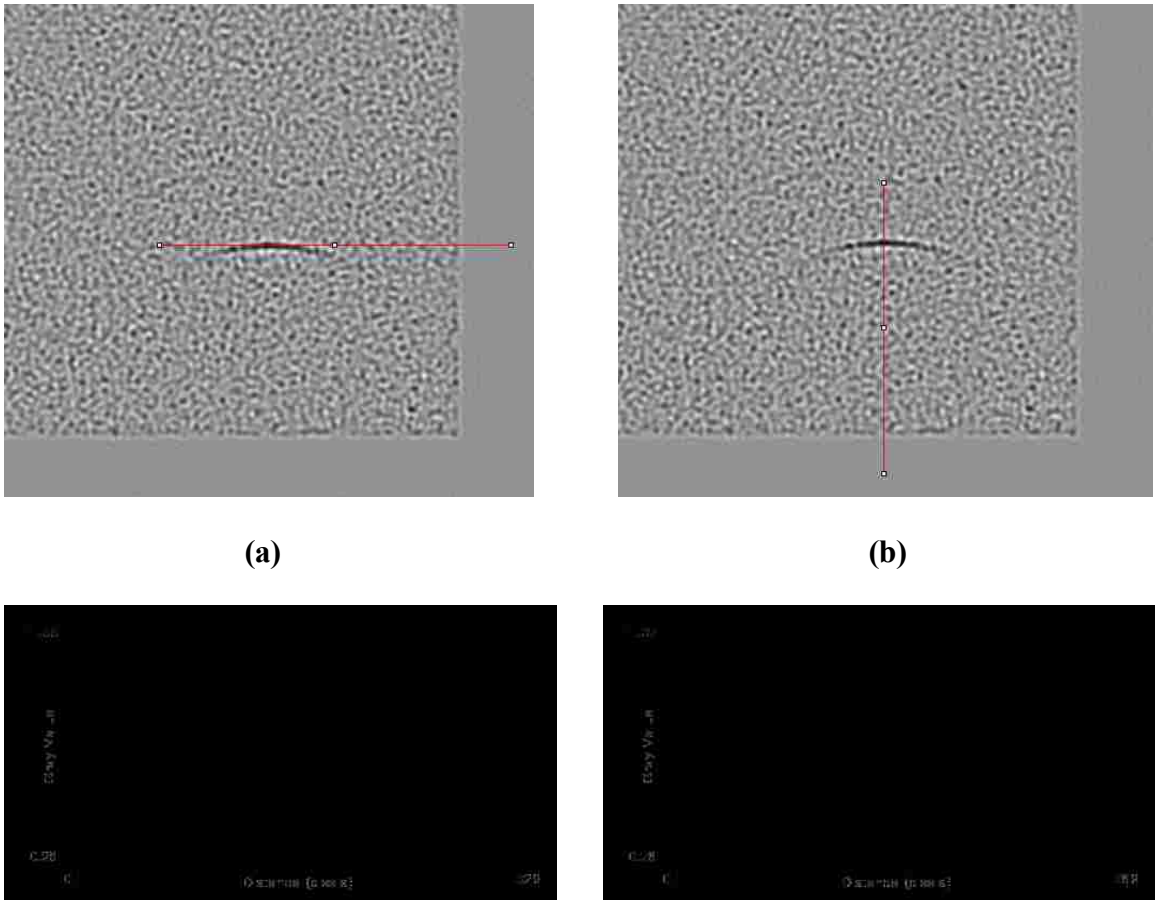

(a) **(b)**

(c) **(d)**

Figure 2.17: (a, b) Simulated TEM images of a relaxed nanocone, viewed down the seam, using a model scope with a 1[Å] resolution limit (field of view 128[Å]). The profile (c) corresponds to the horizontal line in (a) and the profile in (d) corresponds to the line in (b).

2.3 DIFFRACTION PROFILES FOR ATOM-THICK CARBON MOLECULES

Given atom positions for a single molecule, Debye diffraction profiles can be calculated, providing a means for examining crystal shape effects that might manifest in reciprocal space. Because the Debye scattering formula (Equation 1) is essentially an infinite molecule calculation, which averages over all possible orientations of the structure, it is sufficient to calculate profiles for a finite set of different molecules and compare the

results directly. These results may then be compared directly to experimental selected-area diffraction data from collections of similar nanostructures in order to identify trends and characterize materials.

Here, profiles have been calculated for a hexagonal graphene sheet, a triangular graphene sheet, a curved triangular sheet (a triangular-shaped conic section), and a faceted nanocone. Comparisons between the first two reveal some of the subtle differences in reciprocal space that arise due to sheet shape. The curved triangular sheet can be compared to the flat triangular sheet in order to investigate effects in reciprocal space due to sheet curvature. Lastly, coherence effects, caused by the relationship between lattice fringes of neighboring sheets, can be measured and explained using the faceted nanocone Debye profile. This might provide a means for gauging regular faceting in collections of carbon nanostructures.

2.3.1. Graphene Shape Effects in Debye Models. Figures 2.18 and 2.19 are Debye diffraction profiles for a hexagonal and triangular sheet respectively. Evident in each of these are the three peaks corresponding to the first three observed graphene lattice periodicities ((100), (110), and (200), or 2.13[Å], 1.23[Å], and 1.06[Å] respectively). Both molecules used in the calculation of these profiles had approximately the same breadth (~20[Å] across), though the triangular sheet has fewer atoms due to its shape. In order to compare these two profiles directly, the triangular sheet profile must be scaled to account for scattering by the same number of atoms as the hexagonal sheet. This can be accomplished using a multiplicative constant derived from the number of atoms in each

molecular model. The justification for this is that the amount of scattering is proportional to the number of atoms in the model.

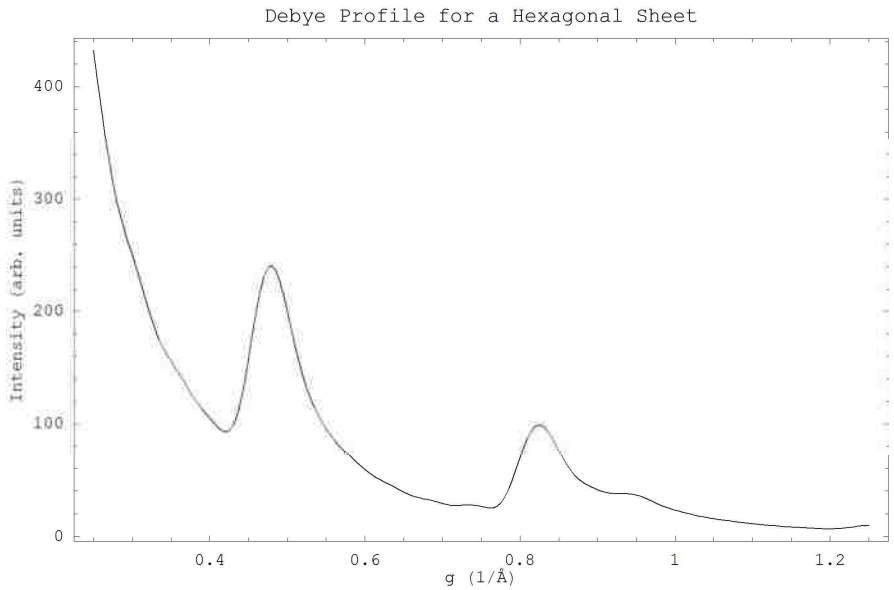

Figure 2.18: Debye diffraction profile for a hexagonal sheet. The first three expected graphene peaks are visible.

After scaling the triangular sheet profile, the difference between this and the hexagonal sheet profile is calculated and plotted in Figure 2.20. Here, the graphene peak shape differences between the hexagonal sheet and the triangular sheet are evident, particularly on the leading edges of the (100) and (110) peaks, and at the peaks themselves. The root mean square difference between the two profiles is 6.89[intensity units], while the area of the residuals, or difference curve, represents about 4.5% of the total area of the hexagonal profile. These types of differences, while small, can be significant when

comparing models to experimental data. The peak shapes are different because of the different crystal shapes.

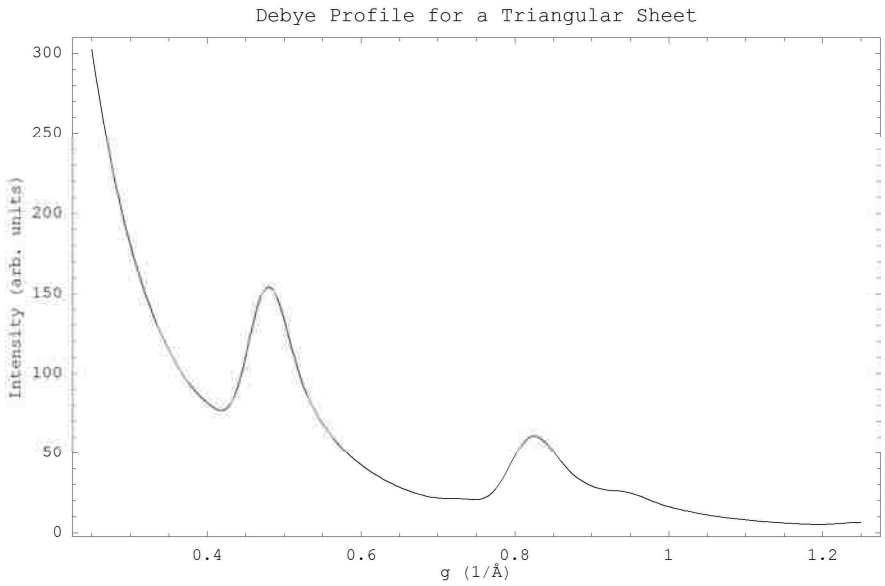

Figure 2.19: Debye diffraction profile for a triangular sheet. The first three expected graphene peaks are visible.

While some of these differences can be lessened by choosing an alternate size for the triangular sheet, there is a fundamental peak shape difference that will merely be scaled by changing the size of the sheet. This is an important effect to be aware of when analyzing collections of atom-thick crystals as average sheet shape will affect selected-area diffraction data from the specimen.

2.3.2. Curvature in Diffraction Profiles. In a method identical to that utilized in Section 2.3.1, it is possible to calculate a diffraction profile for a triangular-shaped conic section,

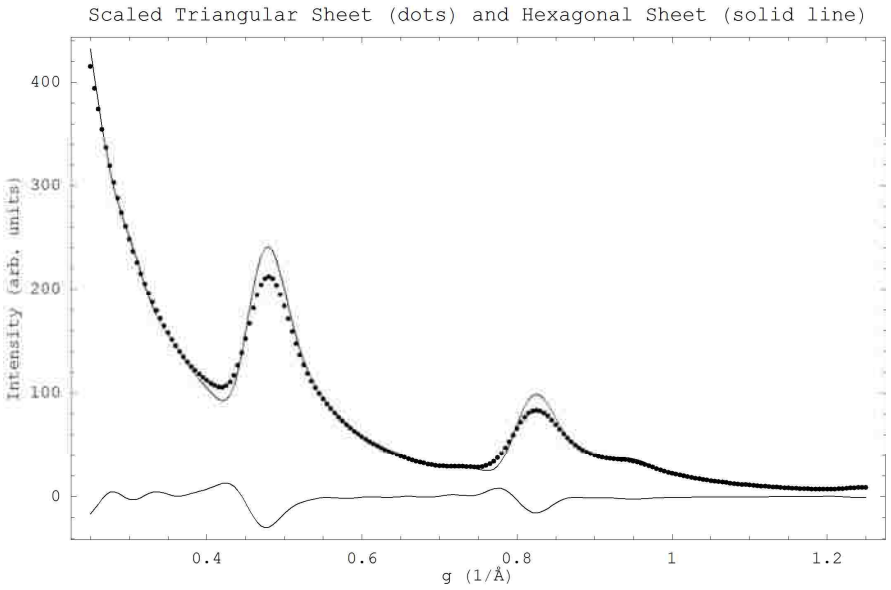

Figure 2.20: The scaled diffraction profile for the triangular sheet (dotted line) plotted with the hexagonal sheet profile (solid line). The lower curve is the difference between the two profiles.

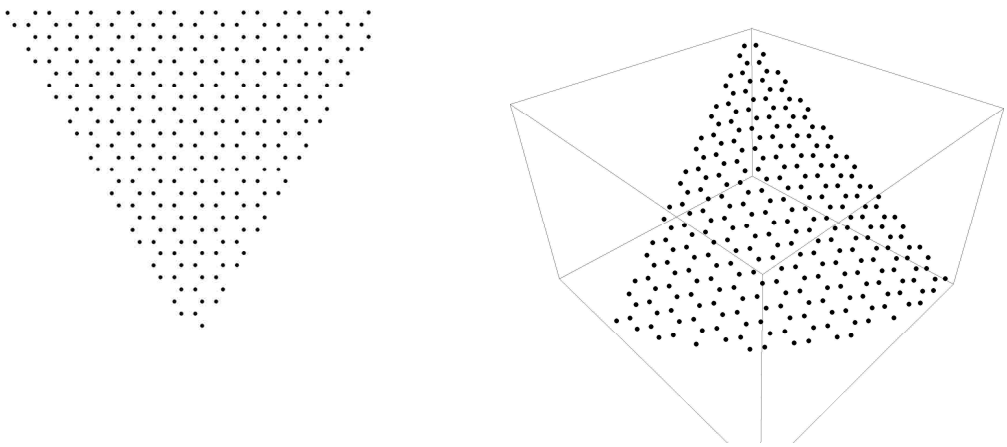

Figure 2.21: Atomic models for a flat triangular sheet and a curved, triangular, conic section used for the calculation of diffraction profiles.

which amounts to a triangular sheet with some curvature (Figure 2.21). Residuals seen between the profiles of these two molecules should be indicative of the effects of curvature on diffraction data, at least for small deviations from sheet flatness. Once again, this type of knowledge is useful when characterizing an experimental material, as improvement in fitting selected-area diffraction data may be realized given an understanding of how these effects manifest.

The diffraction profiles for the flat triangular sheet (dotted line) and the curved triangular molecule (solid line), and the difference between the two profiles, can be seen in Figure 2.22. The flat triangular profile has been scaled to account for scattering by the

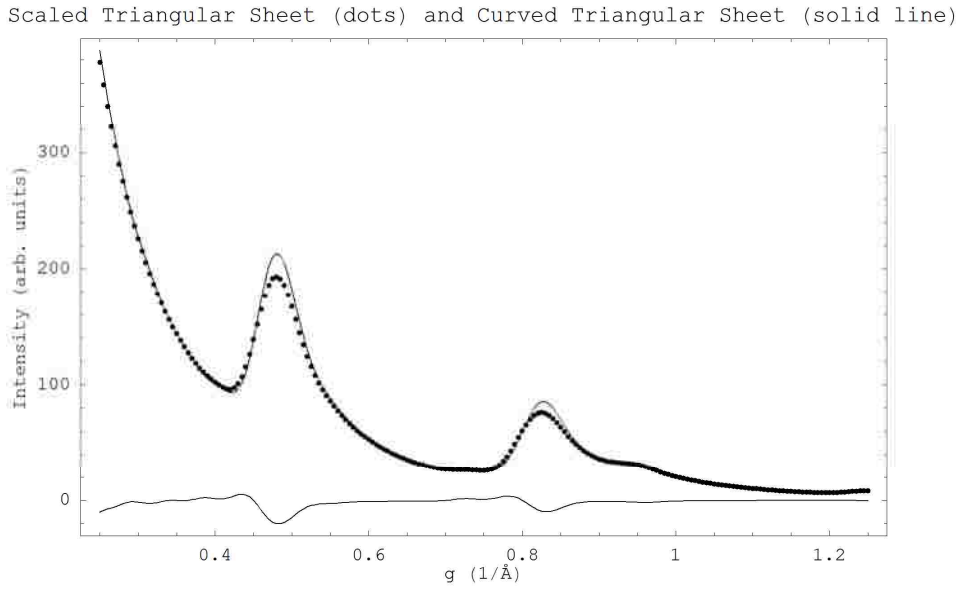

Figure 2.22: The scaled diffraction profile for the triangular sheet (dotted line) plotted with the curved triangle profile (solid line). The lower curve is the difference between the two profiles.

same number of atoms. The root mean square difference between the two profiles is 4.62[intensity units] in this case, and the area of the residuals represents about 3.5% of the total area of the curved triangle profile. More interestingly, however, is that the differences appear to be on the tailing edge of the graphene peaks. Whereas the triangular sheet shape examined in Section 2.3.1 seemed to affect the leading edge of the diffraction peaks (relative to the hexagonal profile), it appears that curvature serves to broaden the tailing edge of the graphene peaks with respect to the flat molecule. Experimental diffraction data from atom-thick structures with some degree of curvature would likely show similar deviations from a flat sheet model, and could be characterized as such.

2.3.3. Coherence Effects in Debye Models. Faceting could be described as an example of "severe" curvature, where flat graphene sheets are seamed together, branching off of a pentagonal, or some other defect. If the type of defect occurs with some regularity in a collection of atom-thick carbon nanostructures, it is possible one could find signatures of this structural phenomenon in diffraction data. A simple model to consider is that of a collection of faceted nanocones. The Debye diffraction profile for a faceted nanocone, made up of five triangular sheets, can be seen in Figure 2.23. When comparing this to the Debye pattern for a triangular sheet (Figure 2.19), the immediate difference is observed on the tailing edge of the (110) peak, around $0.87[\text{Å}^{-1}]$. This new peak arises due to the coherence between neighboring sheets that are seamed together.

One method of visualizing this coherence effect is by looking at the 3D reciprocal lattice for the faceted nanocone. In Figure 2.24, both the real space and a portion of the

reciprocal space crystal lattice for a faceted nanocone are shown. The reciprocal lattice is composed of rel-rods, corresponding to the lattice spacings for each sheet. Here, only the rel-rods for the (110) lattice spacing are shown. While the rel-rods are shortened in this image, for display purposes, it is apparent that the rods will undergo double intersections at a reciprocal distance slightly beyond the (110) lattice spacing, or center of those rods. When averaging this molecule over all possible orientations in the Debye model, there will be a "coherence spike" at this reciprocal distance, resulting in the satellite peak seen in the faceted nanocone Debye calculation.

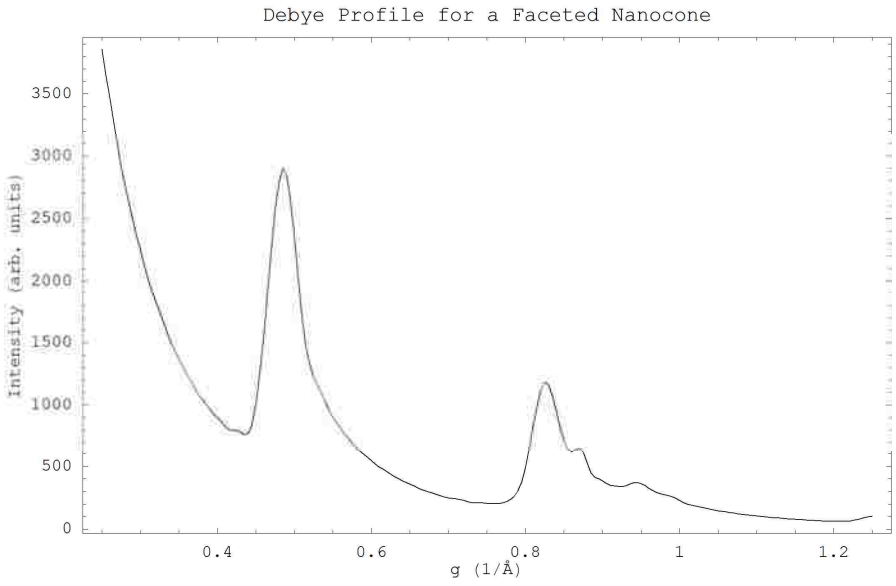

Figure 2.23: The Debye diffraction profile for a faceted nanocone. The faceted nanocone is made up of five triangular sheets that make regular angles with their nearest neighbors. This leads to the occurrence of the feature at 0.87[$Å^{-1}$].

In order to quantify how this effect manifests between two sheets that are seamed together, Debye diffraction profiles were calculated for the two structures shown in Figure 2.25. Here, the two facet structure is composed of identical triangular sheets, as if part of a faceted nanocone with a single pentagonal defect. The single triangular sheet is identical in size to the two making up the faceted structure. The diffraction profile intensities for the single sheet are again scaled by a multiplicative factor to account for scattering by the same number of atoms. Thus, in comparing the two profiles in Figure 2.26, the differences represent coherence effects due to the coordination between the faceted sheets, since each structure really consists of a different number of triangular sheets.

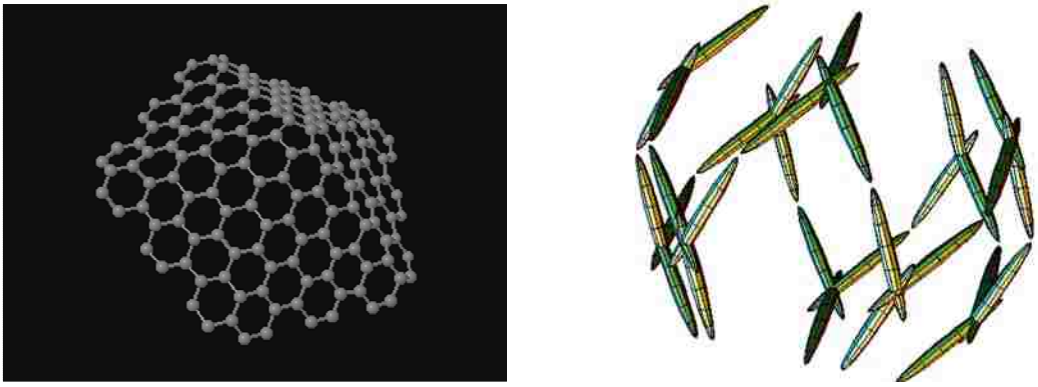

Figure 2.24: The atomic lattice of a faceted carbon nanocone, and a portion of the reciprocal space lattice. The reciprocal lattice, composed of rel-rods, illustrates how the near double-intersections lead to “coherence spiking” and the satellite peak seen in the diffraction model.

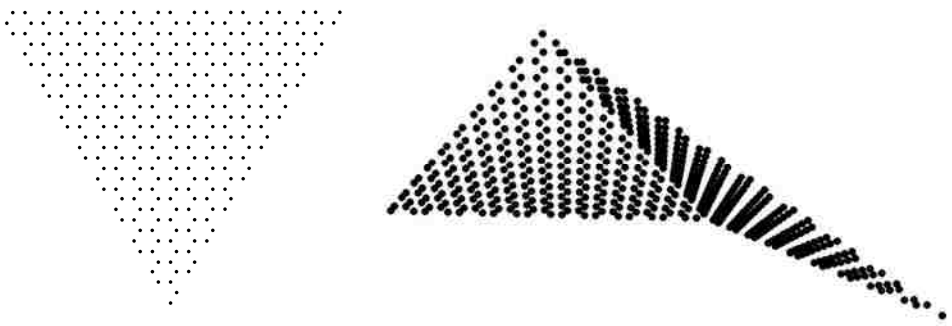

Figure 2.25: Atomic models for a flat triangular sheet and two facets of a faceted nanocone. Each facet is identical to the solitary triangular sheet.

Evident in the residuals between these two profiles is the same satellite peak seen in the faceted nanocone profile. The position of this peak is actually sensitive to the angle between the sheets. As the angle between the sheets changes, the relative position of the rel-rods changes in reciprocal space, as well, causing the location of the intersection in reciprocal space to shift. In a large collection of these molecules, this is a feature that would be visible, and useful in characterizing structure. If the angle between sheets is not consistent or recurring in a larger collection, the various coherence effects should add and blend into the background of the high-frequency tail. This amounts to the Fourier phases between neighboring sheets being fully randomized in the specimen.

This can be seen mathematically by looking at a 1D case, where a real function, $f(r)$, representing a sheet, and its Fourier transform,

$$F(k) = \int_{-\infty}^{\infty} f_i(r) e^{2\pi i k(r-r_i)} dr \qquad (2)$$

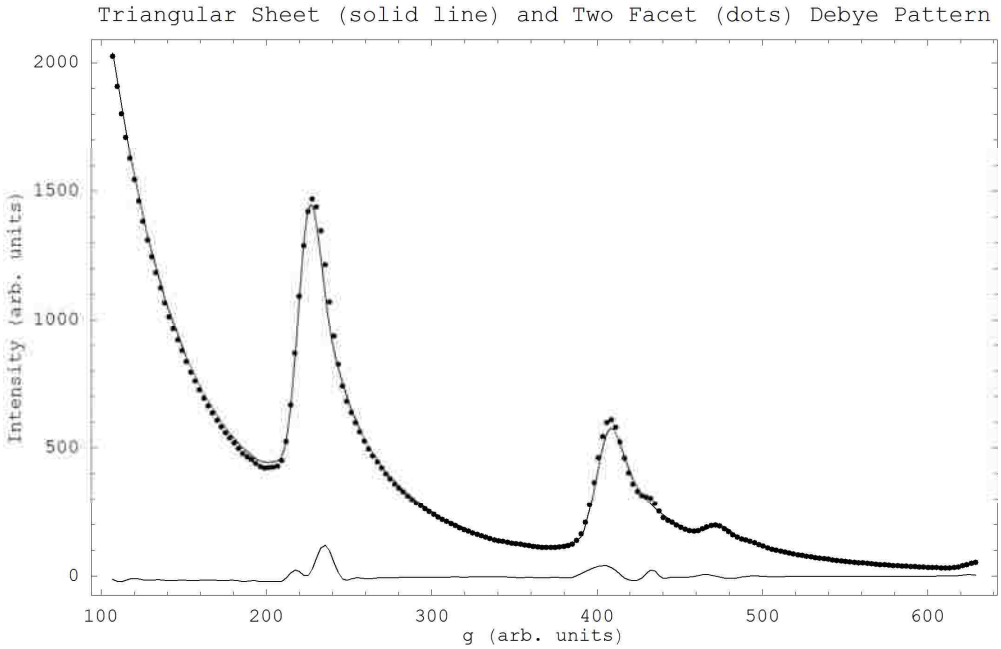

Figure 2.26: Debye diffraction profiles for a triangular sheet (solid line) and the two facet molecule (dotted line). Because both molecules are really just triangular sheets, the differences represent coherence effects that arise due to inter-sheet coordination.

can be used to write an equation for the 1D power spectrum of a collection of *N* objects,

$$F_T^*(k)F_T(k) = \left\{ \int_{-\infty}^{\infty} \sum_{i=1}^{N} f_i^*(r) e^{-2\pi k(r-r_i)} dr \right\} \left\{ \int_{-\infty}^{\infty} \sum_{j=1}^{N} f_j(r) e^{2\pi k(r-r_j)} dr) \right\} \tag{3}$$

This formula reduces to,

$$F_T^*(k)F_T(k) = N\left(F^*(k)F(k)\right)\left[1 + (N-1)\left(\sum_{i=1}^{N} \sum_{j=1, j\neq i}^{N} 2\cos\left(2\pi k(r_i - r_j)\right)\right)\right] \tag{4}$$

where the cosine term vanishes when there are enough sheets to sufficiently randomize the part of the phase, $r_i - r_j$. This same effect will occur when phases are fully randomized in 3D, meaning the deviations from a flat sheet model for a larger ensemble of randomly-oriented graphene sheets will decrease.

2.4 SUMMARY

Greyvalue intensity profiles in simulated, phase contrast, TEM images of edge-on atom-thick structures have been utilized to characterize a variety of structural aspects. Intensity profiles along edge-on graphene sheets are able to distinguish sheet shape; in this case, between hexagonal and triangular sheets. This type of measurement could be utilized in characterizing linear features seen in TEM images of collections of carbon nanostructures. When used in combination with diffraction data, which aids in confirming the presence of atom-thick structures, this technique would detail the structure of the individual molecules and perhaps shed light on formation mechanisms, or growth conditions.

Statistical measurements, such as the range of angles observed between linear features in TEM images, can also provide a method of characterizing collections of carbon nanostructures. In this work, separate collections of faceted and relaxed nanocones were shown to have different characteristic histograms of measured angles. Given the models of the faceted and relaxed nanocones, there is an expectation as to what angles are likely to be observed and the orientations that give rise to these features. This type of information could be used to gauge faceting in a collection of atom-thick carbon molecules, especially

when combined with the orthogonal intensity profiles of adjoined linear features. These intensity profiles reveal some of the image signatures of curvature, where faceting can be thought of as an extreme case of curvature.

Simulations are also useful in providing a set of expectations for electron diffraction data from collections of carbon nanostructures. Changes in peak shape due to changes in crystal shape can be quantified and utilized in characterizing experimental data. Also, effects from the curvature of atom-thick structures manifest due to relationships between adjacent sheets.

All of these models suggest that there is structural information beyond simple lattice periodicities and image features to be discovered in data from collections of carbon nanostructures. The diffraction modeling techniques, combined with the profiling techniques discussed in the earlier part of this chapter, offer the researcher a set of methods for analyzing collections of carbon nanostructures. The information presented here can be used as a stepping stone for further models that may be tailored for characterizing specific materials and dealing with challenges presented therein.

3. ELECTRON DIFFRACTION OF NANOCRYSTALLINE GRAPHITIC STARDUST

Presolar graphite spherules are a subset of graphitic stardust exhibiting an intriguing micron-sized nanocrystalline core that is surrounded by concentric graphitic layers, similar to those of a carbon onion (Bernatowicz, et. al. 1996; Croat, et. al. 2005; Fraundorf et al. 2000; Fraundorf & Wackenhut 2002). These grains are presolar as indicated by isotopic measurements being significantly different from solar values (i.e. C^{12}/C^{13} < solar = 89). The *r* and *s* type nuclear processes required to explain these isotopic ratios suggest grain-forming regions of red giant (AGB) atmospheres as a likely point of origin for these particles (Bernatowicz, et. al. 1996).

Selected-Area Electron Diffraction data from the cores of micron-sized, core-rim, graphite spherules (Figure 3.1) has been shown to exhibit (hk0) in-plane graphite periodicities. Absent in this data is any evidence of (002) graphitic layering, which is observed as a broadened feature even in amorphous carbon. Azimuthally-averaged diffraction data reveals high-frequency tails on each of the graphene peaks, a crystal shape effect characteristic of atom-thick structures. Thus, diffraction indicates the cores are comprised primarily of unlayered graphene (Bernatowicz, et. al. 1996; Croat, et. al. 2005). The left half-width at half maximum can be used to gauge the average size of the diffracting crystals, typically 2-4[nm] in core diffraction data. How one could grow a grain of this size (~1 micron) and suppress all graphitic layering is a mystery for materials engineering, as well as astrophysicists.

Previous diffraction analyses on these grains have focused on examining the differences between the experimental data and a flat, graphene diffraction model (Bernatowicz, et. al. 1996; Mandell, et. al. 2006). These differences are significant, especially on the leading edges of the (100) and (110) graphene peaks. One thought is that the residuals, or differences between the flat sheet model and experimental data, could be explained as being the result of diffraction from another crystallite with graphene-like periodicities, or carbon atoms that fill the gaps between the graphene sheets. Other attempts have been made to improve the model by considering two different sheet sizes, or a logarithmic distribution of sheet sizes, though no significant improvement in fitting has been realized in these models (Mandell, et. al. 2006).

Here, the experimental diffraction data is analyzed for the presence of other carbon species, including higher-order graphite periodicities, and any other peaks that might identify another crystallite. In addition to there being no evidence for other diffracting crystals in the data, the first six expected graphene periodicities are identified. Improvements in modeling the diffraction data are also realized by examining graphene sheet shape effects; comparing Debye diffraction models for hexagonal sheets and triangular sheets to the experimental data. A significant improvement in RMS fit is achieved using triangular sheets, indicating that most of the sheets contributing to diffraction are in some anisotropic form (non-hexagonal), possibly triangular. Also investigated is how the coherence between periodicities across bent crystals might contribute to diffraction here, and whether they could potentially explain remaining residuals.

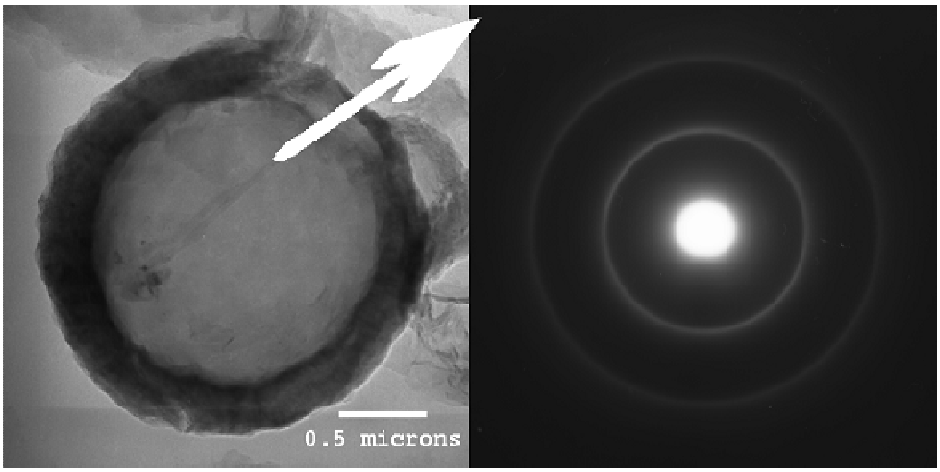

(a) **(b)**

Figure 3.1: (a) A TEM image of a core-rim graphite spherule. The rim is made up of concentric graphitic layers, similar to those of a carbon onion, while the core is comprised of unlayered graphene. (b) A selected-area diffraction pattern from the core structure. Absent is any evidence of (002) graphitic layering.

3.1 GRAPHENE PERIODICITIES IN CORE ELECTRON DIFFRACTION DATA

Azimuthally-averaged diffraction data from the cores was analyzed for evidence of other peaks to determine whether another crystallite might be contributing significantly to scattering. Diamond has strong diffraction peaks corresponding to periodicities of 2.06[Å], 1.26[Å], and 1.07[Å], which are similar to those of graphene, yet should be resolvable if present. Diffraction data was taken using a Phillips EM 430ST with a point resolution of about 0.2[nm], using 300keV electrons, and recorded on photographic film. Images recorded on film were then digitized at 2400[pixels/in] as 16-bit greyvalue data and loaded into Mathematica for azimuthal averaging. The digitization process results in a linear correlation between greyvalue intensity and time of exposure, whereas the film response is typically logarithmic (Hunton, 2004).

Figure 3.2 represents a typical example of the result of this process, where the first six expected graphene lattice spacings have been identified and labeled. This data has been examined down to the level of noise in the image (fluctuations < 1% of average greyvalue in the diffraction pattern) and searched for any peaks that might indicate the presence of another crystal structure, but nothing has been found to date.

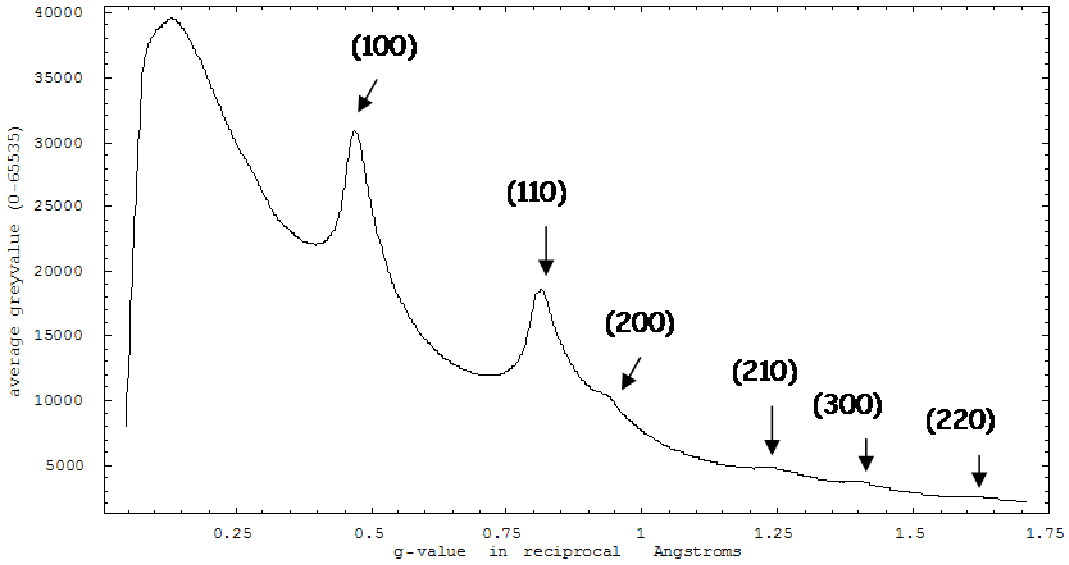

Figure 3.2: Azimuthally-averaged diffraction data from the presolar cores. Identified are the first six expected graphene lattice periodicities. No evidence has been found for any other crystallites contributing significantly to diffraction.

3.2 SINGLE MOLECULE BEST FITS

In order to examine improvements in fitting experimental data with different graphene shapes, a spline-fitting routine was created in Mathematica. For each molecule to be investigated, two Debye diffraction profiles (Equation 1) were calculated; one for a small version of the molecule and another for a larger version. These are chosen so that the

likely best fit size would fall between these two molecule sizes. Backgrounds are subtracted from each of these model profiles because the fitting routine will later need to consider the background in the experimental data, which is likely very different from that in the Debye model. The fitting routine tracks the changes in the shape of the diffraction profiles between the small and large molecule, and constructs a linear interpolation list, which allows for the display of any profile for a molecule with a size between the sizes of the endpoint molecules. This interpolation list is used to determine the best fit profile and corresponding molecule size for experimental diffraction data by using a least squares minimization. The resulting model and experimental profiles can then be overlayed, and residuals, or differences between the model and experimental data, can be used to quantify the performance of the fit. Also, the residuals identify shortcomings in the fitting from that particular model, and serve as a means of comparison between other model molecules that might be employed.

3.2.1. Hexagonal Flat-Sheet Model Best Fit. Because the diffraction data consists of graphene periodicities, an absence of (002) graphitic layering, and high-frequency tails trailing the peaks (indicative of atom-thick structures), a good first model is a hexagonal graphene sheet. This shape of graphene can be considered isotropic in that there is no preferential growth direction (Figure 2.1). Measured across their middle, molecular models of approximately 11[Å] and 42[Å] hexagonal graphene were constructed. Debye diffraction profiles were calculated for each of these, to be used as the endpoint patterns in the fitting routine. The results of the fitting routine applied to the experimental data are shown in Figure 3.3.

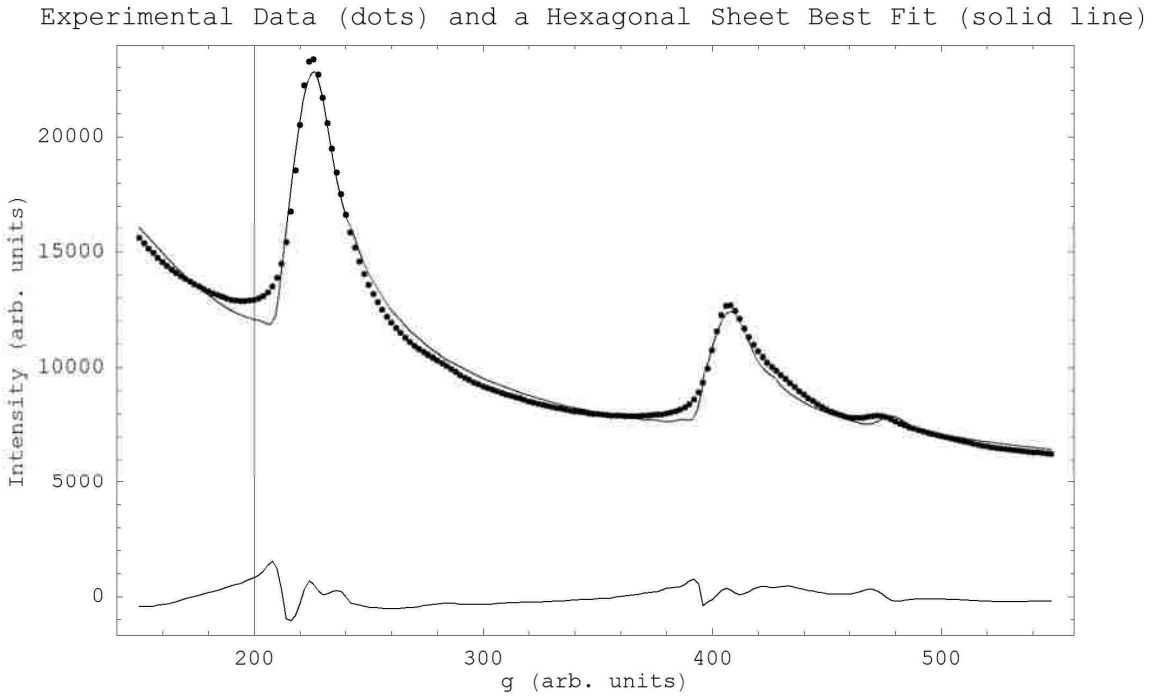

Figure 3.3: Experimental core diffraction data (dotted line) and a hexagonal sheet best fit (solid line). The fitting routine finds the best fit and molecule size by a least squares method. The lower curve represents the residuals between the two profiles.

Confirmed in this analysis are the residuals observed in prior work using a Warren model for graphene peak shapes (Mandell, et. al. 2006). The differences occur primarily on the leading edges of the (100) and (110) peaks, along with some mismatch at the graphene peaks themselves. Here, the RMS difference between the data and the fit is 382[intensity units], and the total area of the residual curve is approximately 3% of the total area of the experimental data. While this model does a fairly good job of fitting the data, the differences are outside of the range of any dynamical effects or instrumental broadening that might explain small differences between the profiles. Also, these residuals are observed consistently in repetitions of this experiment and in diffraction data from other

cores. Though explanations for these residuals involving gap-filling carbon atoms between the graphene or some other small diffracting crystals may be within the realm of reason, other avenues of thought suggest graphene sheet shape is an important factor deserving consideration.

3.2.2. Triangular Flat Sheet Model Best Fit. Comparisons between Debye models from graphene sheets of different shapes have revealed that there are differences that manifest in diffraction. In attempting to model the experimental diffraction data from the graphene cores, graphene sheet shape effects must be considered. Triangular sheets are an example of an anisotropic sheet shape, or departure from the hexagonal, isotropic, model structure. Sheets of this shape might be expected if faceting around pentagonal defects were occurring, as the elements of a faceted nanocone are triangular sheets (Figure 2.11(a-b)). Measured along a side, molecular models of approximately 14[Å] and 44[Å] triangular sheets were constructed (similar to the molecule in Figure 2.1). Debye diffraction profiles were calculated for each of these, to be used as the endpoint patterns in the fitting routine. The triangular sheet best fit and experimental data are shown in Figure 3.4, along with the residuals between the two curves.

Visually, there is an obvious improvement in fitting the leading edges of both the (100) and (110) graphene peaks compared to the hexagonal sheet. This is also seen in the RMS difference being 332[intensity units], versus the 382[intensity units] from the hexagonal sheet best fit. This represents a 13% improvement in fit over the hexagonal sheet. The area under the residual curve now represents only 2.5% of the area under the

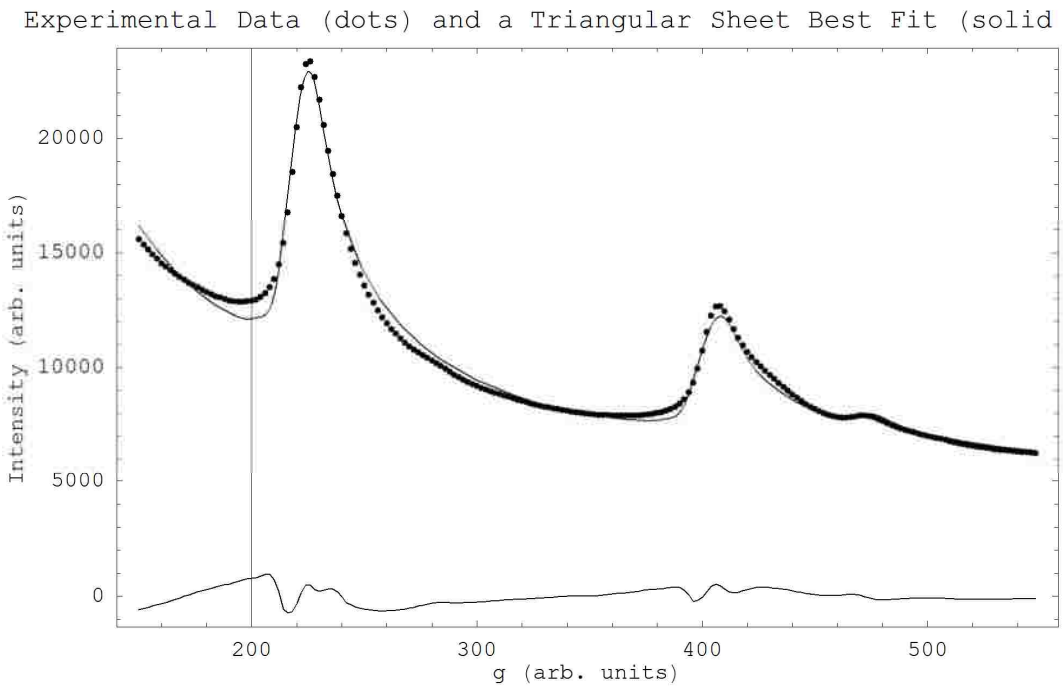

Figure 3.4: Experimental core diffraction data (dotted line) and a triangular sheet best fit (solid line). The fitting routine finds the best fit and molecule size by a least squares method. The lower curve represents the residuals between the two profiles.

experimental data. This analysis indicates that a significant improvement in fit can be realized by simply considering a different sheet shape. The repercussion of this is that the analysis suggests that if not triangular, some anisotropic sheet shape is better able to explain the experimental data. In other words, it should be interpreted that the graphene is likely in some shape that is different from the isotropic shape that might be expected for normal graphene sheet growth in free space.

3.2.3. Coherence Effects and Graphene Sheet Coordination. If the graphene sheets that make up the bulk of the core material are coordinated in some regular fashion, there could

be coherence between the lattice spacings from one sheet to the other that will manifest and alter the peak shapes. This is because under a given orientation of the crystal, some of the lattice fringes will be foreshortened in a particular way. This relationship between the structures can give rise to a sort of spatial "beat" frequency in reciprocal space. Coherence effects can arise due to faceting between graphene sheets, as an example of extreme curvature of graphene, where any one specific angle can be modeled to discern its effects on diffraction data. As seen in Chapter 2, satellite peaks result due to the orientation between adjoined sheets, and the location of these peaks will change as the angle between the sheets is changed. One can imagine that in experimental data, where somewhere on the order of 100,000 sheets are being sampled (given that the selected area aperture is 100[nm] in diameter and the specimen is 70[nm] thick), there is quite a range of angles between sheets in the ensemble. Thus, satellite peaks might not be expected to be visible, though the entire peak shape could be altered by the net effect of all the inter-sheet relationships.

In order to investigate whether coherence effects can play a role under these circumstances, and improve the fitting of the diffraction data, a molecular model for an atom-thick curved triangular sheet was constructed (Figure 2.21). This molecule is essentially a triangular-shaped conic section of a relaxed carbon nanocone and provides an example of a "bent" graphene sheet. Because the shape was only slightly altered from the flat triangular sheet, the size of the section was chosen to be the same as the flat triangular best fit size, as measured along the edge, or seam. The Debye profile for this curved triangle was calculated and background subtracted. It was then used in a least squares

fitting routine with the experimental diffraction data, where the background was part of the fitting process. The results are displayed in Figure 3.5.

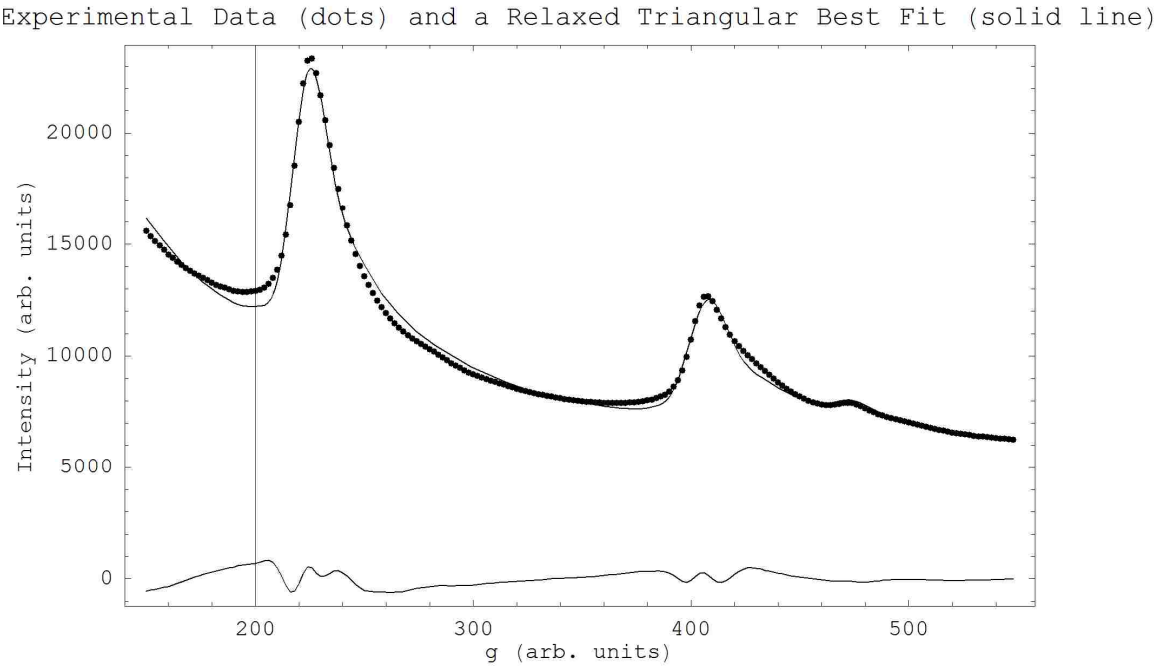

Figure 3.5: Experimental core diffraction data (dotted line) and a curved triangular sheet best fit (solid line). This is an improvement in fit over both the hexagonal sheet and the triangular sheet. The lower curve represents the residuals between the two profiles.

While this really only considers one specific atomic model with coherence effects, being that it does not take into account other angles between sheets, or faceting, an improvement in fit is measured using this molecule. The RMS difference between the two curves is 307[intensity units], an improvement of 7% over the triangular sheet model and 20% over the original hexagonal flat sheet model. The change in peak shape at the graphene periodicities and on the tailing edges allows for the gains observed here. This

analysis indicates that better fits are attainable when considering coherence effects, and that these effects do play a significant role in data from collections of atom-thick structures. A more sophisticated model of these effects might be able to explain away the majority of the remaining residuals.

3.3 SUMMARY

Using a spline-fitting routine, constructed to choose the most appropriate size of a given molecule and background, improvements in fit over the hexagonal sheet were observed consecutively using a triangular sheet, and then a curved triangular conic section. Ultimately, a 20% improvement in fit was realized. While these results do not necessarily suggest that the sheets must be triangular, it does point to the fact that sheet shape plays a major role in diffraction peak shape from an ensemble of graphene. Additionally, an anisotropic sheet shape is shown to significantly improve the fitting versus the isotropic model. This type of information must be considered in examining grain growth conditions in carbon producing stars.

Though only one model for coherence effects was considered in this work, it has been shown that their consideration can improve the fitting. Knowing that the changes in peak shape depend on the degree of curvature, or faceting, one can imagine that their might be some ideal, model combination of these that maximizes the fit improvement. Future work should consider other molecular models that would give rise to coherence effects and attempt to construct combinations of molecules for improved fitting of the experimental data. It should also be considered that average shape effects likely manifest in powder

diffraction data from collections of nanostructures. As computation methods advance in modeling diffraction profiles for various molecules, researchers should begin to discover this type of information within experimental diffraction data from nanocrystal ensembles, especially as the thickness of these crystals approaches the width of an atom.

4. HIGH-RESOLUTION TEM IMAGING OF NANOCRYSTALLINE GRAPHITIC STARDUST

Graphite spherules represent a subset of graphitic stardust with a very interesting core structure that has begun to be understood by using HRTEM imaging in conjunction with a variety of other characterization methods (Bernatowicz, et. al. 1996; Croat, et. al. 2005; Fraundorf & Wackenhut 2002; Fraundorf et al. 2000). Electron diffraction has revealed that the micron-sized cores of these grains (Figure 3.1) are composed of 2-4[nm] unlayered graphene sheets, where (002) graphitic layering has been suppressed (Bernatowicz, et. al. 1996; Croat, et. al. 2005). Previous HRTEM work on these cores has revealed linear features, likely associated with "edge-on", atom-thick structures, as expected from the diffraction data. These linear features often appear to be bent or adjoined, as if due to defects, randomly included in the graphene crystal lattice (Fraundorf & Wackenhut 2002).

With the aid of HRTEM image simulations, the linear features in the experimental images can be compared to various atomic models in order to shed some light on the size and shape of the graphene sheets within the cores. The projected thickness of linear features in HRTEM images of the core material can be gauged by comparing greyvalue intensities to those seen in image simulations of "edge-on" graphene (Chapter 2). Additionally, the amount of curvature, or relaxation, between adjoined linear features can be estimated by intensity profiling tangent to the point of intersection in HRTEM images. Simulations of relaxed and faceted nanocones provide two examples of curvature extremes for graphene with a single pentagonal defect; one where the nearby atoms are fully relaxed

around the defect, and another where they are strained, confined to the sheets in which they reside. The tangential profiles in simulations of these structures, viewed down orientations that lead to adjoined linear features, provide some constraints on measurements in experimental images.

Under certain orientations, graphene sheets will be viewed "edge-on". Greyvalue intensity profiles along the resulting linear features can reveal the shape of the graphene. In this work, graphene shape is investigated by profiling along linear features and comparing to simulated images of different graphene shapes (Chapter 2). Evidence is reported for both hexagonal and triangular graphene in HRTEM images, confirming electron diffraction evidence for non-hexagonal graphene (Chapter 3). Intensity profiles tangent to adjoined linear features show extreme curvature at these points, like that seen, for example, in a faceted pentagonal nanocone. The statistics of the angles between these linear features is also shown to be indicative of the type of curvature present, when compared to models of atom-thick structures with single defects (Chapter 2). Also, greyvalue intensities in linear features are shown to be within the realm of reason for the sheet size estimates from electron diffraction data by comparing them to simulations.

Lastly, High-Angle Annular Darkfield (HAADF) images taken with a 300kV aberration-corrected microscope at Oak Ridge National Lab are discussed. These observations revealed isolated heavy atoms within the core material. This is preliminary data that, in the long run, may help these particles tell the story of thermal transport during the course of their travels across the Milky Way galaxy, prior to their arrival on earth.

4.1 PHASE-CONTRAST HRTEM IMAGES OF GRAPHENE CORES

The specimens were prepared previously through a process of obtaining graphite separates from the meteoritic dust, embedding them in an epoxy, and ultramicrotoming 70[nm] thin sections. These sections were then floated onto 3[mm] holey carbon grids for TEM imaging (Bernatowicz, et. al. 1987, 1991, 1996; Amari, et. al. 1990, 1993; Hoppe, et. al. 1995). Specimen mounts were searched for graphite spherules that were torn and hanging over a hole in the holey carbon film, due to the need of very thin regions for high-resolution imaging. Phase-contrast HRTEM images were taken using a 300[kV] Philips EM430ST with point resolution near 0.2[nm]. Images recorded on film were then digitized at 2400[pixels/in] as 16-bit greyvalue data. This digitization included a hole in the specimen and the image tag, resulting in a 16-bit greyvalue range corresponding to the incident electron beam intensity and no intensity respectively. The digitization process results in a linear correlation between greyvalue intensity and time of exposure, whereas the film response is typically logarithmic (Hunton, 2004).

Figure 4.1 shows an example of an HRTEM image of the core material in a thin region. The adjoined linear features are visible in the thin region, as previously reported (Fraundorf & Wackenhut 2002). The power spectrum from this thin core region does not exhibit any (002) graphitic layering (noise within 1% of the background intensity) and shows a portion of the (100) ring, i.e. evidence in the image of unlayered graphene.

While electron diffraction data suggests that the size of the graphene sheets making up this core should be on the order of 4[nm], the linear features in this image appear

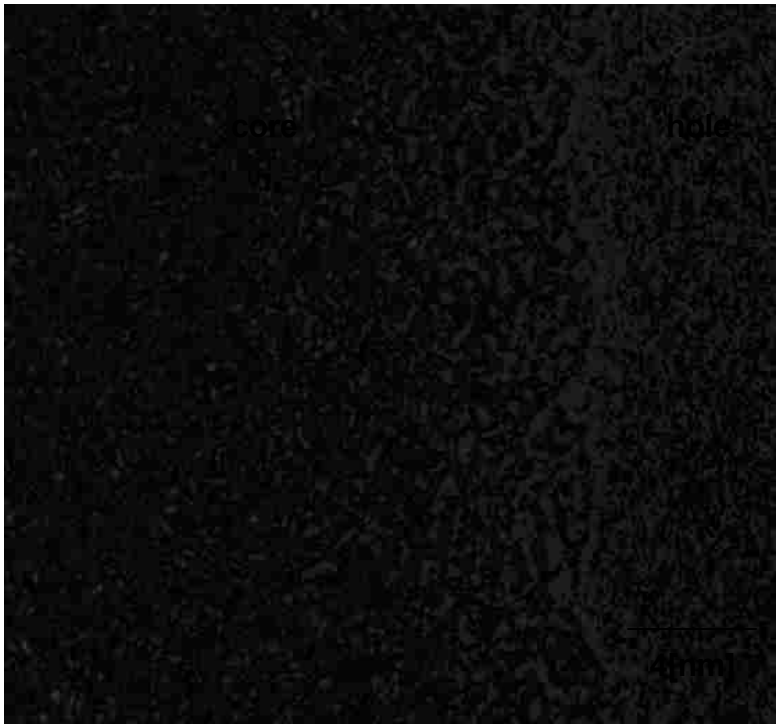

Figure 4.1: An HRTEM image of the core material from a torn graphite spherule. The hole, seen on the far right of the image is useful for interpreting greyvalues in terms of mass-thickness by comparing to simulations.

shorter. As discussed in the previous chapter, sheet shape effects might explain some of these differences in diffraction. Similarly, the projected length of an edge-on triangular sheet might appear shorter than a hexagonal sheet of comparable coherence width in an otherwise noisy field. The adjoined linear features suggest that there are structures near the sheet size suggested by diffraction, but that are composed of graphene sheets joined along a seam. This type of data can be compared to expectations from simulations, as can the intensity profiles and angles between the adjoined linear features (Chapter 2). These comparisons characterize the core material in a way not done previously, and further constrain our interpretation of other characterization data (Chapters 3 and 5).

4.1.1. Graphene Sheet Thickness. The core material was characterized using greyvalue intensity profiles that include regions with no specimen at all, which provide information on the incident beam. Greyvalues can thus be scaled to the unscattered intensity in the hole. Figure 4.2 shows part of the image in Figure 4.1. The inset averages greyvalue intensity over vertical columns in the boxed portion of the image. The average greyvalue in the hole is approximately 60,000 out of a possible 65,535 (16-bit greyvalue data), with the average intensity in the core region getting progressively thicker away from the hole. The far left side of the image has an average greyvalue near 57,000. By finding a linear best fit to the core region data (Figure 4.3), it is possible to develop a function that describes the average greyvalue at a certain distance from the hole. This can be used to gauge intensities seen in line scans through linear features, and determine how well these features stand out against the surrounding medium. The least squares fit with x measured in number of pixels from the left side in Figure 4.2 is,

$$GV = 3.3458(x) + 57376\,. \tag{5}$$

To put this function to use, line scans were performed that crossed the adjoined point between two linear features in the image. An example of this measurement is shown in Figure 4.4. Likely, this point of intersection corresponds to some regularly occurring feature between graphene sheets (defects in the 2D lattice), viewed down a preferential orientation. This provides a gauge of the average thickness of the sheets. If these features are arising from faceting between sheets, these points of intersection would represent seams between the sheets and should be relatable to the maximum sheet thickness.

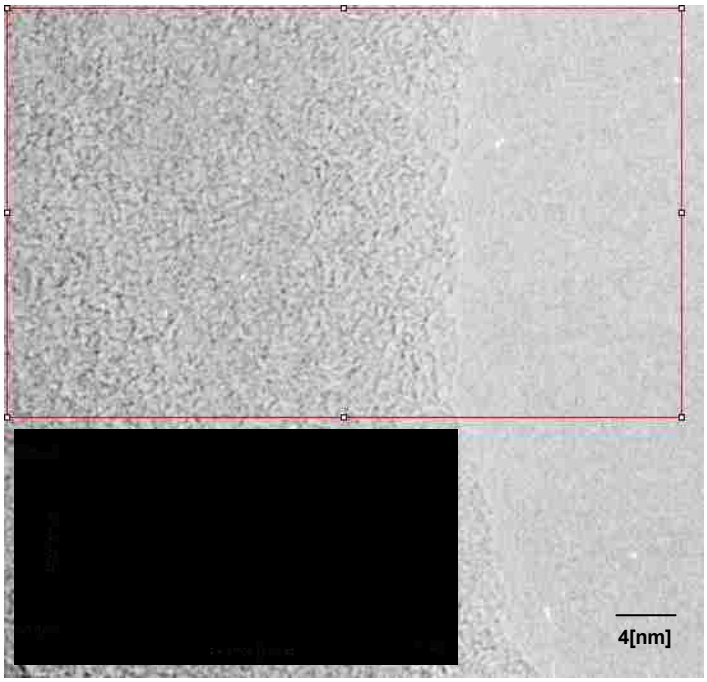

Figure 4.2: An HRTEM image of core material and the average greyvalue intensity profile, plotted horizontally over the windowed region. The profile in the inset illustrates how the core gets progressively thicker away from the hole in the image.

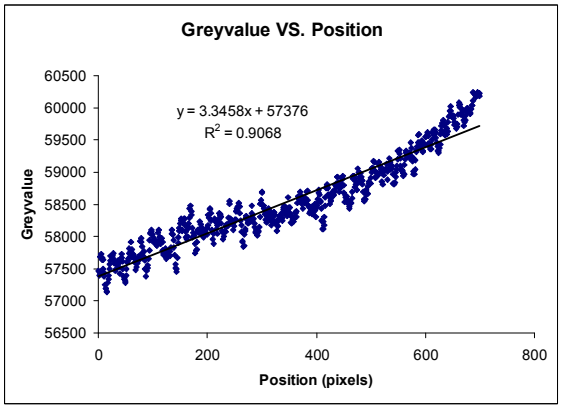

Figure 4.3: The portion of the profile in Figure 4.2 corresponding to the core material and a best fit trend line. The function of this line can be used to take the thickness of the surrounding medium into account when measuring the greyvalue intensities of linear features.

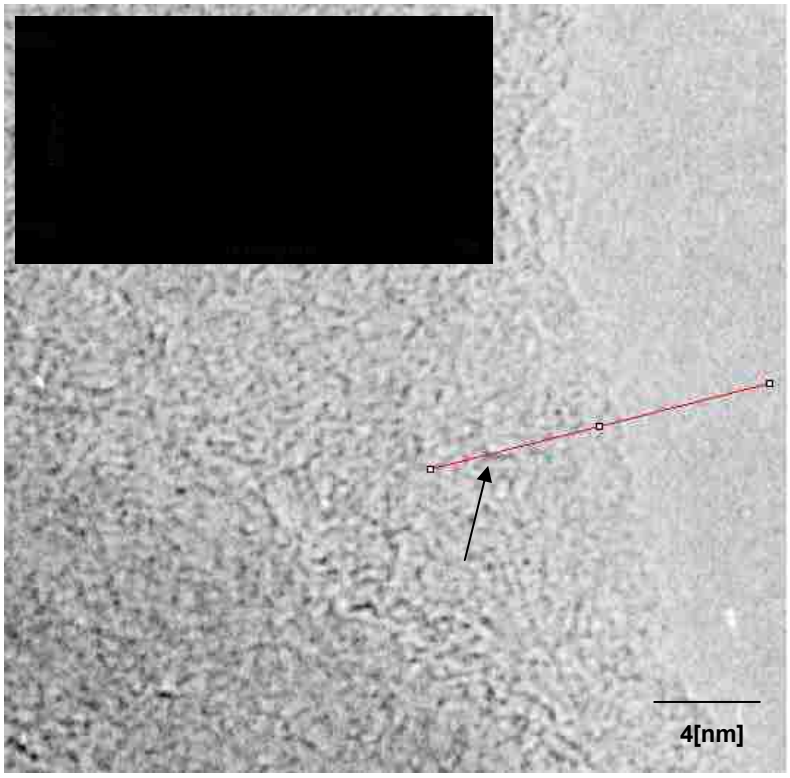

Figure 4.4: A greyvalue intensity line scan through adjoined linear features in an HRTEM image of the core material. The trough is approximately 100 pixels in horizontal distance from the hole, which corresponds to a background greyvalue of ~600 below the hole intensity, using Equation 5. This results in the greyvalue attributable to the feature being ~5200 below the hole intensity.

Because the adjoined feature is approximately 100 pixels in horizontal distance from the hole, Equation 5 indicates the background greyvalue is approximately 600 below the hole intensity at that point. Taking this into account when comparing the trough intensity to the hole intensity, the greyvalue attributable to the adjoined feature is ~5200 below the hole intensity. This difference represents about 9% of the hole intensity (~60,000). Simulations of edge-on graphene 20[Å] in breadth, embedded in a 40[Å] thick amorphous layer, have shown (Chapter 2) that greyvalue intensity fluctuations of anywhere between 7-

17% of the hole intensity are expected when the background greyvalue is taken into account. Thus, greyvalue intensities in this thin region seem to be indicative of structures that in projection are less than the sheet size suggested by diffraction. Note that this is not the average greyvalue for this entire thin region, but the value across the adjoined linear features. The space between the linear features is much more optically thin than the sheets themselves, or less dense in projection. Therefore it seems likely that these linear features do correspond to single "edge-on" graphene sheets. (Note: This interpretation is bolstered by the fact that the linear features here "take the place" of parallel lines, with the graphite (002) spacing, when one looks at terrestrial disordered graphite in the same way.)

4.1.2. Curvature Profiles of Adjoined Linear Features. Intensity profiles tangent to adjoined linear features can reveal the degree of relaxation between the two graphene sheets. Simulations of faceted and fully relaxed nanocones, viewed down orientations that give rise to linear features, provide a backdrop for various expectations depending on the abruptness of the joining of the linear features (Chapter 2). The faceted case represents a case of extreme curvature, where little bending has occurred around the joining seam, while the fully relaxed case will have a more gradual bend around the projected seam direction (Figure 2.11). The difference between these two cases is seen in profiles through the intersecting point and tangent to the features. This trough will be severely broadened if there are nearby atoms that have relaxed around the seam direction, whereas the trough will appear sharper if the sheets are more faceted and branch off abruptly (see Figures 2.14-2.17).

Figure 4.5 shows a portion of the image in Figure 4.1, and a line scan through another set of adjoined linear features (similar to Figure 4.4). The shape of the troughs seen in Figures 4.4 and 4.5, when compared to the simulations of the faceted and relaxed nanocones, reveals a degree of curvature more inline with that seen in the case of faceting. The troughs here spread over roughly 12-15[pixels] at their base, which corresponds to about 6[Å] in the image. Troughs seen in the simulations of faceted nanocones span roughly 13[pixels], corresponding to a distance of about 6.5[Å] (Figure 4.5). The profile in

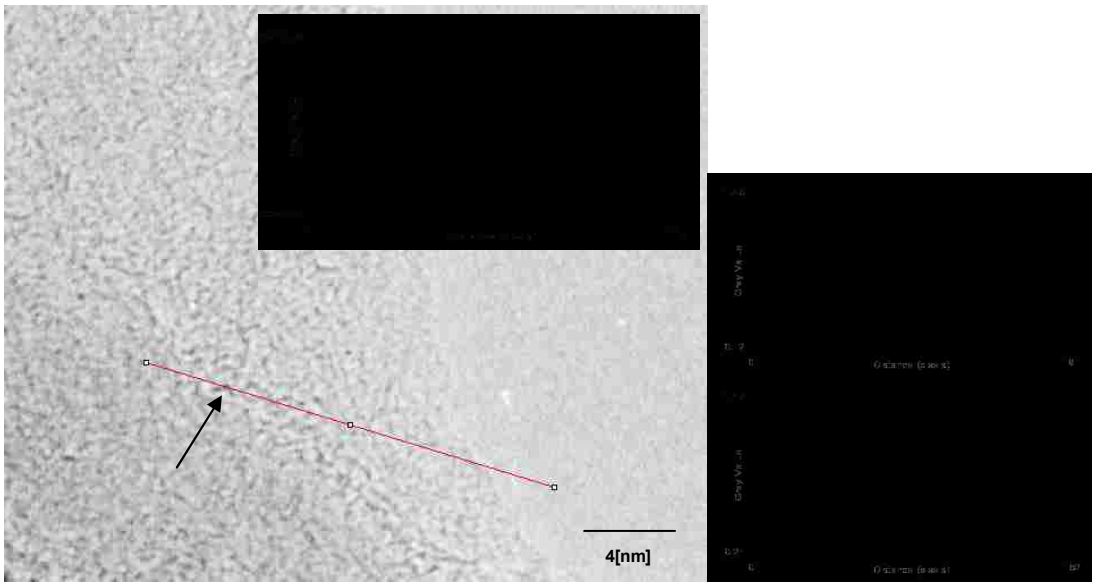

Figure 4.5: A line scan intensity profile through the point of intersection of two adjoined linear features, similar to that seen in Figure 4.4. The trough corresponding to this point is similar in width to that seen in Figure 4.4, and each matches well with line scans from image simulations of faceted nanocones viewed down a seam. The two side profile plots are from tangential profiles of a faceted and relaxed nanocone in simulated phase contrast TEM images near the same point resolution.

the relaxed nanocone simulated images is much broader, spanning roughly 26[pixels] (Figure 4.5). Thus, the intersections between the linear features in the core material tend to be abrupt, more inline with faceting. While some of these apparent intersections could be due to two sheets at different heights in the specimen being projected to appear near one another, the intensity data discussed in the previous section puts some limits on that scenario. The material is just not thick enough in this region for that to always be the case. More likely is that the coordination between sheets is being observed in these abrupt junctions.

4.1.3. Graphene Sheet Shapes in Presolar Cores. Image simulations of triangular and hexagonal-shaped graphene have suggested that greyvalue intensity line scans along linear features corresponding to edge-on sheets might be able to delineate between different sheet shapes (Chapter 2). Figures 2.2 through 2.10 give some expectations for what might be seen in line scans along "edge-on" sheets. The simulations for the 2[Å] point resolution scope indicated that there are fewer troughs visible than in the case of the 1[Å] resolution scope, though they extend over a similar distance, corresponding to the size of the sheet. These troughs appear to be about 10-15 pixels apart in simulations or between 4.5[Å] to 6[Å] apart. Given that the experimental scope in this instance has a similar point resolution, this characteristic, as well as the intensity fluctuations corresponding to sheet shape, should be present for sheets that are viewed nearly edge-on.

Figures 4.6 and 4.7 illustrate some examples of twenty different greyvalue intensity lines scans along linear features in core images. The line scans in both figures have troughs

that are approximately 10-15 pixels apart, or roughly 4.5-6[Å]. It is unclear what mechanism gives rise to this spacing between troughs, but it is consistent with the image simulations of edge-on graphene. The sheet shape is also evident in that the troughs gradually return to the background greyvalue, more indicative of a triangular shape. In Figure 4.7(b), the difference in greyvalue between each of the three troughs making up the sheet is ~600. Relative to the intensity in the hole, this greyvalue change is only ~2%,

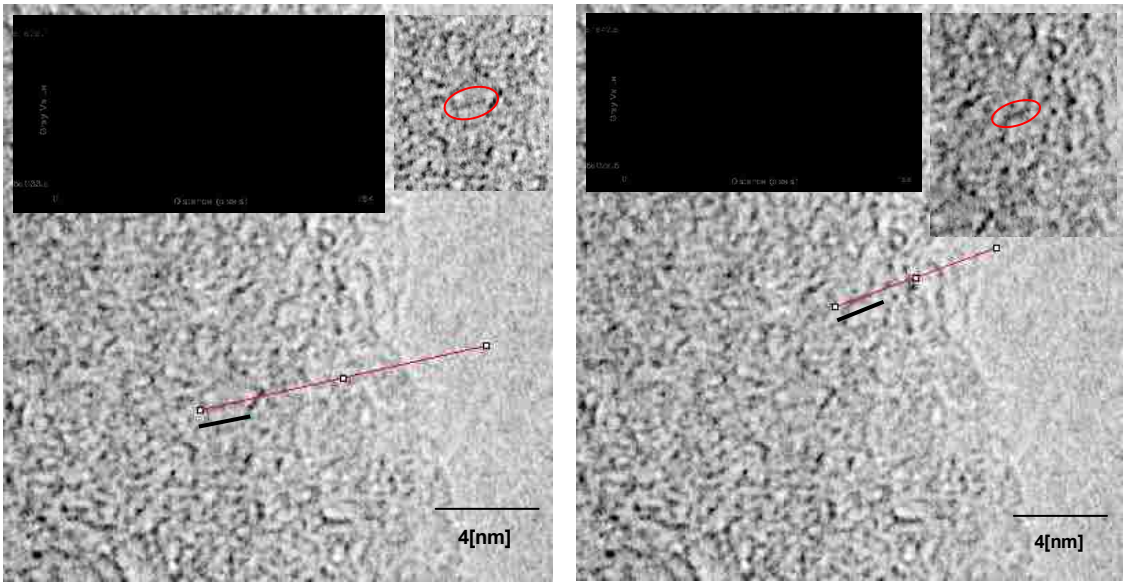

(a) **(b)**

Figure 4.6: HRTEM images of the core material and greyvalue intensity line scans through linear features in the images. The patterns of troughs are similar to those seen in TEM image simulations of "edge-on" graphene. The changes in intensity from trough to trough, and the gradual return to the background greyvalue, are indicative of the sheet shape, (a) triangular, (b) and hexagonal.

which is fairly consistent with changes seen in simulations (Section 2.2.1). The similarities to the sheet shape profiles seen in simulations lead to the conclusion that the majority of the profiled sheets are non-hexagonal, as suggested by diffraction (Chapter 3).

It is also worth noting that the greyvalue intensity of the troughs is about 6000 below that of the nearby hole in the images, and about 5000 below the background greyvalue of the surrounding material in each case. Similar to the discussion in Section 4.1.1, these

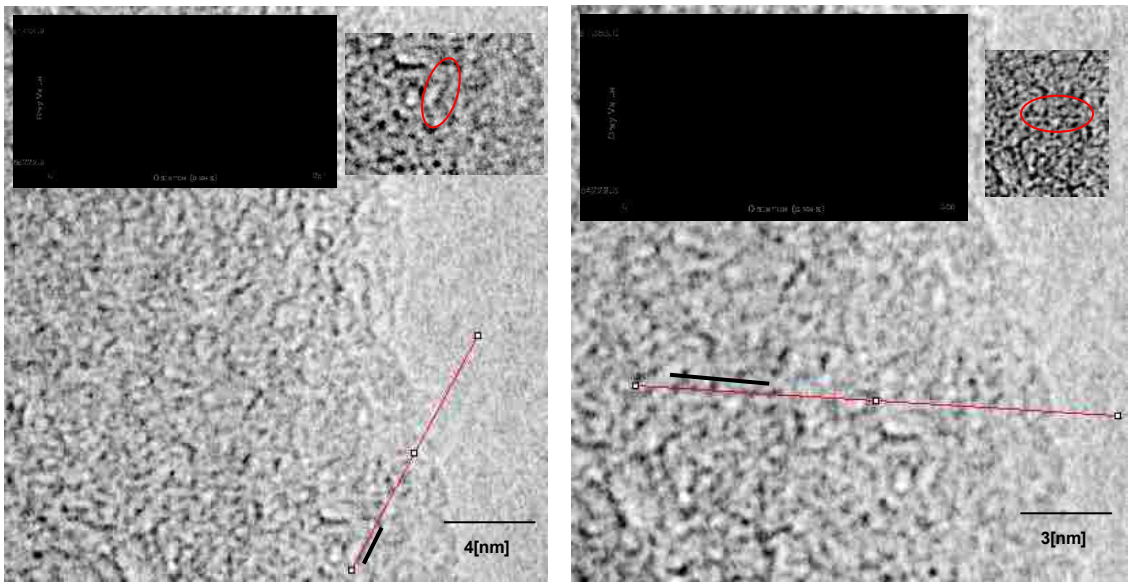

(a) **(b)**

Figure 4.7: Additional greyvalue intensity line scans along linear features in the images. The profiles are again consistent with simulations of triangular-shaped graphene molecules, where the greyvalue intensities gradually fall-off in the line scan along the sheet, eventually melding into the background. Nearly 90% of profiles measured exhibited the triangular shape.

values are about 9% of the intensity in the hole. This matches well with simulations of 20[Å] graphene sheets in thicker amorphous layers, indicating the graphene measured here is at least that thick.

4.1.4. Statistics of Linear Feature Angles. Just as greyvalue intensity profiles can provide information on curvature, or faceting, of graphene sheets in the core material, the statistics of angles between linear features observed in HRTEM images can also constrain the likelihood of these two extremes of curvature. As discussed in Section 2.2.2, there are certain orientations with respect to the electron beam that either fully relaxed or faceted nanocones will exhibit a strong projected potential, likely resulting in linear image features that would stand out against the surrounding matrix. In order to take advantage of those

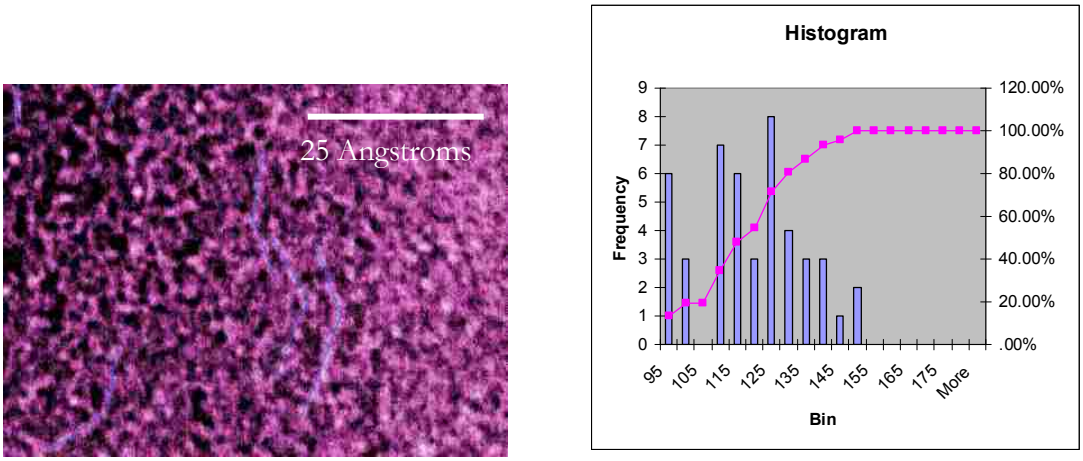

Figure 4.8: A reversed contrast HRTEM image of the core, where some of the features identified as being adjoined and linear are highlighted. The histogram of observed angles indicates a strong incidence of angles less than 145˚. This is not well-supported by a model of fully relaxed nanocones.

models and the statistics on angles between linear features observed in simulated images of each structure, angles between adjoined linear features were measured in the experimental image, and the resulting histogram was plotted (Figure 4.8).

The image in Figure 4.8 has undergone a contrast reversal, in order to emphasize the linear features in the image data. The outlined regions indicate some of the sheets thought to be adjoined and considered in this measurement. The identification and subsequent measurement of angles was performed similarly to that done for the simulated images. The resulting histogram in Figure 4.8 indicates a strong incidence of low angle measurements. The statistics seen in image simulations of fully relaxed nanocones would be difficult to cite in explaining angles below 145˚, while the faceted nanocone statistics allow for a higher incidence of smaller angles. This analysis helps rule out any strong presence of fully relaxed nanocones in the core material, or at least suggests that carbon atoms have not had the ability to fully relax around defects in the graphene lattice. This result, combined with the tangential intensity profile results suggests much of the carbon is faceted around lattice defects.

4.2 HIGH-ANGLE ANNULAR DARKFIELD IMAGES OF CORE MATERIAL

Further imaging of the core material was done using a VG HB603U scanning transmission electron microscope (STEM) with a Nion aberration corrector at Oak Ridge National Laboratory. The 300keV scope is able to attain a probe size of 0.6[Å]. High-Angle Annular Darkfield (HAADF) images were taken, where the contrast mechanism is largely due to projected “Z” (atomic number) thickness. While these images are still being

analyzed for evidence of edge-on graphene, the observation of both isolated and small clusters of heavy atoms (Z>>6) is reported here. Figure 4.9 is an HAADF image of the core material, with an inset showing a portion of the image containing an isolated heavy atom. This feature is approximately 1[Å] in breadth in the image, using the half width at half maximum of the object's profile (5[pixels]). This feature is significantly brighter than the surrounding medium, indicative of its high Z-value.

The existence of isolated heavy atoms and clusters of heavy atoms is another structural characteristic of the cores. Work is currently underway to identify these atoms

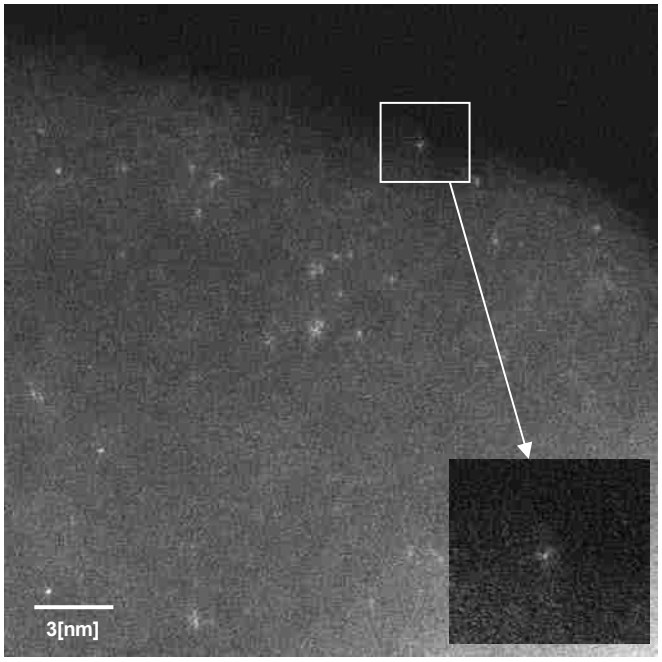

Figure 4.9: An HAADF image of the core material offering evidence for the existence of isolated heavy atoms, along with small cluster of heavy atoms, dispersed throughout the carbon matrix.

using the greyvalue as a measure of scattering strength of the nucleus, and comparing this to the average greyvalue of the surrounding carbon. The incomplete clustering of individual heavy atoms indicates that transport by thermal diffusion has been limited by the time of condensation. This puts limits on the thermal history of these grains during the multi-billion year period of their travels from formation until their arrival on earth, as well as on the thermal diffusion coefficients in these unlayered graphene cores. In-situ annealing experiments at atomic resolution in these specimens might help quantify those limits.

4.3 SUMMARY

HAADF and phase contrast HRTEM imaging of the core material found in a subset of graphitic stardust has revealed a wealth of structural information. Isolated heavy atoms have been observed in Z-contrast image data, indicating they have been frozen into place. Meanwhile, statistical measures of angles between linear features in phase contrast images suggests that carbon atoms have not been able to fully relax around regions between adjoined sheets.

The greyvalue intensity profile data, in combination with image simulations of graphene, is able to shed further light on the shape and size of the graphene making up the core material. Profiles along linear features in images converge with expectations from simulated images of graphene sheets. The fluctuations in greyvalue above the noise level along these linear features are similar to the shape effects seen in simulations of triangular and hexagonal sheets. Though the greyvalue intensities seem to suggest the graphene in

the core is closer to 20[Å] than 40[Å], it should be considered that the shape and size of the average diffracting 2D crystal in the cores could be that for two sheets sharing a row of atoms along a seam rather than a single sheet. The adjoined structures observed in HRTEM images reinforce the idea that these shape effects play a significant role in diffraction from the core, accounting for some of the deviations from a flat sheet model seen in those analyses (Chapter 3). The intensity profile evidence for triangular sheets also speaks to the improvement in diffraction modeling observed when using triangular versus hexagonal sheets.

Future work on imaging the structure of these grains might involve experiments such as oxygen ashing of the graphite spherules prior to imaging. This would remove "loose" carbons that are not fixed in in-plane graphene bonds, leaving behind a skeleton structure made up of surviving carbon. Under these circumstances, graphene sheets should be more clearly visible with more of the surrounding matrix stripped away.

5. DENSITY MEASUREMENTS OF NANOCRYSTALLINE GRAPHITIC STARDUST

Formed in the atmospheres of red giants (AGB stars) after first dredge-up, graphite spherules present both the astrophysicist and materials scientist with an intriguing puzzle (Bernatowicz, et. al. 1987, 1991, 1996; Amari, et. al. 1990, 1993; Hoppe, et. al. 1995). Research on the micron-sized cores of these grains has revealed a nanocrystalline carbon material with no laboratory analog. Electron diffraction data shows that these cores are composed of unlayered graphene (Bernatowicz, et. al. 1996). This is supported by the observation of "edge-on" graphene sheets in HRTEM imaging (Fraundorf & Wackenhut 2002). Recently, diffraction and image modeling have suggested that the majority of the graphene sheets in the core material are triangular or non-hexagonal (Chapters 3 and 4).

Here, the density of the core material is examined by comparing electron mean-free-path thickness measurements between the nanocrystalline cores and the graphitic rims that surround them. The concentric graphitic rims are similar to the concentric graphite layers in a carbon onion (Ugarte 1992). Assuming the rims have a density similar to that of graphite (~2.2[g/cm^3]), and that the specimen preparation methods allow for a grain that is roughly the same physical thickness across its breadth, electron mean-free-path differences between the rim and the core will be indicative of the density differences. These differences can be measured by comparing integrated EELS (Electron Energy Loss Spectroscopy) intensities from the rim and the core (Egerton 1996). Additionally, Energy-Filtered TEM (EFTEM) imaging can be used to perform this same calculation pixel by

pixel, resulting in an electron mean-free-path thickness image. Since both the rim and core are predominantly carbon, greyvalues in this resulting image are indicative of fluctuations in density, assuming the grains have nearly the same physical thickness from point to point.

The results of these two examinations suggest that the core is less dense than the rim (i.e. between 1.5 and 2 [g/cm^3]). This value is a bit smaller than that previously reported for the core material, where the density was gauged by the position of the peaks in EELS data corresponding to plasmon losses (Bernatowicz, et. al. 1996). The past conclusion relied on inferences made for a binary mixture of materials, where the position of the plasmon peak is indicative of the concentration of the two constituents. The work here found a position for the plasmon peak like that in the previous study. However, it is not clear that a precise density value can be inferred from its analysis since crystallite size and increased electron density are known to affect plasmon peak position (Dhara, et. al. 2003, 2004; Liu, et. al. 1998). Graphene has also been shown to exhibit variations in electron density near defects in the graphene lattice, which could affect plasmon peak position (Berber, et. al. 2000; Novoselov, et. al. 2005; Peres, et. al. 2005). In contrast, the mean-free-path thickness differences observed in this study are robust and difficult to explain as being due to any mechanism other than density differences between the core and rim.

5.1 EELS SPECTRA AND RELATIVE MEAN-FREE-PATH THICKNESS

Electron Energy-Loss data was taken using a Gatan 607 series spectrometer in a Phillips EM430ST Transmission Electron Microscope. A selected area aperture was used to isolate a quarter-micron region of interest in each data set, and a large objective aperture

(angular acceptance around 13 milliradians) was used to include diffracted electrons out to 1/1.5A as well. For TEM specimen preparation, the onions were embedded in an epoxy, which was ultramicrotomed in approximately 70[nm] thick sections. These sections were then floated onto a holey carbon film of a 3[mm] copper grid. One of the assumptions in this work is that grains that are not torn are roughly the same physical thickness in the direction of the electron beam. While this is a critical assumption for drawing conclusions about the comparison of EELS data from different points on the specimen, it is noted here that EFTEM imaging (discussed in the next section) is sensitive to these physical changes and can actually map out these fluctuations across imaged grains.

Figure 5.1 illustrates a typical EELS spectrum from core material, and a Gaussian curve, fit to the zero-loss peak in the data. The integrated intensities of each of these curves can be used to gauge the mean-free-path thickness. This can be seen by examining the formula

$$I = I_0 e^{-\frac{t}{\lambda}}. \tag{5}$$

Here, the integrated intensity, I, of the EELS pattern is equal to the integrated intensity of the zero-loss peak, I_0, multiplied by the exponential function shown, where t is the physical thickness of the specimen and λ is the inelastic mean-free-path for the specimen (Egerton, 1996, Malis, et. al. 1988). For each set of data, such as that shown in Figure 5.1, the relative thickness is calculated as,

$$\frac{t}{\lambda} = \ln\left[\frac{I}{I_0}\right]. \tag{6}$$

The ratio of the relative thickness in the core and rim results in a comparison of "apparent thickness", or in this case density. That is to say, if the inelastic mean-free-path of carbon is assumed to be the same in each case, and the physical thickness of the core is similar to that of the rim (within a few nanometers), the differences in relative thickness, are due to the presence of more atoms per square centimeter in projection.

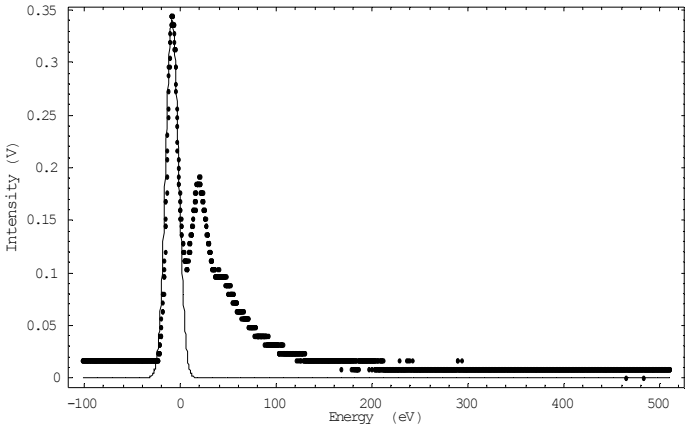

Figure 5.1: An EELS spectra (dashed line) from the core material and a Gaussian curve (solid line) fit to the zero-loss peak. The integrated intensity of these two curves can be compared to determine a mean-free-path thickness.

EELS data was taken from the selected areas marked (A, B, C, and D) in Figure 5.2. This process was repeated with four other grains. For comparison to the core spectra shown in Figure 5.1, Figure 5.3 shows a rim spectrum with a fitted zero-loss peak. The relative thickness is calculated in each of these cases using Equation 6, and the results are divided, giving a number that represents the density of the core relative to the rim. The average value for this measure in these experiments is 0.68. Once again, assuming the rims

to have a density comparable to that of graphite (~ 2.2 [g/cm^3]), this suggests the cores have a density nearer to that of 1.5 [g/cm^3].

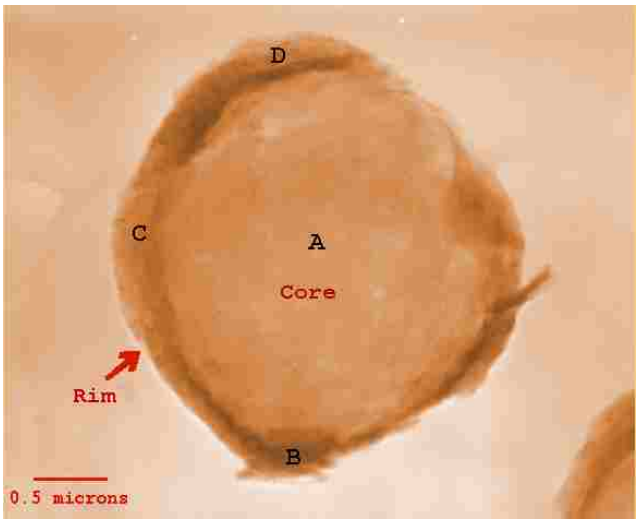

Figure 5.2: A graphite spherule, exhibiting the core-rim structure indicative of these grains. The letters correspond to regions where EELS data was taken. This process was repeated with four other grains.

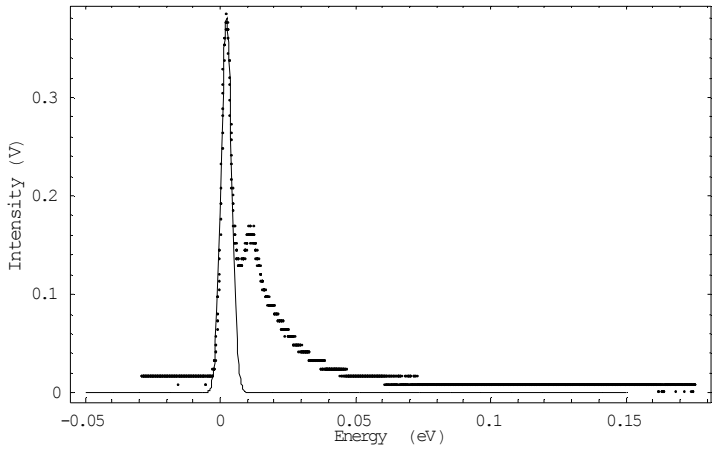

Figure 5.3: An EELS spectra (dashed line) from the rim and a Gaussian curve (solid line) fit to the zero-loss peak.

5.2 EFTEM IMAGING OF GRAPHITE SPHERULES AND MEAN-FREE-PATH THICKNESS MAPS

Transmission electron microscopes with energy-filtering capabilities are able to perform the same measurement discussed in the previous section for the entire field of view. This is accomplished by taking two images; 1) a normal brightfield TEM image, and 2) an image formed using only zero-loss electrons. By taking the natural log of the ratio of the two images pixel by pixel, the resulting image has greyvalue intensities that represent the relative mean-free-path-thickness (Egerton and Leapman, 1995).

$$I_{MFPthickness} = \ln\left[\frac{I_{brightfield}}{I_{elastic}}\right] \tag{7}$$

Upon calculation of this image, intensity profiling can be used to find average intensities in the rim and the core. One can then find the ratio of these for density comparisons, as was done with the EELS measurements. It is also possible to create a three dimensional plot of these intensities, in order to spot trends and perhaps grain damage incurred during specimen preparation.

All energy-filtered image data was collected using a Leo 912 EFTEM with an Omega filter. The objective aperture was approximately 13[mrad] for EFTEM imaging, and was used with an energy selecting aperture of 15[eV] resolution, typical for operation in ESI (Electron Spectroscopic Imaging) mode.

5.2.1. Intensity Profiles in Mean-Free-Path Thickness Images. With a brightfield image and an image formed using only zero-loss electrons, the image seen in Figure 5.4 was calculated per Equation 7. The shadowed side of the spherule in the lower right corner indicates that there was some drift between the two images, which could be corrected for. In this case, because of the large size of the grain and the ability to consider the greyvalue at all points on the spherule as a separate measurement, this drift is not so significant as to severely distort the average data.

The windowed region in Figure 5.4 indicates the region over which the intensity profile is calculated. The greyvalues are averaged in the horizontal direction and plotted along the vertical direction of the window. This results in the profile seen in Figure 5.5, where the areas of both the rim and core are clearly observed. The profile also includes a portion of the hole. The hole intensity is used to establish the intensity corresponding to no energy-loss, or no matter density. Subtracting the hole intensity from the intensity in the rim and core and taking the ratio, as before, again results in the core being less dense than the rim (0.64, or a core density of ~1.5 [g/cm^3], assuming 2.2 [g/cm^3] in the rims). These measurements, as well as the EELS measurements, are slightly altered by the presence of the holey carbon film. However, these differences should average out across the specimen, in the intensity profile, being that little variation is seen in the carbon film in the mean-free-path thickness map. Differences that might arise due to Bragg scattering in the (002) graphitic rims of the spherules should be small. This assertion is based on results using multiwalled nanotubes and comparing the projected mass thickness to the profile in a relative mean-free-path thickness image (Appendix A).

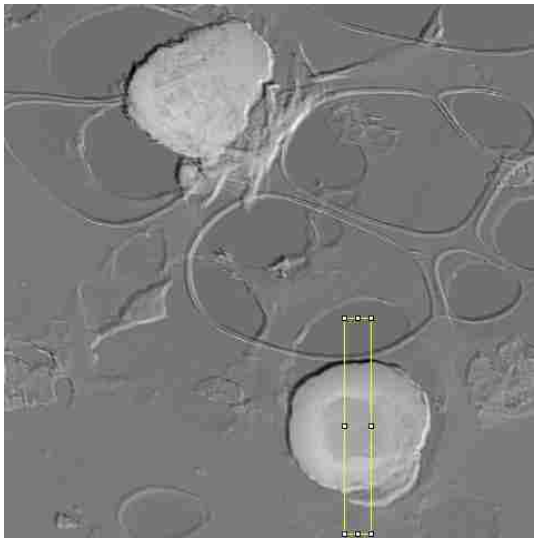

Figure 5.4: A calculated mean-free-path thickness image of a graphite spherule with a nanocrystalline core (field of view ~4[microns]). Variations in intensity are indicative of mean-free-path differences. The windowed region corresponds to the profile shown in Figure 5.5.

Figure 5.5: The greyvalue intensity profile corresponding to the windowed region in Figure 5.4. The greyvalues are averaged across the window horizontally and plotted along the vertical direction. The hole in the image and the regions corresponding to the core material and the rim are all clearly visible.

5.2.2. Three Dimensional Plotting of Relative Mean-Free-Path Thickness Maps. In an attempt to take advantage of all of the data in the relative mean-free-path thickness images, three dimensional plotting of the greyvalue intensities was performed (Figure 5.6). Here, the core material is shown in green and the rim in purple. A gap is exists between part of the core and rim where the data was not clearly from one region or the other. This data can be used to visualize the changes in mean-free-path across the specimen and be used to observe trends that likely reflect on specimen preparation processes. Images were loaded into Mathematica, where regions of the core and rim were selected for plane-fitting. A plane-fit was attempted with the core data in an effort to gauge the evenness of the grain. The core intensities are plotted in Figure 5.7, and the best fit plane, arrived at through a least squares minimization, is shown as well. The equation of the plane is $\mathbf{z} = -(5.4\text{x}10^{-5})\mathbf{x} - (4.4\text{x}10^{-4})\mathbf{y} + 1.26$. Notice that while the plane appears to be slanted severely, the range of intensity values across the plane is between 1.25 and 1.05. Thus, fluctuations in the core intensities are under 16%. While the specimen cutting process was likely not perfect, this does put some bounds on the range of mean-free-path differences in the core. An upper bound on the uncertainty in the density measurement might be ± 0.3 [g/cm^3] (16% variability).

The rim was also plotted and a best fit plane was found, as shown in Figure 5.8. Observe here that the range in intensity values in the plane-fit is larger than in the core, indicating that there might be more of a slope to the cut. Here the intensities range from 1.6 all the way down to 1, corresponding to a variability of 38%. The equation for the plane in Figure 5.8 is $\mathbf{z} = -(2.7\text{x}10^{-3})\mathbf{x} - (8.7\text{x}10^{-4})\mathbf{y} + 1.755$. The plane-fit equations for

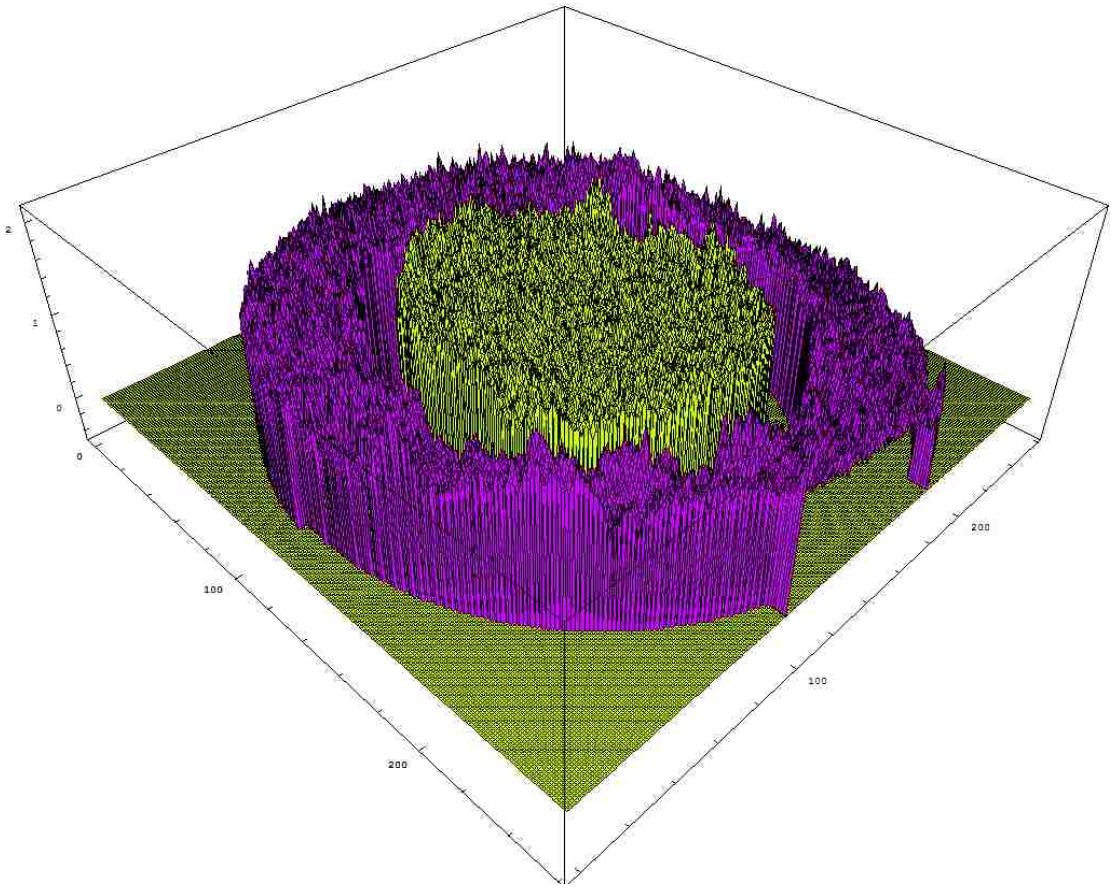

Figure 5.6: A three dimensional plot of the intensities of the graphite spherule that was profiled in Figure 5.4. By attempting to fit a plane to the core (green) and rim (purple), it is possible to gauge how evenly the grain was cut during specimen preparation.

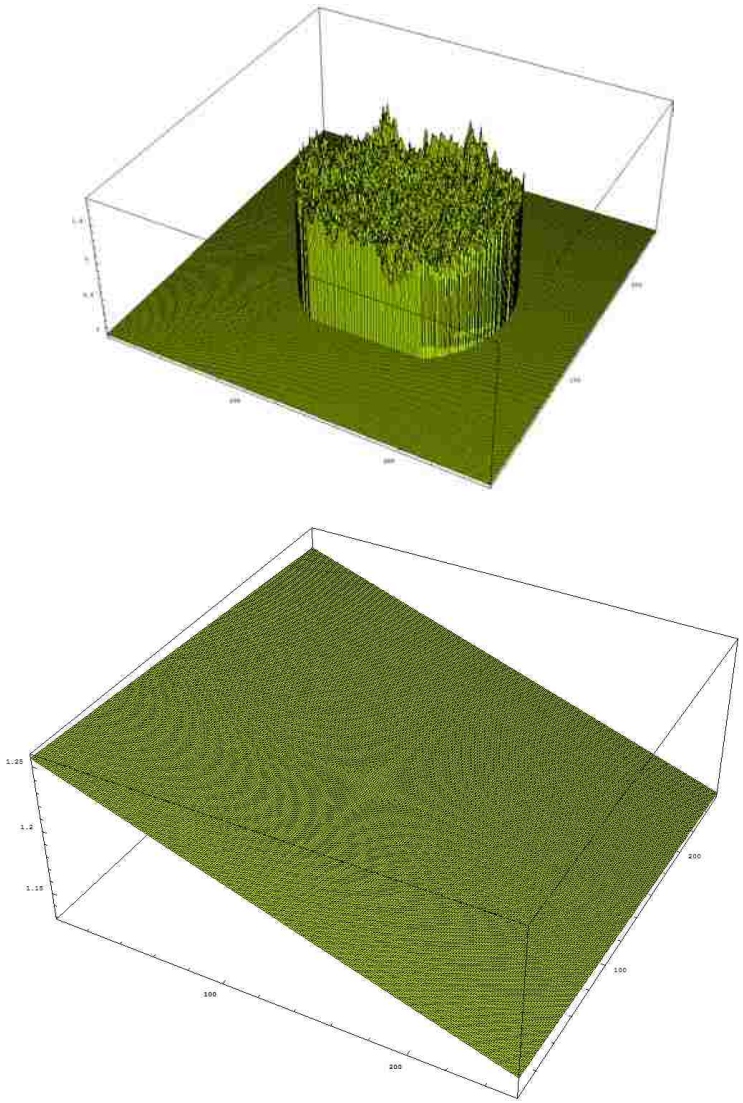

Figure 5.7: A three-dimensional plot of the greyvalue data from the core of the spherule from Figure 5.4 and the resulting plane-fit to the data. Notice that while the plane appears slanted, the intensities range between 1.25 and 1.05. Thus, the value in the core is fairly constant.

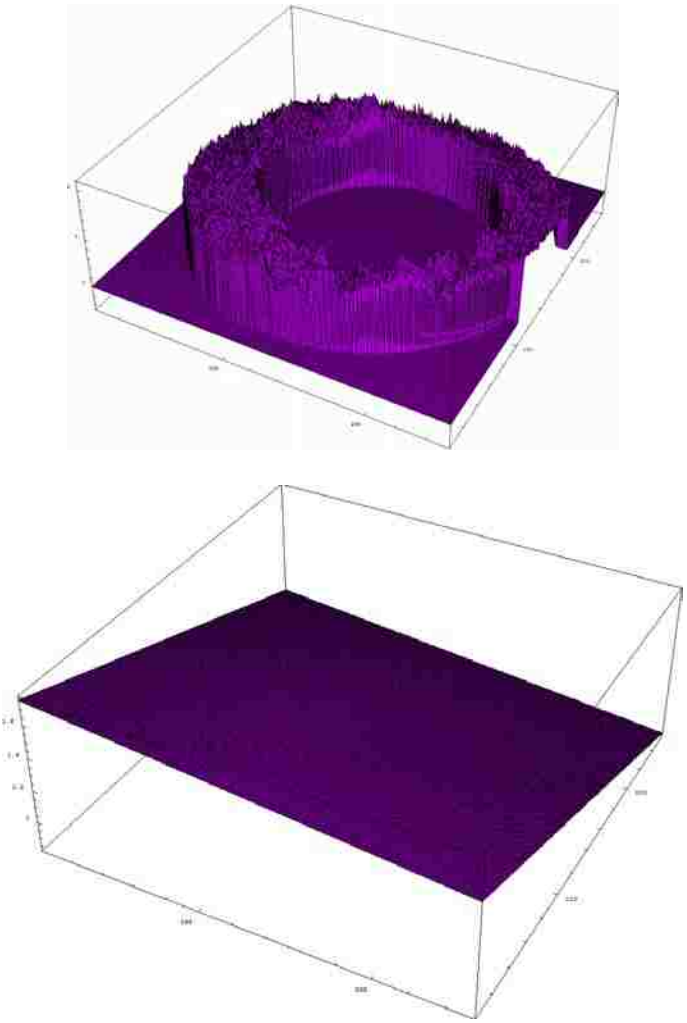

Figure 5.8: A three-dimensional plot of the greyvalue data from a section of the rim and the resulting plane-fit data. Observe the larger degree of tilt relative to the z-direction due to the apparent uneven thickness of the rim.

the core and the rim were each plotted over appropriate regions in Figure 5.9, in order to get a sense of the relative slope between the core and rim. The angle between the planes is ~3˚, and it is noted that they are sloped in a similar direction (to the right). This is further indication that this shape is a result of the specimen preparation process, where the rim

might be susceptible to tearing due to the more organized structure of the graphitic layers compared to the randomly oriented graphene that makes up the core.

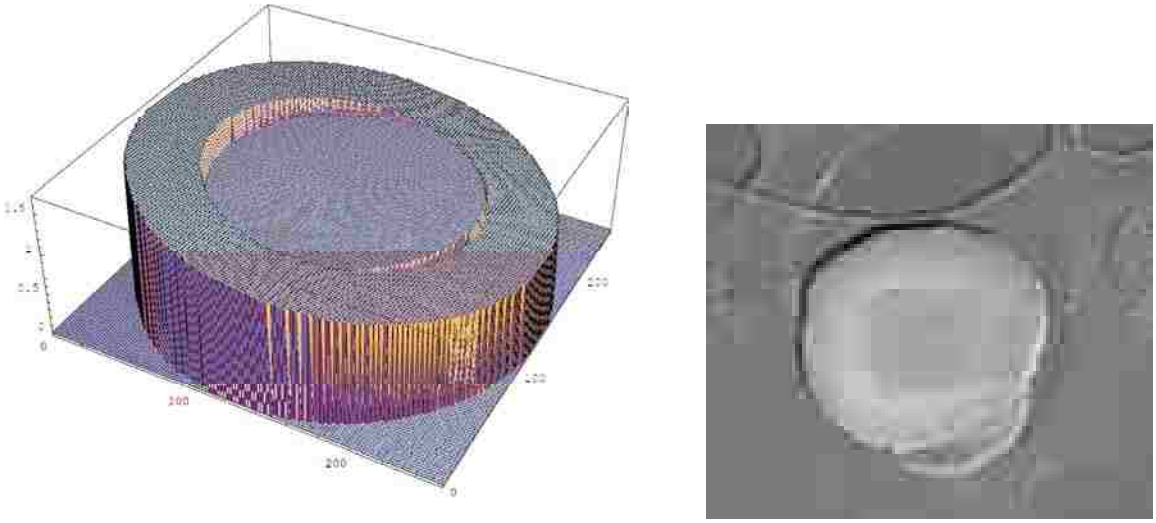

Figure 5.9: The functions for each plane plotted over the approximate pixel range corresponding to the locations of the core and rim sections, and the EFTEM image of the spherule (field of view ~ 1.5[microns]). The core plane is generally less than the rim, except on the far right. The angle between the planes is small, ~3˚.

5.3 SUMMARY

In this work, both EELS and EFTEM imaging have been used to explore density differences between the cores and rims of a subset of graphitic stardust with nanocrystalline cores. Both techniques have revealed the unlayered graphene cores to be less dense than the graphitic rims. Assuming a nominal graphite density for the rims (~ 2.2 [g/cm^3]), the cores have an approximate density of 1.5 [g/cm^3], as measured in EELS and via relative mean-free-path thickness maps, calculated using EFTEM imaging. Three-dimensional

plotting of mean-free-path thickness maps has shown that this density is nearly constant throughout the cores. Plane-fitting applied to the core and rim in the mean-free-path thickness images has been shown to reveal mechanical properties of the grains, themselves, providing a window on the behavior of these grains in the specimen preparation process.

Future work on these grains should consider further trials, measuring the relative mean-free-path thickness between the core and the rim. In addition, carbonaceous material that has been identified recently as being derived from the solidification of liquid carbon might prove useful as a laboratory analog for the graphene cores (Bandow, et. al. 2000; de Heer, et. al. 2005).

6. CONSTRAINTS ON GROWTH AND FORMATION MECHANISMS OF NANOCRYSTALLINE CORES IN PRESOLAR GRAPHITE SPHERULES

Presolar grains, discovered in primitive chondritic meteorites like Murchison, are providing us with perspective on the primary sources of heavy atoms in the Milky Way, and specifically on condensed matter outflows from *s*-process (red-giant star) and *r*-process (supernovae) nucleosynthesis sources (Amari et. al. 1990, 1993; Bernatowicz, et. al. 1987, 1991, 1996; Hoppe et. al. 1995; Lugaro 2005). These stardust grains are identified as presolar by anomalous isotopic ratios (i.e. different than the galactic and solar average value). Among the many identified species of presolar grain are silicon carbide, corundum, spinel, diamond, graphite, and silicates (Lugaro 2005).

Graphitic stardust can be divided into several subsets based on grain morphologies observed in SEM and TEM imaging (Bernatowicz, et. al. 1996). Three types of micron-sized graphitic stardust observed are onion-like spherules, aggregate graphite grains, and cauliflower-like grains (Bernatowicz, et. al. 1996; Croat, et. al. 2005). The onion-like graphites are comprised of concentric graphitic rims, with the nominal (002) graphite lattice spacing between layers, while the cauliflower-like grains consist of turbostratic graphite, or graphite layers that are aligned well only over smaller domains (<50[nm]), leading to a very loose structure in comparison (Croat, et. al. 2005). The aggregate graphite grains appear to be compositions of many onion-like grains.

Onion-type spherules can be categorized further in the TEM, after the grains have been cut with an ultramicrotome into ~70[nm] thick sections. While some of the onion grains have concentric (002) graphitic layers extending throughout the grain, in some cases surrounding a carbide seed crystal at the center of the grain, approximately two-thirds of the surveyed onion-type grains have condensed around a nanocrystalline core (Figure 6.1) (Bernatowicz, et. al. 1996; Croat, et. al. 2005; Fraundorf et al. 2000; Mandell, et. al. 2006). Electron diffraction indicates that the cores are comprised primarily of ~4[nm] graphene sheets with no evidence of graphitic layering. High-resolution TEM imaging of the cores has also shown linear features in images, corresponding to "edge-on" graphene sheets (Fraundorf & Wackenhut, 2002). These often appear bent by the inclusion of a defect, such as a pentagonal unit in the hexagonal graphene lattice.

Figure 6.1: A TEM image of a graphite spherule. This type of stardust exhibits a core-rim structure, where the core is composed of unlayered graphene.

The onion-type spherules with nanocrystalline cores present a challenge for both materials scientists and astronomers. The challenge for materials scientists is to explain how to form a micron-sized carbon sphere and suppress any graphitic layering in the nanocrystalline cores. The challenge for astronomers revolves around explaining the growth and formation of these grains. Some of the criteria to consider in the latter challenge involve the time available to form the grains, sticking coefficients for collisions between atoms and molecules, and the carbon partial pressures in a red giant stellar environment (Bernatowicz, et. al. 1996; Fraundorf & Wackenhut 2002; Lodders & Fegley 1997; Michael, et. al. 2003).

Grains that form in the stellar atmosphere will be pushed outward by the radiation pressure from the star in the stellar outflow, putting quantitative limits on the rim to core diameter ratio (Fraundorf, et al. 2000). For graphite onions with carbide inclusions not normally found in the core-rim grains, models suggest that carbon partial pressures required to grow them are much higher than those expected in spherically symmetric models of AGB atmospheres (Bernatowicz, et. al. 1996). This is the case even when assuming a unit sticking coefficient when experiments suggests that the single-atom sticking coefficient could be much less (Michael, et. al. 2003). This suggests that regions of high carbon density ($> 10^8[cm^{-3}]$) are required to explain the growth of the graphite, at least in those particles in which carbide grains put constraints on thermal history On the other hand, a network of PAHs and graphene might be assembled more quickly by collisional aggregation of pre-formed molecules, although dissipation of intermolecular kinetic energy and packing of the resulting aggregate to “condensed matter” densities are

not easy to explain (Bernatowicz, et. al. 1996). "Icospiral" growth might help in this context (Kroto, et. al. 1985), although the near total suppression of graphite layering followed by a fairly abrupt transition to graphite rims remains unexplained (so far) by any conditions known to exist in the cool outer atmosphere of a red giant, or for that matter on earth.

Electron beam characterization techniques, applied to the nanocrystalline cores, reveal structural detail that can be used to further constrain grain formation. Recent work with electron diffraction data has suggested that not only are the cores comprised primarily of unlayered graphene sheets, but that a sizable percentage of these sheets are in some irregular shape (non-hexagonal), perhaps triangular (Chapter 3). This different shape may be due to some regular coordination between adjacent sheets, sharing a lattice defect. HRTEM images of the cores have revealed linear features, corresponding to "edge-on" graphene, which often appear bent, likely due to defects in the graphene lattice. Greyvalue intensity profiles tangent to these bent features indicates that the atoms around the bend have not fully relaxed. In addition, greyvalue intensity profiles along the linear features shows that these sheets are often triangular, as in diffraction (Chapter 4). Lastly, EELS and EFTEM image data indicate that the cores are significantly less dense than the surrounding graphitic rims (Chapter 5).

Here, three proposed methods of formation are considered; (1) growth of the nanocrystalline cores that proceeds one atom at a time, (2) core growth that occurs through an agglomeration of graphene sheets, or polycyclic aromatic hydrocarbons (PAHS), (3) and

the dendritic growth of graphene sheets deriving from the solidification of a liquid carbon droplet. Each model is described and then evaluated in its ability to explain recently observed aspects of the core structure. This side-by-side comparison indicates that the dendritic growth model might be better able to account for the structural data, suggesting further lines of research into the theory and existence of liquid carbon in stellar atmospheres.

6.1 ELECTRON BEAM CHARACTERIZATION DATA OF GRAPHITE SPHERULES

Electron diffraction data from the core material shows rings corresponding to the (hk0) graphite in-plane periodicities and no presence of any (002) graphitic layering (Figure 3.1). When this data is azimuthally-averaged, high-frequency tails are seen on each of the peak periodicities. These combined observations require that the core material be comprised primarily of unlayered graphene (Bernatowicz, et. al. 1996). Currently, there is no analog laboratory material that can reproduce this diffraction data, as even amorphous carbon has a broad (002) feature in diffraction.

Diffraction data not only carries information about lattice periodicities in the cores, but the shape of the graphene sheets, as well. Comparisons between hexagonal and triangular graphene diffraction models and the experimental data have shown that the triangular model is a better fit by 13% using a least squares method. This fit is further improved by another 7% when considering models with coherence effects in diffraction, which manifest when sheets are bent, due to the inclusion of an in-plane lattice defect.

Also, HRTEM imaging of the core material has not only allowed for the observation of "edge-on" graphene within the cores, but has shown many of the linear features to be bent (Fraundorf & Wackenhut 2002). Greyvalue intensity profiles tangent to these bent features suggest that the atoms near the bend have not been able to fully relax around a defect, as in a relaxed carbon nanocone, but appear more faceted, as if sheets are seamed together. In addition, the presence of triangular sheet shapes is seen in image intensity profiles along linear features. Formation models should be able to explain why the graphene within the core has not grown isotropically (hexagonal), and how sheets have become faceted.

High-Angle Annular Darkfield (HAADF) images of graphene cores have revealed the presence of isolated heavy atoms interspersed throughout the matrix. While this data has yet to be used to identify the atomic number of the heavy atoms, their locations in the core material are another piece of structural information for consideration. Atoms are able to diffuse in bulk solids, typically from areas of high concentration to low, and would likely bond to form a nanocrystal as they become near enough to one another. During the growth of these grains, something has interfered with the natural diffusion process, as the atoms have been seemingly frozen into place.

Lastly, core density measurements from EELS and EFTEM imaging indicate that the core is significantly less dense than the concentric graphitic rims. Because both the cores and rims are comprised almost entirely of carbon and have nearly the same physical thickness, due to the specimen preparation process, differences in mean-free-path seen in

electron energy loss spectra are indicative of density differences. Mean-free-path thickness images, calculated using EFTEM imaging, are able to illustrate these density differences as differences in greyvalue (Figure 5.4). Both analyses indicate that the cores have roughly 70% the density of the rim. Proposed formation mechanics must also be able to account for the change in density between the rim and the core, and the packing of graphene accomplished in the core without layering.

6.2 THREE CORE GROWTH MODELS

Here, three core growth models are proposed for later comparison, given the structural characteristics of the core. The three models are growth by one atom at a time, growth through an agglomeration of polycyclic aromatic hydrocarbons (PAHs) and graphene sheets, and growth through the dendritic solidification of a liquid droplet. These represent three plausible models that explain how carbon might come together in a red giant atmosphere and could give rise to the basic graphene structure seen in the cores.

6.2.1. Growth by One Atom at a Time. In this first model, the growth of the core is considered as beginning with a single carbon atom. As carbon atoms collide and bond with the first, they will begin to form a hexagonal lattice. If there is occasionally a defect in this lattice, such as a pentagonal bond network, the graphene sheet will bend out of the plane. This process of adding one atom at a time continues, where portions of the graphene network are occasionally bent out of the plane through the inclusion of a defect. This results in a core structure similar to an "icospiral" network of graphene (i.e. Kroto shell). If there is enough time before being "frozen" into place by bonding to additional atoms,

carbon near the in-plane defects will relax, resulting in a more curved structure. This core growth could be taking place in a high carbon density region where atoms are added very quickly. Upon reaching a less dense region, the increased time between addition of atoms allows the spiral shell to relax as it grows, resulting in the layered rims (Bernatowicz, et. al. 1996). Alternatively, the rim might be grown by a process akin to chemical vapor deposition (CVD).

6.2.2. Growth by Accretion of Graphene Sheets and PAHs. PAHs and graphene are both thought to be present in red giant atmospheres (Allamandola, et. al. 1989; Cherchneff, et. al. 1992; Frenklach & Feigelson 1989). The second proposed growth model is that the graphene cores formed through the rapid accretion of PAHs and graphene sheets. PAHs are essentially graphene with hydrogen-terminated bonds around the perimeter of the sheet and are considered to be much smaller than the ~4[nm] average graphene sheet size. The quick coalescing of these sheets and PAHs in a high density region of the atmosphere might result in a large collection of these structures, randomly-oriented with respect to one another. Any defects within the PAH or graphene sheet structure should have carbon atoms relaxed around the defect, as these formed as atom-thick structures in free space. Again, the rim could be deposited by either of the processes discussed in Section 6.2.1.

6.2.3. Dendritic Growth by Solidification of a Liquid Droplet. The third proposed growth model involves the solidification of a liquid droplet. Under conditions where carbon "rain" might form in a stellar atmosphere, it will likely freeze quickly due to the

narrow range of pressures and temperatures over which liquid carbon is thought to exist. Given a large number of carbon atoms, each with many nearest neighbors in the fluid, freezing would likely result in the dendritic growth of flat graphene sheets with the nearest atom to the plane of the sheet getting a chance to bond in. When an out-of-plane defect does occur at the growth edge, the plane of a new sheet might thereby be defined giving rise to faceting down seams between sheets. Figure 6.2 shows an atomic model of what two seamed sheets might look like, given they branch from the same defect. There is little, to no relaxation around these defects because there is simply no room to relax. Once the droplet has frozen and has become a maze of networked, seamed graphene, the rims could again be grown through either of the previously described methods.

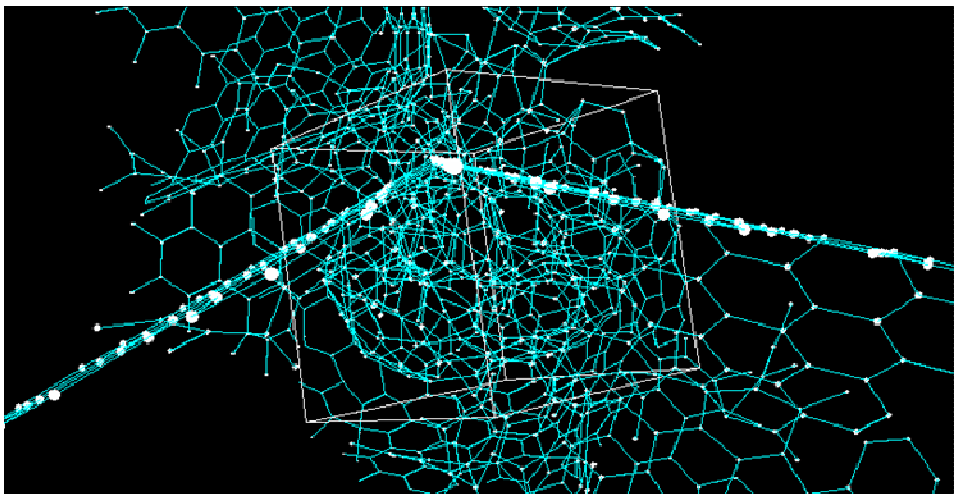

Figure 6.2: An atomic model of dendritic graphene, representative of what might occur in a frozen liquid carbon droplet. In this case, two graphene sheets are seamed together as they grow away from a pentagonal defect.

6.3 GROWTH MODEL EVALUATION AND SUMMARY

Each of the three growth models presented in the previous section can now be examined in order to evaluate whether they can explain the core structural data derived from electron beam techniques, as well as restrictions due the stellar environment, where formation occurs. A table has been constructed to provide a visual framework for this discussion, which lists the three growth models along the top row, and various structural characteristics of the core material, or challenges, down the far left column (Figure 6.3). In the fashion of a Consumer Reports™ evaluation chart, the emotion indicated by the face in each grid box denotes the match between each growth model and a given set of observations.

The first observations on the chart involve environmental conditions in dust forming regions of the star. Both carbon and PAHs are known via spectroscopic observations (Chiar, et. al. 2004) to be present in AGB atmospheres, while there is no observational evidence to date for hot carbon droplets. As discussed later, it's likely that if liquid carbon is present it is probably short-lived and only present in areas that are optically dense. Hence at least the lack of observational evidence for it may be expected. Processes that might produce carbon droplets, including jets or backflows, in AGB atmospheres do not appear to have been explored in much detail as of yet (Woitke 2006).

When it comes to collisions, the kinetic energy of individual PAH on PAH collisions seems likely to break them apart rather than result in the formation of a compact spherical structure. The average kinetic energy of a carbon atom in this stellar wind (~10[km/s]) is at

least on the order of the potential bond energy between atoms in graphene (Whittet 1992). Any structure forming will be susceptible to collisions between atoms with this energy, or higher, causing significant "knock-on" damage and making it difficult to maintain a bonded structure. Thus, sticking coefficients are likely to be far from unity, making it very difficult to accrete matter in the first two growth models (Michael, et. al. 2003; Roth & Hopf 2004). The rating given to the dendritic growth model for the carbon sticking coefficient challenge represents a lack of knowledge of the conditions that might lead to the formation of carbon rain in the stellar atmosphere.

The sharp core to rim transition could be easily explained in the dendritic growth model as being due to the vapor deposition of carbon atoms after the freezing of the core material. Meanwhile, the PAH accretion model lacks an explanation as to why PAH accretion (forming the cores) stops and rim growth begins by single atoms. It is not clear if PAHs should only exist within a finite region of the stellar atmosphere, or what other mechanism could allow for the sudden changeover from core to rim. In contrast, the atom by atom model is at least forming the cores one atom at a time, using the same single atoms necessary for rim growth. Thus, in this case the rating for the atom-by-atom model represents the possibility that as the grain was pushed further out into cooler regions of the stellar atmosphere, an environmental change made graphitic layering favorable over continued rim growth.

As stated earlier, carbon partial pressures in red giant atmospheres, suggested by spherically symmetric models, are not sufficient to explain the growth of the graphene

Observations\Model	Atom by Atom Growth	PAH Accretion	Dendritic Melt Solidification
Starting Material Present	☺	☺	☹
Carbon Partial Pressures & Sticking	☹	☹	😐
Radiation Pressure and Rim Growth	😐	😐	😐
Compact Spherical Shape	😐	☹	☺
Sharp Core to Rim Transition	😐	☹	☺
Unlayered Graphene	☹	😐	☺
Triangular Sheet Faceting HREM&Diff	☹	☹	☺
1.5g/cc<density<2g/cc	😐	☹	☺
Unclustered heavy atoms	😐	😐	☺

Figure 6.3: A table comparing three different formation models and their ability to address various challenges evidenced in the structural data. Smiling faces indicate that the evidence is consistent with the model, while frowning faces coincide with a model's seeming inability to explain the observed data. Expressionless faces indicate uncertainties in a model's ability to meet the requirements of a particular challenge.

cores under any of these models, indicating the need for much denser dust-forming regions (Bernatowicz, et. al. 1996). This in turn reflects on the time available to grow the rim. If the cores form by the dendritic solidification of a liquid droplet, there will be more time remaining to grow the rim as the grain is pushed away from the star than in either of the other two scenarios, which require that core growth occur on a greater time scale, being slowly built up from a number of individual constituents.

The dendritic model also lends itself well to explaining the compact spherical shape. Surface tension will certainly dominate the shape of a liquid droplet, possibly preserving that shape upon freezing. Formation by one atom at a time might statistically allow for a general spherical shape over time as a Kroto-shell is grown slowly, though it is slightly more difficult to imagine an agglomeration of PAHs resulting in a necessary spherical shape each time. Random orientations of PAHs colliding should not build an object so dense and necessarily spherical.

The last four challenges presented in Figure 6.3 consist of structural evidence discovered via electron beam analyses. The atom by atom growth model runs into difficulty in explaining the presence of unlayered graphene. A spiral graphitic network would have some definitive coordination between sheets and would likely have some type of layering periodicity associated with the distance between successive shells (Zhang et. al., 1985). It is also difficult to imagine faceting rising out of such a model because the carbon should be able to relax around defects, as they are included in the lattice. This in turn makes it difficult to conceive of triangular-shaped graphene resulting from this spiral shell growth. While the density would be likely near that of graphite, it actually seems it would be too high to explain the less dense cores.

The proposed formation model by PAH agglomeration runs into similar problems when considering the experimental data. Firstly, the merging of randomly-oriented PAHs would leave large gaps void of any other atoms within the core material. Thus, it is very difficult to imagine arriving at a final product with anything near the density observed.

Also, because carbon atoms would have time to fully relax around any lattice defects within the PAHs, prior to accretion, both the faceting and the odd sheet shape are difficult to explain, though this model is able to build a core that would appear to be composed of unlayered graphene.

The dendritic growth model is able to explain the suppression of graphitic layering by beginning with many atoms close together in a liquid droplet. As the droplet freezes and graphene begins to grow, there is not enough space for Van der Waals bonded layers, associated with graphite, to form. The onset of graphene sheet growth would result in strained carbon around defects, as the nearest neighbor distances between atoms in other graphene sheets prevents full relaxation. This causes there to be graphene sheets that appear seamed together, branching away from defects. In this instance there have been reports on the density of frozen liquid carbon beads, involved in the formation of nanotubes, which is very similar to the density of the cores reported here (~1.5[g/cm^3]) (de Heer, et. al. 2005; Poncharal, et. al. 1999).

As for the evidence of isolated heavy atoms, they could have been "frozen" into place in the dendritic growth model without enough time to diffuse and bond. In the other two models, they could have been added periodically as the lattice grew, or PAHs were added. In each case, it is not clear how the atoms became "stuck" there, or why they were not able to diffuse short distances through the unfinished lattice to cluster. It could very well be that because the C-C bond is so small (1.42[Å]), graphene is very resistant to diffusion; especially in a random graphene network that might arise out of these two models. More

work is required in identifying the atomic number of the isolated heavy atoms seen in HAADF images, and estimating number densities, which might further constrain how this observation reflects on each of these proposed growth models.

Proposed growth models for the formation of presolar graphene cores have been examined in light of new structural characterization data, obtained via electron beam techniques. While none of the models are able to necessarily meet all of the challenges presented by these grains, the model of dendritic solidification of a liquid droplet performs the best when it comes to answering the new challenges presented here. Perhaps more importantly, it is difficult to imagine how the growth of the cores by one atom at a time, or by a rapid accretion of PAHs, might explain evidence of faceting between graphene sheets, triangular shaped sheets, or the density. This new set of challenges and measurements raises more questions than it necessarily answers, provoking thought on stellar atmospheric models that could account for the graphite spherules. One possible consideration might be "backwarming" observed in 2D models of AGB stellar winds, which could account for warmer regions, perhaps capable of condensing carbon in a liquid droplet form, while here on Earth, material observed to play a role in the formation of carbon nanotubes in a pure carbon arc might be similar structurally to that found here in the cores of graphite spherules (de Heer, et. al. 2005; Woitke 2006).

APPENDIX A.

NANOTUBE PROFILES IN EFTEM IMAGES

Relative mean-free-path thickness images can be calculated from two images obtainable in an energy-filtered TEM (Egerton & Leapman 1995; Egerton 1996). The two required images are a regular brightfield, phase-contrast image, and a zero-loss image, formed using only zero-loss electrons. The result when taking the natural log of the ratio of greyvalues for corresponding pixels in these images is an inelastic mean-free-path thickness map (Equation A1), which allows for the relative comparison of projected mass thickness from point to point in the image.

$$I_{MFPthickness} = \ln\left[\frac{I_{brightfield}}{I_{elastic}}\right] \tag{A1}$$

Greyvalue intensity profiles of nanotubes in relative mean-free-path thickness images can be compared to expected projected mass thickness functions across the tube, potentially measuring any severe departures from cylindrical symmetry. However, there is also some question as to whether the (002) diffracting regions of a multi-walled tube would affect the calculation of the relative thickness image. This is because the nanotube walls will be responsible for the elastic, Bragg scattering of electrons. These electrons may or may not be collected given the physical size of the energy selecting aperture, when taking the zero-loss image. To rephrase the issue at hand, is the potential lack of contribution of elastically scattered electrons from the tube walls going to drastically change the zero-loss image in such a way that the calculated thickness map is unreliable?

To explore this issue, experimental brightfield and zero-loss images of bamboo multi-walled nanotubes were obtained using a Leo-Zeiss 912 with an integrated Omega energy filter. The objective aperture was approximately 13[mrad] for EFTEM imaging, and was

used with an energy selecting aperture of 15[eV] resolution, typical for operation in ESI (Electron Spectroscopic Imaging) mode. A relative mean-free-path thickness map (Figure A1) was then calculated using a zero-loss image and a regular brightfield image, as described above. Sections of the tubes where the walls were nearly parallel were chosen for profiling. Averaging greyvalues along the direction of the tube axis, within the profile window, resulted in the profile shown as the scatter plot data in Figure A2. When compared to the expected projected mass thickness function (the blue line in Figure A2) for a multi-walled tube with an inner and outer radius as measured from the experimental images, both the line and scatter data overlap very well. Differences seen here are attributed to the large amount of drift that has occurred between the brightfield and zero-loss images, observable by the large shadows seen in the relative mean-free-path thickness map. The drift seems to be directed to the right and slightly downward in the image. Even with this drift, we are able to confirm the expected mass thickness function for a cylindrical multi-walled tube, and rule out any sizable effects from the (002) diffracting regions of the tubes.

The red line in Figure A2 is a model profile that demarcates the (002) diffracting regions of the tube and represents the strength of effects that might result due to elastic scattering from the tube walls. If these effects were large, we would expect deviations between the experimental profile and the mass thickness profile to occur in the walls of the tube. These deviations would be of a form similar to this red line, though none are observed.

Though there was reason to give pause as to whether mean-free-path differences between the walls of the tube and the center of the tube would be accurately represented in the calculated mean-free-path thickness maps, this experiment suggests that they will. This analysis could be fairly extended to any graphitic carbon specimen (i.e. multi-walled nanocones, nanohorns, carbon onions), given similar scope parameters and objective aperture size.

Figure A1: A relative mean-free-path thickness map of a bamboo multi-walled nanotube calculated using brightfield and zero-loss, phase contrast, images. The profile across the tube is taken in the window shown where greyvalues are averaged along the direction of the tube axis. The question is whether the (002) diffracting walls of the tube will affect conclusions about the physical thickness of the tube using this mean-free-path thickness map.

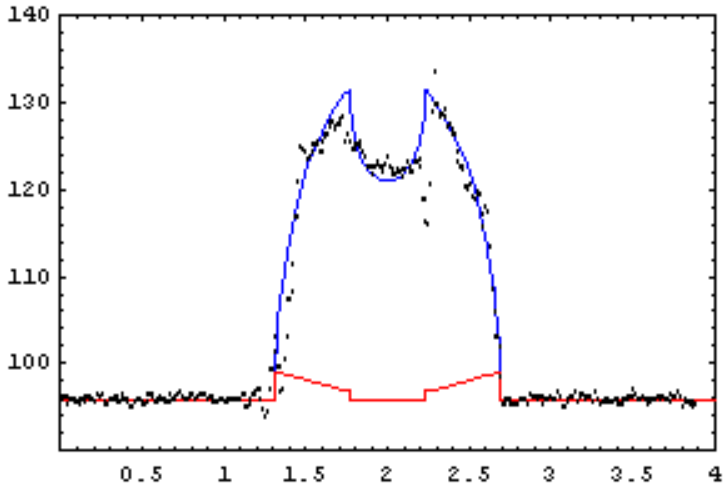

Figure A2: The experimental profile (scatter data) superimposed on the expected projected mass thickness profile (blue line) for a multi-walled nanotube with the same inner and outer radius seen in Figure A1. The red line represents the (002) diffracting regions of the tube, where deviations from the expected mass thickness function might be observed due to the large amount of elastic scattering.

APPENDIX B.

POWDER PATTERNS FROM NANOCRYSTAL LATTICE IMAGES

(As appeared in Microscopy and Microanalysis 10 S(02) (2004), 1254-1255)

Eric Mandell[1], P. Fraundorf[1], and M. F. Bertino[2]

[1]Dept. of Physics & Astronomy, University of Missouri-St. Louis, St. Louis MO 63117

[2]Department of Physics, University of Missouri-Rolla, Rolla MO 65409

Fringes in electron phase, and Z, contrast images contain (among other things) the same “Fourier phase information” used in conventional darkfield imaging to locate objects of selected periodicity. However, conventional darkfield apertures often vignette in azimuth, and/or cannot distinguish frequencies whose spacing differs by less than 10%. Lattice images of multiple nanocrystals facilitate an alternate approach to analyzing both fringe abundances (illustrated here), and cross-fringe correlations (discussed in a separate abstract).

At the University of Missouri - Rolla, AgPt nanoparticles with high aspect ratio were grown in "necklace form" with crystal links 3-5[nm] long and 2-4[nm] in breadth, separated by occasional "large" equant knots (up to perhaps 10[nm] in diameter) (Doudna, et. al. 2003). The question we address here: Can HRTEM imaging provide insight into segregation between Ag and Pt across the various components of these nanochains, given that Ag and Pt have strong (111) diffraction peaks at spatial frequencies of 2.36[Å] and 2.26[Å] respectively, making it impossible to distinguish them grain by grain e.g. by darkfield imaging (Wyckoff 1982)?

Figure B1 is a 240,000x magnified image taken with a Phillips EM430ST microscope which shows the chain-knot strands streaming off of a large clump of silver. Using Adobe Photoshop with IPTK plugins and/or ImageJ, we are able to take power spectra of selected regions of specimen images digitized at 2400 dpi, and measure spatial frequencies (Figure B2) (Russ 1999). By taking many individual power spectra of various parts of chains and knots and measuring spatial frequencies, a histogram of spatial frequencies associated with links and knots was then compared to powder diffraction profiles of Ag and Pt.

Fringe spacings thus allow one to correlate with each object type the range of randomly encountered Bragg spacings. Interesting patterns emerge from the data in Figure B3. For example, the profiles in Figure B3 suggest that the knots are largely Ag. Our analysis also suggests that the chains have a sharp peak in lattice parameter, quite near the 2.26[Å] peak for Pt though shifted slightly towards the higher lattice spacing of Ag. Projection broadening of fringes due to the small (e.g. 2[nm]) grain cross-sections is one possible explanation.

Specimens with less similar structures would of course make identification of trends even easier. Although the analysis described here was done by manually analyzing power spectrum peaks in 136 individual grains, the technique also lends itself to automation by simple azimuthal intensity averaging, provided regions for differential comparison can be otherwise flagged for the computer. Polycrystalline films in profile, with hopelessly overlapping grains, can also be analyzed in this way. The usefulness of this strategy will

increase with the availability of large digitized images containing projected lattice fringe information.

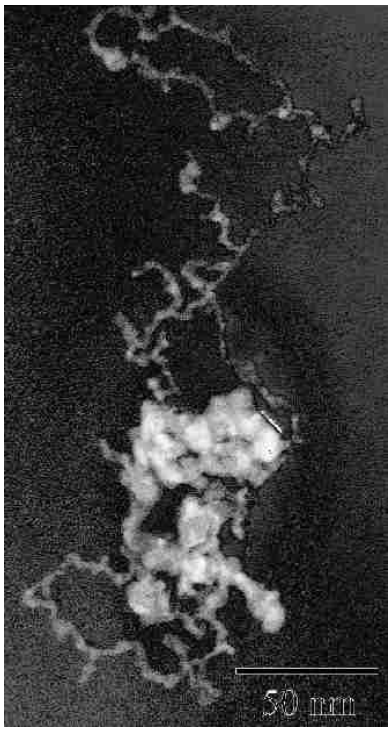

Figure B1: A TEM image of AgPt nano-chains at 240,000x. The darker regions are larger clumps of silver.

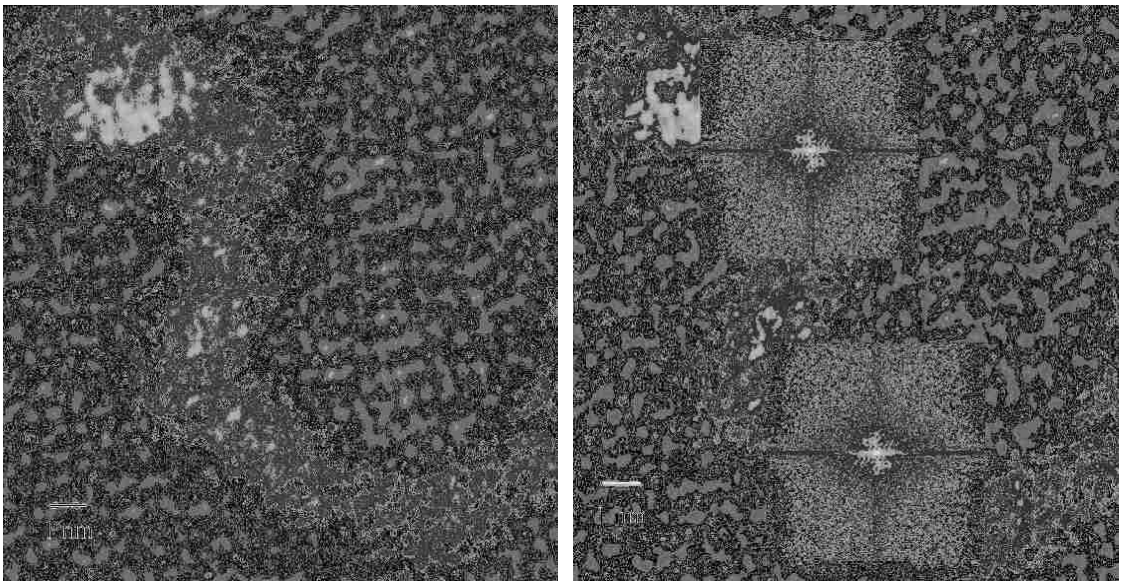

Figure B2: Platinum crystal “links” in a chain approximately 2[nm] in width. The length to width ratio of the nanocrystals is approximately 3:2. The power spectrum was calculated for the local region of each section of the nano-chains and measured lattice spacings were recorded.

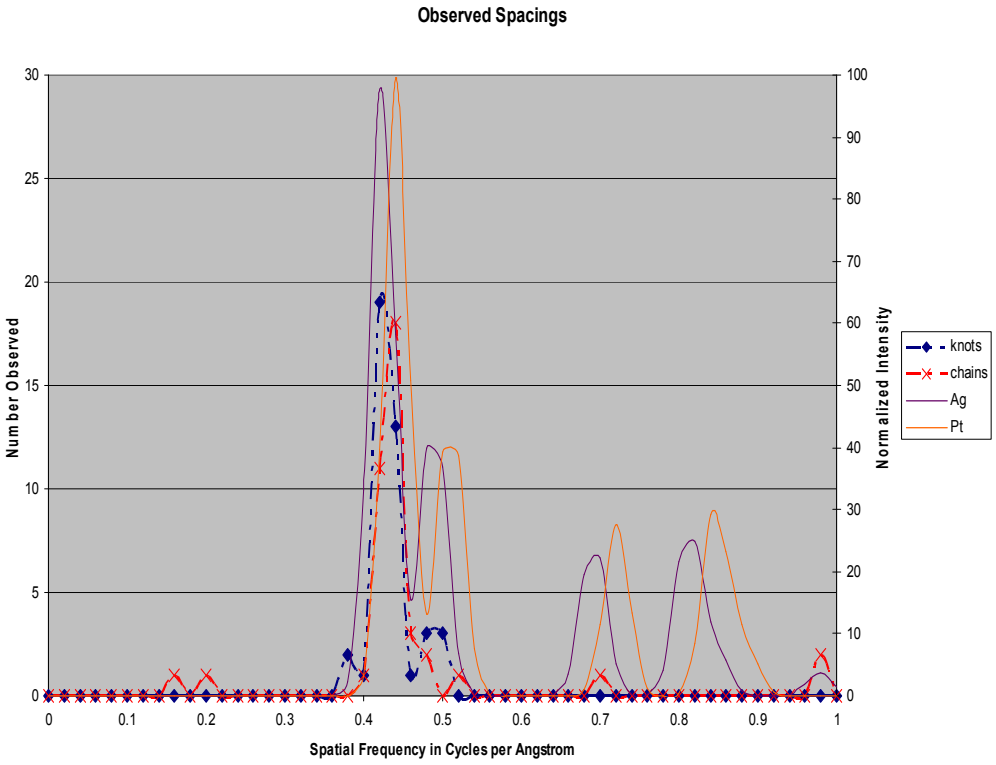

Figure B3: A histogram comparison to diffraction data for Ag and Pt. The left-most solid line is Ag and the other solid line is Pt. We see the knots have a strong peak under the Ag, 2.36Å spacing, while the chains have a peak more centered under the 2.26Å spacing of Pt.

APPENDIX C.

MEASURING LOCAL THICKNESS THROUGH SMALL-TILT FRINGE VISIBILITY

(As appeared in Microscopy and Microanalysis 10 S(02) 2005)

E. Mandell[1], P. Fraundorf[l], W. Qin[2]

[1]Dept. of Physics and Astronomy, University of Missouri-St. Louis, St. Louis, MO 63121

[2]Technology Solutions, Freescale Semiconductor, Inc.

Specimen thickness measurements are often limited to analyzing one region at a time, and by the size of the electron probe. With increased availability of lattice fringe data in phase and z contrast images, information on how fringes change with tilt is also more accessible. We discuss how such data can provide thickness information on specimen regions only nanometers on a side, provided that they are thin enough for lattice imaging. Using micrographs 1/3 of a micron across, many regions can be analyzed with only a few images.

When tilting a nanocrystalline specimen, one encounters a band of incident electron angles that give rise to visible fringes for a particular crystal lattice spacing (Allpress & Sanders 1973). The width of this range is,

$$\alpha_{\max} = \sin^{-1}\left[\frac{df}{t} + \frac{\lambda}{2d}\left(1 - \left(\frac{df}{t}\right)^2\right)\right], \qquad \text{(C1)}$$

where d is the lattice spacing, t is the crystal thickness, λ is the electron wavelength, and f is a "visibility factor" (approximately equal to 1) that accounts for the signal-to-noise ratio in detecting fringes (Qin & Fraundorf 2005). For specimens < 10[nm] thick and the small λ

typical of most electron microscopes, Equation C1 becomes $\alpha_{\max} \cong df / t$. The ensemble of all visibility bands of a spherical crystal, oriented properly with respect to one another on a sphere, forms a fringe-visibility map (Fraundorf, et. al. 2005; Qin & Fraundorf 2005; Qin 2000). If the visibility band half-width is α_{max}, the angle between the reciprocal lattice vector and the tilt direction is φ, and the total tilt range over which the fringes are visible is θ, as shown in Figure C1, the Spherical Trigonometry's Law of Sines gives us

$$\sin[\alpha_{\max}] = \sin[\varphi]\sin\left[\frac{\theta}{2}\right]. \tag{C2}$$

Equation C2 in combination with a simplified form of Equation C1 yields an expression for crystal thickness that depends on the experimentally measured quantities d, φ, f and θ (Fraundorf, et. al. 2005).

$$t \cong (df)\csc\left[\frac{\theta_{range}}{2}\right]\csc[\varphi] \tag{C3}$$

Figures C2 and C3 show an example of two TiO_2 grains from the same set of negatives taken at various tilts. The grain in Figure C2 has fringes oriented such that φ = 60° for the grain in Figure C3. Estimates for θ_{range} were obtained for each grain by measuring fringe intensity, and used to calculate a value for t/f in Angstroms. These two points are shown on Figure C4, which is a series of plots of t/f versus θ_{range} for different values of φ with d = 3.5[Å] and λ = 0.01[Å]. Inferred thicknesses are comparable to grain widths, as expected for this set of randomly-oriented equant grains.

The primary errors come from uncertainties in θ_{range} and f. The variability of f, like the value of f itself, may be investigated for a given microscope, specimen type, and operational definition for θ_{range}. Errors in f cause equivalent % errors in t. Goniometer accuracy will be crucial for minimizing errors in θ_{range}, even given a clear operational definition, particularly for grains with large thickness and/or φ near 90°. In Figure C4, note that for grains with small φ and sufficiently large tilt range that determinations of t/f can be quite accurate. Also note that overlapping grains may also be analyzed independently by this technique, as long as each has visible fringes, and refocusing between tilts can be done reliably.

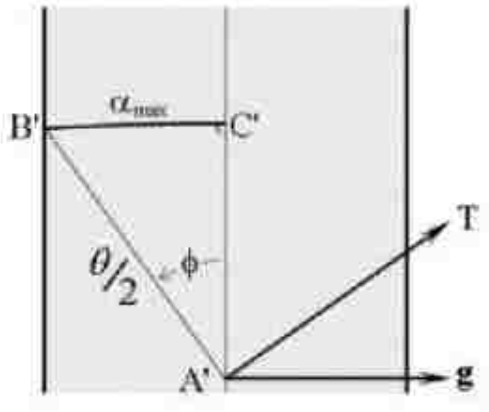

Figure C1: A segment of a visibility band. The half-bandwidth, α_{max}, angle between the reciprocal lattice vector and the tilt direction, φ, and the range of tilt over which the fringes remain visible, θ, allow for the determination of nanocrystal thickness.

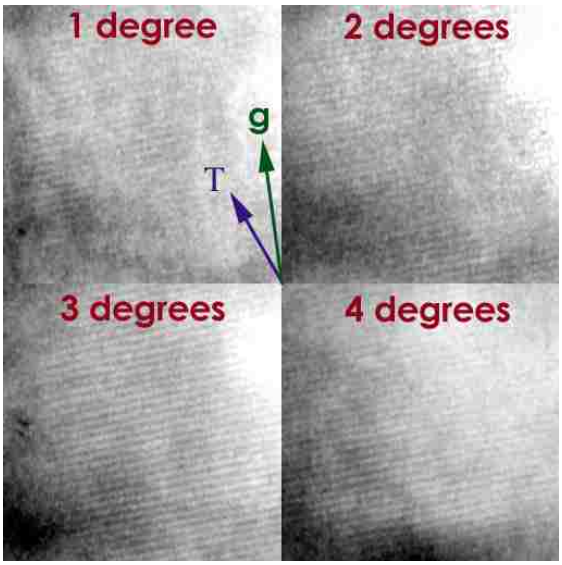

Grain 1

Figure C2: A set of image data for grain 1, a TiO_2 nanocrystal, where the reciprocal lattice vector makes a small angle with the tilt axis vector. Thus, it is expected that the fringes should be visible over a wide range of tilts. The intensity of the fringes peaks at 3 degrees.

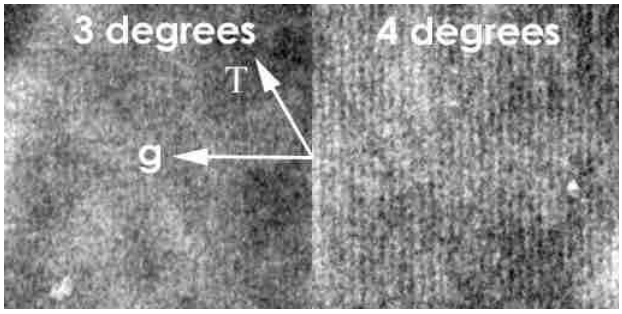

Grain 2

Figure C3: A set of image data for grain 2, another TiO_2 nanocrystal, where the reciprocal lattice vector makes a large angle with the tilt axis vector. Thus, it is expected that the fringes should be visible only over a short range of tilt.

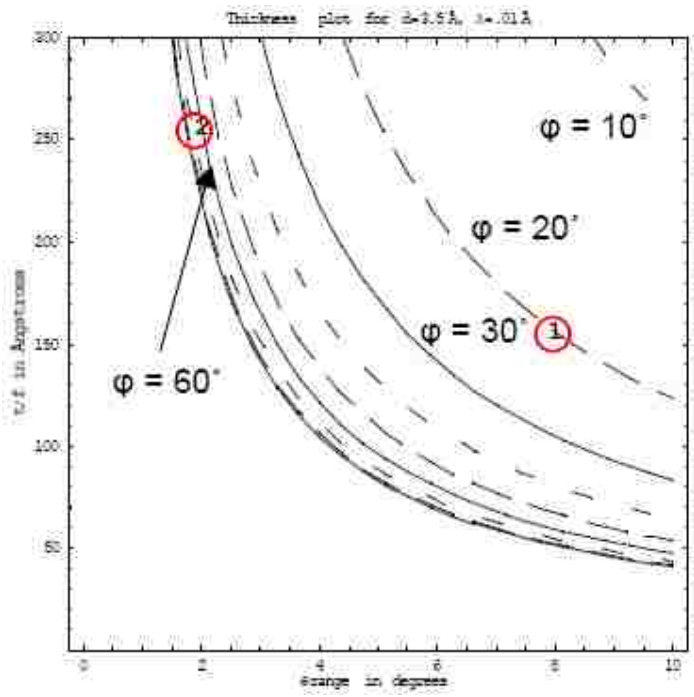

Figure C4: A theoretical series of plots of *t/f* versus θ_{range} for different values of φ with d = 3.5[Å] and λ = 0.01[Å]. These plots can provide a gauge of how uncertainties in θ_{range} can affect uncertainties in the measured thickness. Points 1 and 2 correspond to the estimated θ_{range} for grains 1 and 2 from experimental images taken at one-degree tilt intervals.

BIBLIOGRAPHY

Allamandola L J, *et. al.*, ApJ Supplement Series **71**, 733 (1989)

Allpress J G & Sanders J V, J. Appl. Cryst. **6**, 165-190 (1973)

Amari S, *et. al.*, Nature **345**, 238-240 (1990)

Amari S, *et. al.*, ApJ **394**, L43 (1992)

Amari S, *et. al.*, Nature **365**, 806-809 (1993)

Amari S, *et. al.*, Meteoritics **30**, 679 (1995)

Bandow S, *et. al.*, Chem. Phys. Lett. **321**, 514-519 (2000)

Benninghoven A., *et. al.*, *Secondary Ion Mass Spectrometry: Basic Concepts, Instrumental Aspects, Applications, and Trends*, Wiley, New York (1987)

Berber S, *et. al.*, Phys. Rev. B **62**, R2291-R2294 (2000)

Bernatowicz T, *et. al.*, Nature **330**, 728-730 (1987)

Bernatowicz T, *et. al.*, ApJ **373**, L73 (1991)

Bernatowicz T, *et. al.*, ApJ **472**, 760 (1996)

Bernatowicz T & Walker R M, Physics Today **26**, December (1997)

Bernatowicz T, *et. al.*, Proceedings of the Lunar and Planetary Science Conference (2005)

Bundy FP, J. Geophys. Res. **85 (B12)** 6930 (1980)

Cherchneff I & Barker J R, ApJ **394**, 703 (1992)

Chiar, J E, *et al*, ApJ **537**, 749 (2000)

Croat T K, *et. al.*, ApJ **631**, 976-987 (2005)

De Heer W A, *et. al.*, Science **307**, 907-910 (2005)

Dhara S, *et. al.*, arXiv:cond-mat/0401630v1 (2004)

Doudna C M, *et. al.*, J. Phys. Chem. B **107**, 2966 (2003).

Dresselhaus M S, *et. al.*, *Science of Fullerenes and Carbon Nanotubes*, Academic Press, San Diego (1996)

Egerton R F & Leapman R D, *Quantitative Energy-Loss Spectroscopy*, Springer Series of Optical Sciences **71**, 269 (1995)

Egerton R F, *Electron Energy-Loss Spectroscopy in the Electron Microscope*, Plenum Press, New York (1996)

Ewels CP, *et. al.*, Chem. Phys. Lett. **351**, 178-182 (2002)

Fraundorf P, *et. al.*, Met. Soc. Abstracts (2000)

Fraundorf P & Wackenhut M, ApJL **578**, L153 (2002)

Fraundorf P, *et al.*, J. Appl. Phys. **98**, 114308 (2005)

Frenklach M & Feigelson E D, ApJ **341**, 372 (1989)

Gilliland E R & Harriot P, Industrial and Engineering Chemistry **October**, 2195 (1954)

Hansson A, *et. al.*, Phys. Rev. B **62**, 7639-7644 (2000)

Hashimoto A, *et. al.*, Phys. Rev. Lett. **94**, 045504 (2005)

Ho M H, *et. al.*, Acta Cryst. A44, 878-884 (1988)

Hoppe P, *et. al.*, Geochim. Cosmochim. Acta **59**, 4029 (1995)

Howie A, J. Microsc. **177**, 11, (1979)

Hren J J, *et. al.*, *Introduction to Analytical Electron Microscopy*, Plenum Press, New York (1986)

Hunton N, *Diffraction Analysis of Graphene Starsmoke*, Proceedings of NASA/MO Space Grant Consortium (2004)

Iijima S, J. Cryst. Growth **50**, 675-683 (1980)

Iijima S, J. Phys. Chem. **91**, 3466-3467 (1987)

Iijima S, Nature **354**, 56 – 58 (1991)

Iijima S, *et. al.*, J. Chem. Phys. **104**, 2089-2092 (1996)

Jaszczak J, *et. al.*, Carbon **41**, 2085-2092 (2003)

Kasuya D, *et. al.*, J. Phys. Chem. B **106**(19), 4947-4951 (2002)

Kirkland E J, *Advanced Computing in Electron Microscopy*, Plenum Press, New York and London (1988)

Kroto, *et. al.,* Nature **318**, 162-163 (1985)

Liu Z, *et. al.*, App. Phys. Lett. **72**, 1823-1825 (1998)

Lodders K & Fegley B, AIP Conference Proceedings **402**, 391-424 (1997)

Lugaro M, *Stardust From Meteorites: An Introduction To Presolar Grains*, World Scientific Pub Co Inc (2005)

Malis T, *et. al.*, Journal of Electron Microscopy Technique **8**, 193-200 (1988)

Mandell E, *et. al.*, arXiv:cond-mat/0606093v1 (2006)

Menon M, *et. al.*, J. Chem. Phys. **104(15)**, 5875-5882 (1996)

Michael S, *et. al.*, ApJ **590**, 579 (2003)

Murr L E & Soto K F, Materials Characterization **55**, 50-65 (2005)

Novoselov K, *et. al.*, Nature **438**, 197-200 (2005)

Oberlin A, *et. al.*, J. Cryst. Growth **32**, 335 (1976)

Peres N M R, *et. al.*, Phys. Rev. B **72**, 174406 (2005)

Poncharal P, *et. al.*, Science **283**, 1513 (1999)

Qin C & Peng L M, Phys. Rev. B **65**, 155431 (2002)

Qin W, *Direct Space (Nano)Crystallography via HRTEM*, Ph.D. thesis, University of Missouri - St. Louis/Rolla (2000).

Qin W & Fraundorf P, Microsc. Microanal. **11** S(2), 1960-1961 (2005).

Reimer L, *Transmission Electron Microscopy: Physics of Image Formation and Microanalysis*, Springer-Verlag, New York (1997)

Roth J & Hopf C, Journal of Nuclear Materials **334**, 97-103 (2004)

Russ J C, Reindeer Games, *The Image Processing Toolkit* Version 3.0 (1999).

Saito R, *et. al.*, Appl. Phys. Lett. **60**, 2204-2206 (1992)

Spence J C H, *Experimental High-Resolution Electron Microscopy*, Oxford University Press, New York (1988)

Stadermann F J, *et. al.*, Proceedings of the Lunar and Planetary Science Conference (2004)

Stadermann F J, *et. al.*, Geochimica et Cosmochimica Acta **69**, 177-188 (2005)

Ugarte D, Nature **359**, 707-709, October (1992)

Veranth JM, *et. al.*, Fuel **79**, 1067-1075 (2000)

Wang Z L & Hui C, *Electron Microscopy of Nanotubes*, Kluwer Academic, Boston (2003)

Warren B E, Phys. Rev. **59**, 693-698 (1941)

Warren B E, *X-Ray Diffraction*, Addison-Wesley/Dover, New York (1969/1990).

Whittet D C B, *Dust in the Galactic Environment*, Institute of Physics Publishing, New York (1992)

Williams David B and Carter C B, *Transmission Electron Microscopy*, Plenum Press, New York (1996)

Woitke P, arXiv:astro-ph/0602371v1 (2006)

Wyckoff R G W, *Crystal Structures*, Kreiger Publishing Company, Malabar Florida (1982)

Yu M F, *et. al.*, Science **287**, 637-640 (2000)

Zhang Q L, *et. al.*, Journal of Physical Chemistry **90** (1986)

Zuo J M, *et. al.*, Science **300**, 1419-1421 (2003)

VITA

Eric Samuel Mandell was born on October 26, 1975 in Chicago, Illinois. In May of 1997 he graduated Magna Cum Laude from Illinois College, Jacksonville, Illinois with a B.S. degree in Physics and Mathematics. While at Illinois College, he was awarded the H.L. Caldwell Prize in Physics and the Robert Thrall Mathematics Prize in 1997. He completed his M.S. degree in Physics at Ball State University, Muncie, Indiana in May of 2001. During his time at Ball State University, he was supported by the CERES (Center for Energy Research Education/Service fellowship and was awarded the Cooper Science Physics Award in 2000. In December of 2007, he received his Ph.D. in Physics from the University of Missouri – St. Louis/Rolla. His honors while attending the University of Missouri – St. Louis/Rolla include being awarded the NASA/Missouri Space Grant Consortium research fellowship in multiple semesters from 2005 to 2007.

His accomplishments include publications in journals and conference proceedings in a variety of research areas, including quantum-dot cellular automata, fringe visibility in TEM imaging, and the characterization of presolar materials. He was inducted into the Ball State University chapter of Sigma Pi Sigma (Physics Honor Society) in May of 2000, and has been a member of the American Physical Society since 2000, and the Microscopy Society of America since 2005. He has also been a member of the American Association of Physics Teachers since 2006.